REVERSIBLE ENERGY STORAGE ON A FUEL CELL-SUPERCAPACITOR HYBRID DEVICE

Von der Fakultät Chemie der Universität Stuttgart zur
Erlangung der Würde eines Doktors der Naturwissenschaften
(Dr. rer. nat.) genehmigte Abhandlung

vorgelegt von
Jesus Enrique Zerpa Unda
aus Caracas, Venezuela

Hauptberichter: Prof. Dr. Emil Roduner
Mitberichter: Prof. Dr. Klaus Müller

Tag der mündlichen Prüfung: 18.02.2011

Institut für Physikalische Chemie der Universität Stuttgart
November 2010

Gedruckt mit Unterstützung des Deutschen Akademischen Austauschdienstes

Eidesstattliche Erklärung

Ich versichere, dass ich diese Dissertation selbstständig verfasst und nur die angegebenen Quellen und Hilfsmittel verwendet habe.

Jesus Enrique Zerpa Unda

23.11.2010

Prüfunsvorsitzender: Prof. Dr. Michael R. Buchmeiser
Hauptberichter: Prof. Dr. Emil Roduner
Mitberichter: Prof. Dr. Klaus Müller
Tag der mündlichen Prüfung: 18.02.2011

Contents

1 Introduction

Energy has played a determinant role in the development of the human society by allowing it to adapt and control the environment. In any functional society the managing of energy is essential, for example, in the industrialized world the availability of energy resources is essential as support for critical sectors, such as agriculture, transportation, waste collection, information technology and communication. One of the most important energy resources are the fossil fuels, since they provide more than 80% of the energy consumed in the present time [1]. The increasing use of these types of fuels as energy resource since the Industrial Revolution has been related with serious environmental effects, such as global warming as a consequence of the high amount of green house gas emissions coming form the combustion of such fuels [2]. Specifically in the transportation sector, fossil fuels have been widely utilized as energy carriers resulting in an important global contribution to these green house gas emissions and pollutants.

The use of other energy carriers which produce a lower level of pollutants and such gas emissions is an alternative to lower the environmental effects. Hydrogen, for example, has emerged as one of the most promising candidates for the replacement of the current fossil-fuel-based energy carriers. Low mass density, high abundance, and its environmental friendliness make it an attractive fuel for various applications [3], but an important condition for its wide usage for mobile applications is the development of a safe, cheap and simple storage method. Hydrogen storage has been termed "The Grand Challenge" [4], as the commercially available options, such as storing hydrogen gas in high pressure tanks made of composite materials or steel and storing it as a liquid in cryogenic vessels, either require high pressure or low temperature (or both) for storage, or high temperature for release of H_2, or they require electrical work [5]. These options consume a substantial fraction of the stored energy and may have problems with reversibility [3, 6], for example, the energy necessary for liquefaction of the hydrogen at low temperatures represents almost half of the lower heating value of hydrogen combustion [7]. Therefore, it would be of great advantage to develop a hydrogen storage system that can be reversibly loaded and unloaded near ambient temperature and pressure, perhaps simply by

opening a valve or closing a switch.

Fuel cells are energy converter devices characterized by having a high specific energy and offering an average power output. This feature is very important for the applications when, for example, a vehicle powered by a fuel cell has to maintain a constant velocity or when a computer is running routine process which do not involve a high power demand in a short time. However, instantaneous high power demand cycles, such as driving up-hill or accelerating the vehicle after being stopped at the traffic lights or in a laptop when a CD has to be written or during start-up are common situations in the normal operation of these devices. Therefore, it would be also necessary to consider a system capable of storing energy and of delivering it as a high specific power in a short time, such as a supercapacitor, in order to improve the efficiency of the fuel cell system. Consequently, an energy system which couples the high energy density of fuel cells with the rapid charge/discharge and power capabilities of supercapacitors is desired. Recently, increasing efforts are devoted to the hybridization of fuel cells or batteries with supercapacitors.

In the present work we explore the potential and limitation of a novel concept of energy storage based on hydrogen, the principal advantage of this novel hybrid device is that it works spontaneously (without applying any current or voltage) and reversibly near ambient pressure and temperature. In this concept protons and electrons are firstly electrochemically separated at a fuel cell anode and then stored in the electrical double layer of a supercapacitor. We began by investigating a completely unexplored fuel cell-supercapacitor hybrid configuration based on the combination of a fuel cell-type Faradaic electrode coupled internally with a supercapacitor-type non-Faradaic (also pseudo-Faradaic) electrode in a two-electrode single-cell arrangement. This cell was designed in order to test the basic concept and to study the influence of several variables on its performance, namely the type of the storage material, the response to the pH and concentration of the electrolyte, the influence of the H_2 pressure and the charging and discharging kinetics. An advanced design of this cell involving the combination of a non-Faradaic (also pseudo-Faradaic) supercapacitor-type electrode with two fuel cell-type electrodes in a single cell configuration was tested. The results revealed that the concept is viable, offering a way to store hydrogen (energy) reversibly and at near ambient temperature and pressure and that it is also able to act as a hydrogen buffer in a fuel cell-supercapacitor hybrid configuration.

2 Fundamentals

2.1 Fuel cells

A fuel cell is an electrochemical device which converts directly chemical energy of a fuel into electrical energy in form of DC current. This conversion of energy takes place very simply in comparison with the typical process of electricity generation from fuels, which normally involves several conversion steps with losses of energy present in each step. A fuel cell generates electricity in one single step and without any mechanical losses. Also the efficiency of such a device is remarkably higher than the typical process of electricity generation from fuels, such as the Carnot process. Furthermore, with the use of environmentally friendly generated fuels, this kind of devices could produce near to zero emissions and contaminants. Its simplicity, high efficiency and environmental friendliness are the most attractive features that have made the fuel cell to be considered as one of the candidates for a future environmentally sustainable energy conversion system.

2.1.1 Types of fuel cells

Commonly, fuel cells are grouped by the type of electrolyte they use, namely [8]:

- Alkaline fuel cells use concentrated KOH (50 wt.% -85 wt.%) as electrolyte, and the operation temperature is in the range of 120-250°C. The electrolyte is retained in a matrix, such as asbestos. The electrocatalysts used are Ni, Ag, metal oxides and noble metals.

- Polymer electrolyte membrane fuel cells (PEM fuel cells) use a thin ($\lesssim 50\ \mu$m) proton conductive polymer membrane as electrolyte. The operating temperature is in the range of 60-80°C. The catalyst commonly used is platinum supported on carbon, with loads of about 0.3 mg cm^{-2}.

- Phosphoric acid fuel cells use almost 100% concentrated phosphoric acid as electrolyte. The acid is held in a matrix of SiC and the electrocatalyst used is platinum. The operating temperature range is between 150 and 220°C.

- Molten carbonate fuel cells use a combination of alkali carbonates retained in a ceramic matrix of $LiAlO_2$ as electrolyte. They operate in the range of 600-700°C. At such high temperatures, the use of noble metal catalysts is not necessary.

- Solid oxide fuel cells use a solid, nonporous metal oxide, such as Y_2O_3-stabilized ZrO_2, as electrolyte. The operating temperature is in the range of 800-1000°C where ionic conduction by oxygen ions takes place.

Among all the fuel cell types, the PEM fuel cell has gained increasing importance as energy converter for automotive applications. Also for small-scale distributed stationary power generation and for portable power applications, such as mobile phones and laptops, this technology is a serious option to be considered. PEM fuel cells are briefly described in the following section.

2.1.2 Polymer electrolyte membrane fuel cells

PEM fuel cells are one of the most attractive fuel cell technologies because of their simplicity, viability, quick start-up and many demonstrated applications [8]. As described above, PEM fuel cells use a thin proton conducting polymer membrane as electrolyte which is the most important element of this type of fuel cell. The membrane is impermeable to reactant gases, but it is capable to conduct protons. It is typically made of perfluorocarbon-sulfonic acid ionomer which is essentially a copolymer of tetrafluoroethylene and various perfluorosulfonate monomers. The best-known membrane material is Nafion® made by Dupont. This membrane uses perfluoro-sulfonylfluoride ethyl-propyl-vinyl ether. Figure 2.1 shows the chemical structure of Nafion®. In this structure the SO_3H can be regarded as a dissociated acid, then the end of the side chain is actually an SO_3^- ion with one H^+ ion. Although the Teflon-like backbone is hydrophobic, the sulfonic acid group at the end of the chain is highly hydrophilic. The formation of hydrophilic regions around the clusters of sulfonated side chains facilitate that these kinds of material absorb water in relatively large amounts. Therefore, the proton mobility within well-hydrated regions makes Nafion® a proton conductive material [8]. This means that Nafion® membranes need to be well hydrated in order to conduct protons. The optimal protonic conductivity is in the range of 0.1 S cm^{-1} at room temperature and with a water content of 20-25 water molecules per sulfonate group [9].

Commercially available Nafion® membranes are normally classified by a three digits number. For example, for Nafion® 112, the first two digits refer to the equivalent weight divided by 100 and the last digit refers to the thickness in mil (1 mil = 25 μm)

in the dry state, which means that for Nafion® 112 the equivalent weight is 1100 g Nafion per mol SO_3^- and the thickness is 50 μm. The thickness of the membrane is a very important technical factor. The membrane has to be thin enough in order to minimize the ionic resistance and prevent the drying effect as a consequence of the electroosmotic drag and also thick enough to inhibit the hydrogen crossover permeation.

In a PEM fuel cell, the membrane is placed between two porous, electrically conductive electrodes, which are made of carbon cloth or carbon paper; they are also called the gas diffusion layer (GDL). This layer provides a pathway for reactant gases from the flow field channels to the catalyst layer. The catalyst layer is placed between the gas diffusion layer and the membrane and is made of catalyst particles, typically platinum supported on carbon black.

The combination of the membrane, the GDL, and the catalyst in a PEM fuel cell is called the membrane electrode assembly or MEA. In this configuration the membrane is sandwiched between the two electrodes and GDLs. In the preparation of such MEAs the catalyst layer can be directly formed onto the membrane or onto the GDL. The deposition of the catalyst layer onto the GDL or onto the membrane has been made through several methods, such as spreading, sputtering, spraying, painting, screen printing, electrodeposition and evaporative deposition. One of the most common methods of preparing a MEA is by spray-coating the membrane with a catalyst ink or with a dry powder [8, 10]. In these methods the catalyst ink is sprayed onto the membrane in several layers, until a specific metal loading is achieved.

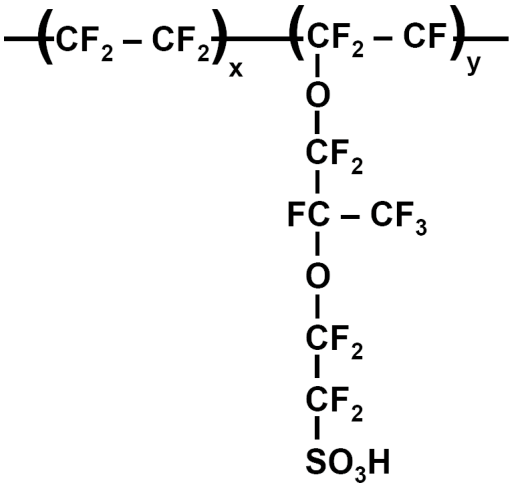

Figure 2.1: Structure of Nafion® perfluorosulfonate polymer. Reproduced from reference [8].

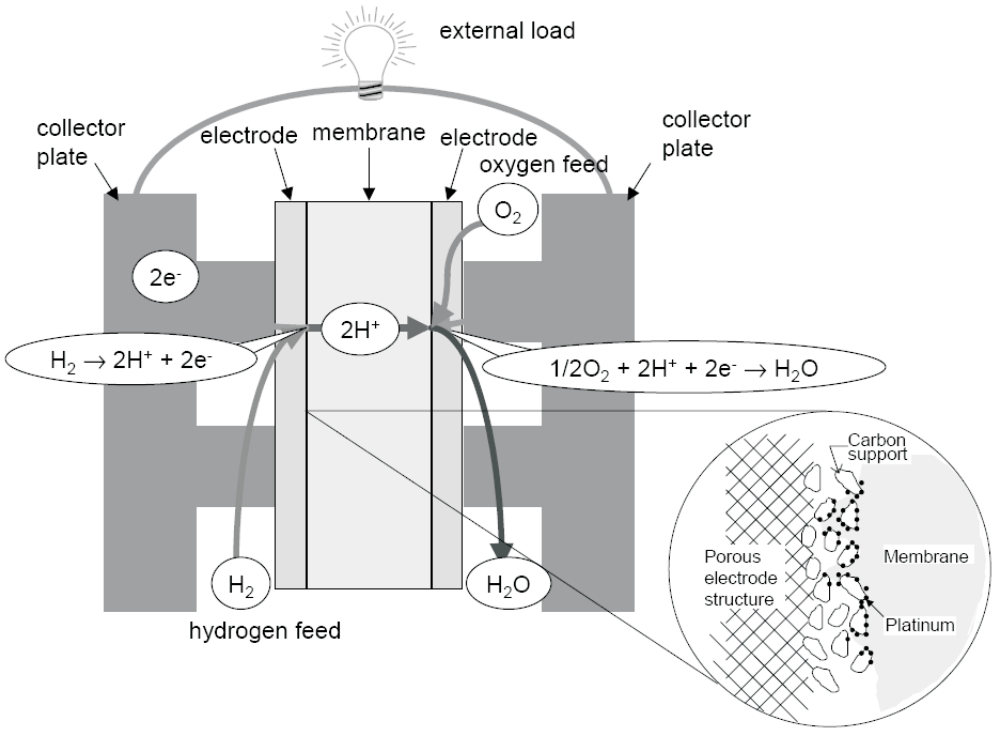

Figure 2.2: Basic principle of operation of a PEM fuel cell. Reproduced from reference [8].

Electrochemical reactions occur at the surface of the catalyst layer, at the interface between the electrolyte and the membrane, specifically where all the three kinds of species that participate on it have access. This is in the so called three-phase boundary. Therefore, the surface area of the catalyst should be maximized by using small platinum particles finely dispersed in the catalyst support. Typical platinum loadings are 0.3-0.4 mg cm^{-2} [8]. Additionally, a higher catalyst active surface area may be obtained by the inclusion of ionomer in the catalyst preparation. It was found that the optimum amount of inomer in the catalyst layer is about 28% by weight [11, 12].

When, for example, hydrogen is fed on one side of the membrane, it is oxidized at the catalyst surface. The oxidation of hydrogen produces protons and electrons. The protons are transported through the polymer membrane, whereas the electrons travel through electrically conductive electrodes, current collectors and through the external circuit generating power and then come back to the other side of the membrane. There they combine with oxygen (which is fed on that side) and the protons that arrived through the membrane to form water, as shown in Figure 2.2. Water is then pushed out of the cell with excess flow of oxygen in order to prevent electrode flooding. The net result of these electrochemical reactions is the flow of electrons

which can perform useful work, i.e. direct electrical current.

The electrochemical reactions in this system occur simultaneously on both sides of the membrane (cathode and anode). Taking into account the basic fuel cell reactions described previously (electrochemical hydrogen oxidation and oxygen reduction) the overall reaction is then described by (2.1).

$$H_2 + \tfrac{1}{2}O_2 \rightleftharpoons H_2O \tag{2.1}$$

This reaction is the same as the hydrogen combustion reaction. However, the combustion is an exothermic process, which means that some amount of energy is released when hydrogen is burned in presence of oxygen. When the product of this reaction is liquid water, then this energy amounts to -286 kJ mol^{-1} (at 25°C and 1 atm), which is known as the hydrogen's higher heating value and is also the reaction enthalpy. There is also a hydrogen's lower heating value, which is obtained when hydrogen is combusted with sufficient excess of oxygen and allowed to cool down to 25°C. Then the products of this reaction will be a mixture of unburned oxygen and water in form of vapor and the heat of reaction amounts to -241 kJ mol^{-1}.

Although no combustion reaction takes place in a fuel cell, the hydrogen's heating value (higher or lower) is used to have an estimation of the energy input into the system. This is the maximum amount of thermal energy that can be extracted from hydrogen. Obviously, not all of this energy input can be transformed into electricity by a fuel cell. The portion of the hydrogen heating value that can be converted into useful work by a fuel cell coincides with the Gibbs free energy, which is determined by equation (2.2).

$$\Delta G = \Delta H - T\Delta S \tag{2.2}$$

The entropy produced in the chemical reaction lowers the amount of energy that can be converted into electricity. It corresponds to irreversible losses in the energy conversion. Therefore, from thermodynamic data it can be calculated that at 25°C and 1 atm, only 237.34 kJ mol^{-1} from 286 kJ mol^{-1} of available energy can be converted into electrical energy, the remaining 48.68 kJ mol^{-1} is then converted into heat. This also represents the theoretical fuel cell efficiency when it is assumed that all the Gibbs free energy can be converted into electrical energy and it amounts to 83%.

The fuel cell efficiency is always proportional to the cell voltage and can be calculated as the ratio of the experimental cell voltage and the voltage corresponding to the hydrogen's heating value (calculated by using equation (2.3)), which is 1.482 V for the higher or 1.254 V for the lower value [8].

$$E = \frac{-\Delta G}{nF} \tag{2.3}$$

2.1.3 Fuel cell polarization curves

The fuel cell performance is commonly characterized by a plot of the cell voltage vs. current density, which is known as a polarization curve. Taking into account the fuel cell electrochemistry it is possible to obtain a mathematical expression which describes the behavior of this curve (2.4).

$$V_{cell} = E_{r,T,P} - \frac{RT}{\alpha F} ln\Big(\frac{i}{i_0}\Big) - \frac{RT}{nF} ln\Big(\frac{i_L}{i_L - i}\Big) - iR_i \tag{2.4}$$

In this equation $E_{r,T,P}$ indicates the equilibrium voltage of the cell at constant pressure and temperature when no net current flows through the electrodes which corresponds to the the open circuit voltage (OCV). α is an experimental parameter called the transfer coefficient and it is equivalent to the symmetry factor β but used to describe a multi step process. i is the current density, i_0 the exchange current density, i_L the limiting current density at which the reactant is consumed faster than it can reach the electrode surface, and R_i is the total cell internal resistance (including the ionic, electronic and contact resistance).

It is important to note that because of the heterogeneous nature of the elements present in the system, such as reactants, products, catalyst and electrolyte, several intermediary sequential and parallel steps are involved in the overall reaction. Figure 2.3 shows a typical fuel cell polarization curve in which three different regions can be noted [8].

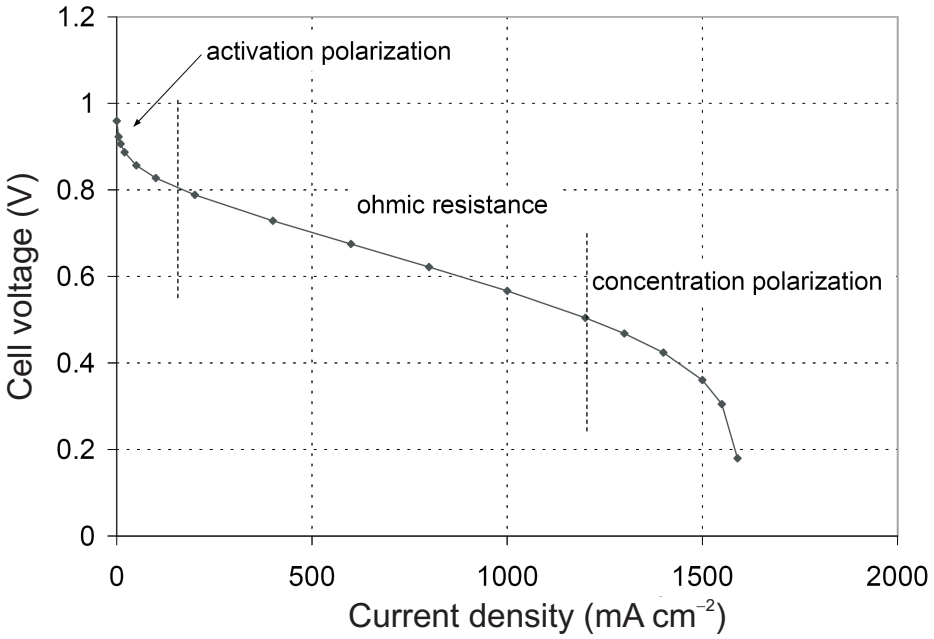

Figure 2.3: Typical fuel cell polarization curve. Reproduced from reference [8].

- At low current densities: The cell voltage falls sharply as a consequence of the so-called activation polarization. It is associated with sluggish electrode kinetics and it occurs because some voltage difference is needed (overpotential) in order to keep the electrochemical reaction going. The rate of the electrochemical reactions is determined by an energy barrier that the charge must overcome in being transfered from electrolyte to a solid electrode or vice versa. The losses are also related to the value of the exchange current of the electrochemical reaction, the higher the exchange current density the lower the activation polarization losses. This polarization loss can be present at both, anode and cathode. However, oxygen reduction requires much higher overpotentials than hydrogen oxidation. In fact, the exchange current of the electrochemical hydrogen oxidation is about 10^{-4} vs. 10^{-9} A cm^{-2} for the oxygen reduction on Pt at 25°C and 1 atm. The second term on the right hand side of equation (2.4) corresponds to this type of losses.

- At intermediate current densities: The cell potential decreases linearly with the current density. This effect is caused by ohmic losses and is associated with the resistance to the flow of electrons through the electrically conductive fuel cell components and to the flow of ions in the electrolyte. Typically the ionic and contact resistances are the most relevant and the electronic resistance can be neglected. In the fourth term on the right side of equation (2.4) these losses are represented following Ohm's law. The effect of this polarization loss in the polarization curves is characterized by the increase in the absolute value of the slope with increasing the internal resistance.

- At high current densities: The cell potential exhibits a pronounced non-linear drop with the current density. This polarization loss is called concentration polarization and occurs when a reactant is rapidly consumed at the electrode surface in a way that concentration gradients are established. The surface concentration reaches zero when the rate of reactant consumption exceeds its diffusion rate. The current density at which this phenomenon occurs is called the limiting current density. This is the maximal current density that the fuel cell can produce at a given condition and depends on how fast the reactants can reach the electrode surface. The third term on the right side of equation (2.4) is related to this type of losses.

There are other curves deriving from the polarization curves, for example, the power density vs. current density curves. The power density (in mW cm^{-2}) is the product of the voltage and current density. This curve may be plotted together with

the polarization curve and it shows that there is a maximum of power density a fuel cell may reach. This is a very useful information because it does not make any sense to operate a fuel cell at a voltage beyond its maximum of power. The same power output may be obtained at a lower current and higher voltages. The polarization curves can be also used for fuel cell sizing purposes. Usually, a fuel cell is rarely sized anywhere close to the maximum power density and its operating point is selected at cell potentials around 0.7 V.

2.2 Electrochemical supercapacitors

2.2.1 Introduction

The principle that charge can be stored on a charged capacitor has been known since 1745. The energy stored between two parallel plates at a given voltage (V), where the charges $+q$ and $-q$ in the plates are separated by an insulator material increases with V^2(Gibbs free energy) and is given by (2.5). In this equation C is called the capacitance and is given in units of farad which is 1 coulomb per volt [13].

$$E = \frac{1}{2}CV^2 = \frac{1}{2}qV \tag{2.5}$$

The application of this principle for practical purposes in storing electrical charge in a cell or battery of cells was proposed for the first time by Becker in 1957. This idea involved the use of a porous carbon material perfused with an aqueous electrolyte. A charge was then held in its interfacial double layer storing electrical energy [13]. This principle involved the charge of the electrochemical double layer capacitance (C_{dl}) which arises at all solid/electrolyte interfaces, such as metal, semiconductor and colloid interfaces. The first electrochemical capacitor was then created.

A different principle, developed in 1975 by Conway [13], which involves the type of capacitance denoted as "pseudocapacitance" was also used as a basis for energy storing on a capacitor. This is associated with the potential dependence of electrochemical adsorption of H or electrodeposition in monolayers of some metals (Pb, Bi, cu) at Pt or Au. Also the pseudocapacitance related with solid oxide redox systems of, for example, RuO_2 has been studied [13].

Carbon materials, such as graphite, glassy carbon, amorphous carbons and carbon blacks, are widely used in the fabrication of electrochemical capacitors. These materials are convenient for forming high-area electrode structures, normally on a support matrix. In electrochemistry, carbon is considered as a relatively unreactive material, having a potential voltage range of almost ideal polarizability, which approaches 1.0 V in aqueous solution and up to 3.5 V in nonaqueous media [13].

Not only the electrode material determines in the performance of an electrochemical capacitor. The dielectric material of such devices also plays a very important role since it is the solvent of the electrolyte solution. It forms locally the dielectric of the double layer and provides the solvation shells of the ions present in this medium. The double layer at the electrode/solution interface consists of two layers: The first layer can be represented as a real electronically conducting plate, such as a metal, semiconductor, oxide or carbon surface, and the second as a virtual plate that is in the inner interfacial limit of an ion conducting electrolyte solution [13]. The charges are then distributed in a double layer configuration formed across this interphasial region. The term interphasial region is chosen over the word "interfacial" since the boundary region is really 3-dimensional rather than 2-dimensional [13]. The double layer is composed of a compact layer of 0.5 to 0.6 nm thickness (corresponding to the diameters of the ions and solvent molecules present) and a wider region of 1 to 100 nm thickness, depending of ion concentration, where the ions are thermally distributed. As a consequence of the very small thickness of the compact interphasial layer, specific capacitances on the order of 20 to 50 μF cm^{-2} can be achieved. Typical distances in dielectric capacitors are in the range of 10 to 100 nm with oxide-film dielectrics (electrolytic capacitors) or 1000 nm with very thin mica or polystyrene dielectric-film hardware capacitors. Therefore, the capacitances per cm^2 area achievable by double layer capacitors are 10^4 times those of ordinary dielectric capacitors (see equation (2.7)). A more detailed description of the double layer in such systems is given in the following section.

A practical supercapacitor of the double-layer type consists of two electrodes immersed in an electrolyte where each electrode has its own interphasial double layers and exhibit its own capacitance so that the complete cell can be considered as two capacitors in series. The dielectric (electrolyte solution) and the ion permeable separator are found between these two interphasial regions, as illustrated in Figure 2.4. The cell capacitance (C_{cell}) of a symmetrical capacitor with similar electrodes is expressed by equation (2.6) where C_1 and C_2 are the capacitance of the first and second electrodes.

$$\frac{1}{C_{cell}} = \frac{1}{C_1} + \frac{1}{C_2} \tag{2.6}$$

The double layer capacitance (C_{dl}) at each electrode interface is given by equation (2.7) where A is the surface area of the electrode, ε is the dielectric constant of the electrical double-layer region and d is the thickness of the electrical double layer.

$$C_{dl} = \frac{\varepsilon A}{4\pi d} \tag{2.7}$$

In regular dielectric capacitors the geometrical factors and the bulk properties of

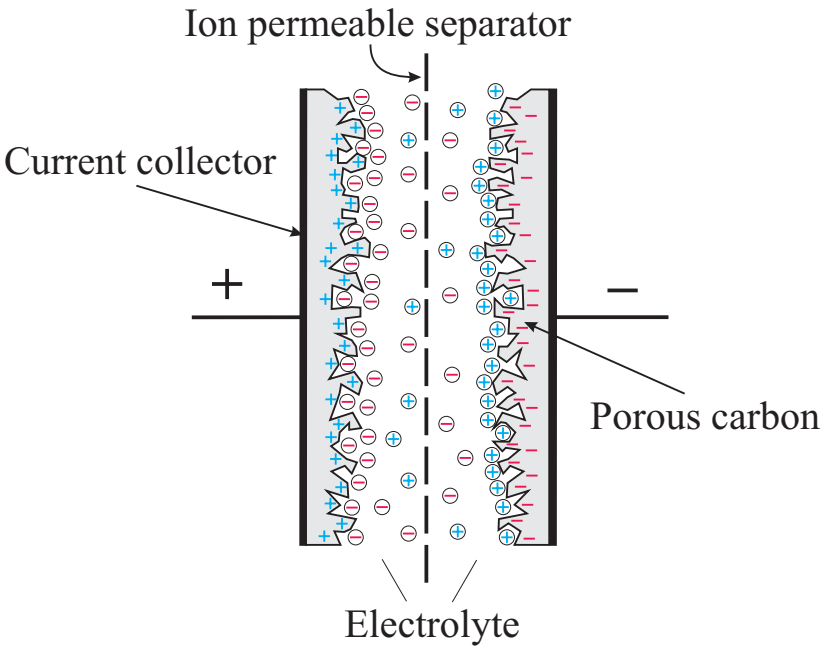

Figure 2.4: Electrochemical double layer capacitor in the charged state.

the dielectric medium determine the capacitance of the device. In contrast, in electrochemical capacitors it is the microscopic properties at the molecular level of the dielectric (electrolyte solution) that determine the specific double-layer capacitance.

The terms "supercapacitor" or"ultracapacitors" are derived from the large capacitances that can be developed with such devices. With an electrochemical capacitor made of high specific area porous carbon electrodes of about 1000 $m^2\ g^{-1}$ and having a nominal specific capacitance of ca. 25 $\mu F\ cm^{-2}$, an overall capacitance of 250 $F\ g^{-1}$ is theoretically realizable. Furthermore, at 1 V operating potential this capacitance can theoretically store a specific energy of about 250 $J\ g^{-1}$ [13].

Such devices are characterized by a high degree of reversibility of charge acceptance and delivery and also a capability of excellent operating power levels compared with batteries of a similar size. Battery-type charge/discharge processes are based on Faradaic processes which lead to major chemical and structural changes of the electrochemically reactive materials. For example, the conversion of lead dioxide to lead sulfate and lead metal to lead sulfate during discharging of the lead-acid battery limits its cycle life to 1000-3000 cycles, depending on rates of charge and discharge and temperature. In contrast, electrochemical double-layer capacitors can exhibit cycle lives up to one million under suitable conditions. This is because, ideally at least, only storage and delivery of electrostatic charge takes place at the extended two-dimensional interface of high-surface-area materials and no irreversible or slow

chemical phase changes take place as they do between 3-dimensional chemical materials in rechargeable batteries. This is a fundamental difference between the electrochemical behavior and properties of electrochemical capacitors in comparison with batteries.

2.2.2 The electrochemical double layer

A detailed description of the properties and structures of the double layers is essential for a full understanding of the operation of a double-layer capacitor and the specific capacitances that are achievable by these devices using active porous materials in various systems. In the study of the behavior and structures of electrified interfaces it is important to have an estimation of the double-layer capacitance and its dependence on the electrode potential. The relation between the charge q accumulated at each side of the electrode interfaces, such as electron density on the metal and ion density on the solution side and the measured electrode potential (E), can be described as a differential quantity (capacitance) following equation (2.8). It is assumed that these types of values give more resolved information than the corresponding integral relation, in this case the total charge plotted vs. the electrode potential E at which this charge has been accumulated. This is the reason for the wide use of cyclic voltammetry and ac impedance techniques in evaluating the double layer and the resulting electrochemical capacitor devices [13].

$$C_{dl} = \frac{dq}{dE} \tag{2.8}$$

The following section is dedicated to the description of the double layer structure which is the 3-dimensional interphasial region (of 0.3 to 0.5 nm thickness) of the metal/electrolyte boundary. The concepts of surface concentration or surface excess of ions of the electrolyte and solvent molecules are then used to describe this region [13].

Models and structures of the double layer

It is useful to describe the models of the double layer in the historical order with which they were presented in the literature. Following the progress towards a correct description of the structure of the interphase at electrode surfaces, a better understanding of the underlying situation is gained.

The concept and model of the double layer consisting of two array layers of opposite charge facing each other as on the plates of a two-parallel-plate dielectric capacitor and separated by a small distance (atomic dimensions) arose in the work

of von Helmholtz (1853) on the interfaces of colloidal suspensions. This model is illustrated in Figure 2.5 (a). Note the compact structure of the double layer used in this model. In the original model for colloid interfaces, the charges generated by acid-base ionization at the colloid phase where counterbalanced by counterions of opposite sign of charge on the solution side forming a double-layer array of positive and negative charges. This model was later adapted to the case of metal/electrolyte interfaces where a controllable surface density of excess of negative or positive charge can appear, corresponding with the excess or deficiency of electron charge of the delocalized electron plasma of the metal.

The assumption that the ions in the solution side of the double layer remain static in such a compact array neglected the thermal fluctuation effects which affect the ion distribution in the solution according to the Boltzmann principle. In a modified representation of the double layer, developed by Gouy in 1910, a thermal fluctuation factor was included and the counterions were represented as a 3-dimensional diffusely distributed population of cations and anions in the solution with a net charge density equal and opposite to the virtually 2-dimensional electron excess or deficit charge on the metal surface. This model is known as the Gouy model and is shown in Figure 2.5 (b). In this model, the ions were considered as a point charges. This led to the failure of the model in the estimation of the potential profile and local field near the electrode surface and therefore to prediction of too-large capacitance values. The interphasial capacitance related with this model is commonly referred to as the "diffuse" double-layer capacitance [13] and was fully mathematically treated by Chapman in 1913.

In 1924 the problem with the overestimation of the double-layer capacitance present in the Gouy-Chapman treatment was resolved by Stern in his contribution to the theory of double layers. The calculations made in this model assumed that first, the inner region of the ion distribution could be treated in terms of an adsorption process according to Langmuir's adsorption isotherm, and second that the region beyond this inner layer into the solution could be effectively treated in terms of a diffuse region of distributed ionic charge as treated by Gouy and by Chapman. The ions, in this case, were considered as having a finite size taking also into account the annular thickness of their hydration shells. Following this assumption Stern, could define a geometrical limit to the compact region of adsorption of ions at the electrode surface (see Figure 2.5 (c)). This region corresponds to a Helmholtz-type of compact double layer which has a capacitance C_H. The remaining ionic charge density beyond this compact array of ions is then referred to as the "diffuse" region of the double layer with a capacitance C_{df}. The overall double-layer capacitance (C_{dl})

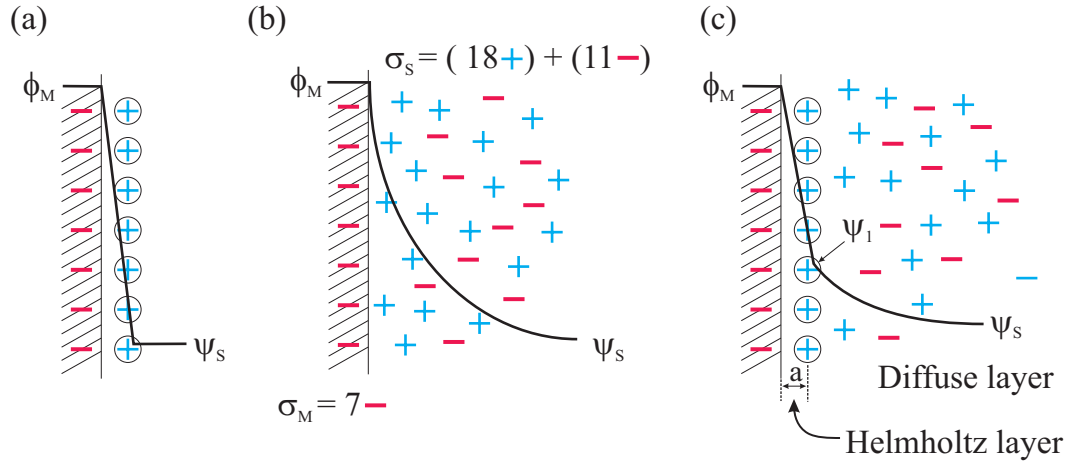

Figure 2.5: Models of the electrochemical double layer: (a) Helmholtz model, (b) Gouy point-charge model (σ is specific charge per unit area), (c) Stern model [13].

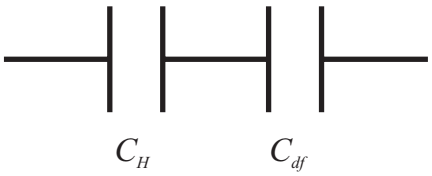

Figure 2.6: Series combination of the Helmholtz layer (C_H) and diffuse layer (C_{df}) capacitances.

is related to these capacitances following equation (2.9) and its value is determined by the smaller of these two components. This corresponds to a series combination of both capacitances as in the equivalent circuit shown in Figure 2.6.

$$\frac{1}{C_{dl}} = \frac{1}{C_H} + \frac{1}{C_{df}} \tag{2.9}$$

Although the Stern theory of the double layer was a good basis for interpretations of electrode interface phenomena, the work of Grahame [14] in 1947 on the double layer capacitance at the mercury electrode in aqueous solutions led to a further advance in this field. The Grahame model of the double layer (Figure 2.7) makes an important distinction between the distances of closest approach of the anions and cations at the electrode surface, originated by the fact that most common cations are smaller than common anions and can retain their solvation shells. This corresponds to the formation of an inner and outer Helmholtz layer in the interphase electrode/electrolyte which also means that in this model three different layers are

considered: the inner and the outer Helmholtz layer and a diffuse ion distribution region.

The ideally polarizable electrode

In order to understand the meaning of the double-layer capacitance at electrode interfaces, it is necessary to describe the conditions under which charge separation takes place between the electrode surface and the solvated ions in the solution in the interphasial region. Specifically, the concept of an ideally polarizable electrode is key in this interpretation.

In an ideally polarizable electrode the changes in potential caused by the flow of charge from or to the electrode only produce changes in the charge density on the metal. Consequently, the ion density in the solution side of the electrode/electrolyte interface also changes, leading to the charge of the double layer. No Faradaic electrode reactions occur within a relatively wide electrode potential range. This concept was described by Grahame in 1947 [14].

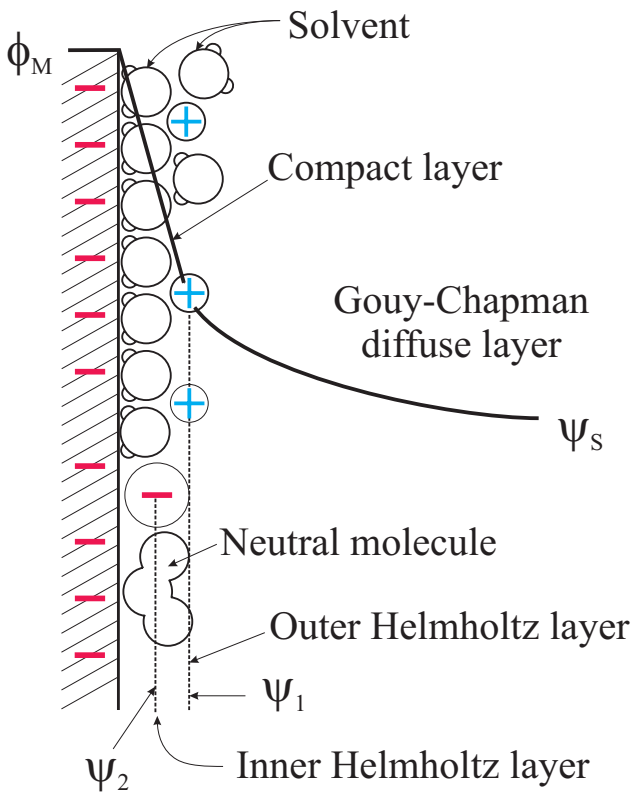

Figure 2.7: Double layer structure with different regions of adsorption of hydrated cations, less hydrated anions, solvent molecules and an adsorbed neutral molecule corresponding to the Grahame model [13].

The Hg electrode in aqueous electrolyte solutions behaves almost as an ideally polarizable electrode over the potential range of +0.23 V to −0.9 V vs. the normal hydrogen electrode (NHE). With the flow of charge from an external circuit to the Hg electrode in this potential range, only the double layer is charged with zero Faradaic current passing through the interface. At potentials more negative than −0.9 V, H_2 is produced as a consequence of the solvent water decomposition through the Faradaic charge transfer following (2.10).

$$2\,H_2O + 2\,e \rightarrow H_2 + 2\,OH^- \tag{2.10}$$

At potentials near to 0.23 V or higher the Hg electrode in, for example, KCl solution becomes electrochemically oxidized according with

$$2\,Hg + 2\,Cl^- \rightarrow Hg_2Cl_2 + 2\,e \tag{2.11}$$

or in basic medium at a different potential (+0,0977 V)

$$Hg + 2\,OH^- \rightarrow HgO + H_2O + 2\,e \tag{2.12}$$

Between this potential range the electrode interphase approaches ideal polarizability with the charge of an almost nonleaky double-layer capacitance. Therefore, this interphase is capacitorlike in its electrical response, with the storing of charge in the double layer [13].

Equivalent circuit representation of double-layer electrical behavior

The electrode interphases described here can be represented by a combination of electrical elements in an equivalent circuit. An ideally polarizable electrode is described, for example, as a simple capacitance (see Figure 2.8 (a)) which may also have a potential dependent value. When a Faradaic process is present and a current parallel to the double-layer charging current passes, then a modified equivalent circuit applies where the equivalent Faradaic leakage resistance (R_F) and electrolyte resistance (R_S) are noted (see Figure 2.8 (b)). The R_F is very important in electrochemical capacitors and batteries because it is the basis of the self-discharging.

The behavior of the equivalent circuits in Figure 2.8 (a) and (b) is easily distinguished by comparing their impedance spectra with variations of frequency. The circuit (a) exhibits a pure capacitive response while (b) has a maximum capacitive impedance for a given value of C_{dl} and R_F at a certain frequency and a particular potential [13].

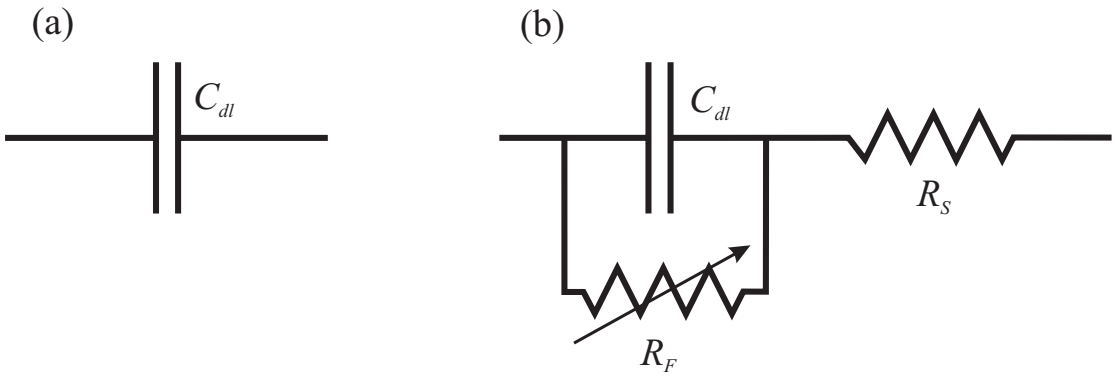

Figure 2.8: Equivalent circuits representing the pure double-layer capacitance (a) of an electrode interphase and the situation when a Faradaic process is also present (b). The R_S represents the electrolyte resistance.

2.2.3 Carbon materials for electrochemical capacitors

Carbon has been extensively used in a variety of electrochemical systems. The different forms in which it is available makes the selection of the appropriate carbon for a specific electrochemical system and the prediction of its electrochemical behavior particularly difficult.

In the industry the major application for carbons is in the fabrication of electrodes for steel arc furnaces and brushes for electric motors [15]. The raw material used in the production of carbon and graphites is derived from other industries as by-products, for example, petroleum coke and coal-tar pitch are residues from the petroleum refining and the steel industry.

Carbon represents an interesting alternative for electrochemical applications because of its good electrical and thermal conductivities, low density, adequate corrosion resistance, low thermal expansion, low elasticity, and high purity. Furthermore, carbon materials can be produced in a variety of structures, such as fibers, powders, large blocks and thin solid and porous sheets being easily available and generally low-cost [15].

In the specific field of electrochemical capacitors, the carbon materials used are far from being electrochemically inert. Oxidation or reduction of the redox electrochemical functionalities that are initially present in various carbon materials can occur during polarization generating a kind of electrochemical reactivity and the so-called pseudocapacitance as well as the double layer capacitance. The carbon materials usually selected for the use as electrodes in electrochemical capacitors possess a unique combination of chemical and physical properties, namely [13, 16]:

- High surface-area range on the order of 1000 m^2 g^{-1}.

- High intra- and and interparticle conductivity in porous matrices.

- Good corrosion resistance.

- Good electrolyte accessibility to the intrapore surface area.

- Controlled pore structure.

- Relatively low cost.

Carbon surface functionalities

Most carbons exhibit a certain concentration of surface functionalities, for example, the oxygen-based type (see Figure 2.9), which are formed as a consequence of the chemisorption of oxygen at prolonged exposure to air. These surface functionalities are very important because of their influence on the physicochemical properties (i.e. wettability, catalysis, electrical and chemical reactivity) of carbonaceous materials. The formation of these functionalities in the carbon, specifically at the edges of the basal planes, is related with the presence of some residual surface bonds which can give rise to a high reactive surface free radical character and the subsequent formation of oxygen-based species [15].

The surface properties and conditions of carbon particles depend to a great extent on the preparation and conditioning procedures which also include the type of initial

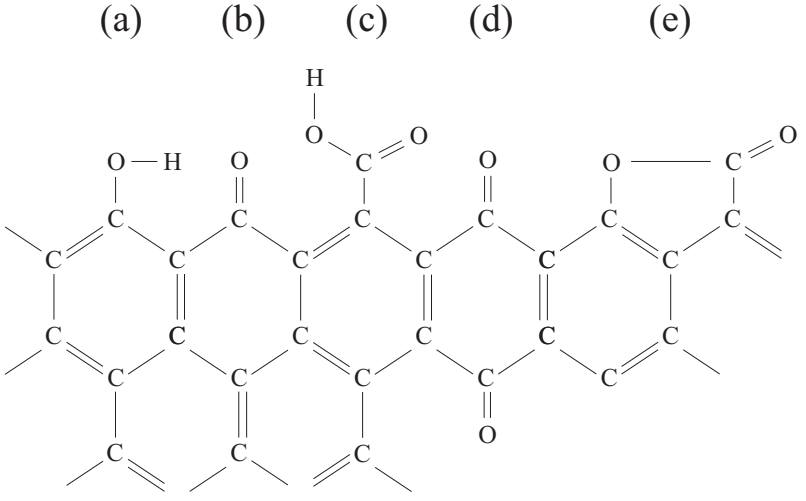

Figure 2.9: Schematic diagram representing the oxygen-based surface functional groups on carbon: (a) phenol, (b) carbonyl, (c) carboxyl, (d) quinone and (e) lactone [15].

organic compound from which the carbon was formed and the thermal treatment applied. The redox couple quinone/hydroquinone in aqueous solution of H_2SO_4 is one of the electrochemically active species most commonly found in various carbon types, such as carbon blacks and graphites, having a redox potential of about +0.65 V vs. NHE [15]. The relative proportion of these functionalities in the carbon normally tends to scale with the specific surface area of the material. They are also responsible for the significant redox pseudocapacitance (C_Φ) exhibited by such materials when also the predominant double layer capacity is present (C_{dl}). It is reported that in some carbon materials the contribution of the pseudocapacitance can amount up to 5-10% of the total realizable capacitance [13]. The distinction between these two types of capacitances is in principle possible using impedance analysis, however, it becomes a difficult task when porous carbon materials are involved.

The pseudocapacitance is defined as a kind of capacitance originated by Faradaic redox reactions and electrosorption processes at the electrode surface. It arises where fast, potential-dependent redox reactions result in charge transfer across the double layer as in battery charging or discharging. Such reactions become thermodynamically favorable at certain potential ranges producing charge/discharge capacitive behavior. This is generated by the appearance of a derivative ($\mathrm{d}q/\mathrm{d}V$), which is equivalent to a capacitance, as a consequence of a change in the rate of charge acceptance with changes in potential.

In addition to the electroactive redox species, other surface acidic or basic titrable functionalities related to some surface structures, such as α-diketone, ketone, phenolic, carboxylic, carbinol, *o*-hydroquinoid and lactone [13] are found in various carbon materials. As mentioned before, they influence the wettability of carbon materials which is a very important factor in maximizing the access of electrolyte to the carbon surface. It is reported that the electrochemical oxidation of carbon increases its wettability as a consequence of an increase in the hydrophilic oxygen-based surface groups. The electrochemical reduction has then an opposite effect [17, 18].

It is also believed that the amount of oxygen present in the carbon as physically adsorbed oxygen or as surface complexes influences the rate and the mechanism of capacitor self-discharge or leakage [13]. Specifically, carbons with a high concentration of acidic surface species exhibit high rates of self-discharge. For example, an increasing leakage current was observed by Pandolfo et al. [16] with increasing concentration of acidic surface functional groups, suggesting that they may serve as active sites which catalyze the electrochemical oxidation or reduction of carbons or the decomposition of the electrolyte components.

Double layer capacitance of carbon materials

Generally, it is assumed that the mass specific capacitance of a porous carbon is proportional to its available surface area (in m^2 g^{-1}). Although this tendency is sometimes observed, in practice it represents an oversimplification [19, 20]. Some factors have to be taken into account in order to describe this complex (non-linear) relationship [16]:

- The method used in the measurement of the electrode surface-area.
- Variations in the specific capacitance of carbon electrodes with differing morphology.
- Variations in the surface chemistry, i.e. wettability and pseudocapacitive behavior.
- Variation in the conditions at which carbon capacitance is estimated.

The most widely used method to measure the surface areas of porous materials is the gas adsorption, usually nitrogen at 77 K. This adsorption data is typically analyzed by means of the Brunauer-Emmett-Teller (BET) theory in order to have an estimation of the apparent surface area. It is reported in the literature that this method has some limitations when it is applied to calculate the surface area of highly porous and heterogeneous materials and, therefore, should be used as a semi-quantitative tool [16]. The major limitation in correlating the capacitance with the BET surface-area arises when the assumption that the surface-area accessed by nitrogen gas is similar to that accessed by the molecules of the electrolyte during the capacitance measurements. It is expected that during the absorption the gas molecules penetrate almost all the open pores with a molecular size higher than that of the adsorbate, in contrast the electrolyte accessibility will be more sensitive to changes in the carbon structures and surface properties.

The specific double layer capacitance of various materials in different electrolytes is listed in Table 2.1; it seems to depend on the pretreatment history and overall morphological characteristics. As mentioned before, the measurements of carbon capacitance is very dependable on the experimental conditions employed. For example, the capacitance of microporous carbons is affected by variations in the discharging current used in the experiments due to the effect of limited electrolyte diffusion in narrower pores. Therefore, capacitances have to be measured at fixed current density, if the data will be used for comparative purposes.

Table 2.1: Electrochemical double-layer capacitance (C_{dl}) of carbonaceous materials, reproduced from reference [13].

Carbonaceous material	Electrolyte	C_{dl} (μF cm^{-2})[a]	Remarks
Activated carbon	10% NaCl	19	Surface area 1200 m^2 g^{-1}
Carbon black	1 M H_2SO_4	8	Surface area 80-230 m^2 g^{-1}
	31 wt.% KOH	10	
Graphite powder	10% NaCl	35	Surface area 4 m^2 g^{-1}
Graphite cloth	0.168 N NaCl	10.7	Surface area 630 m^2 g^{-1}
Glassy carbon	0.9 N NaF	13	Solid
Carbon aerogel	4 M KOH	23	Surface area 650 m^2 g^{-1}

[a] Values based on estimates. For a comprehensive discussion see reference [13].

Carbon surface-area and porosity

Porous carbon, especially in the activated form, are normally characterized by large values of BET surface areas which are in the range of 500 to approximately 3000 m^2 g^{-1}. The IUPAC classifies the different pore sizes in three categories as follows: micropores (diameters < 2 nm), mesopores (diameters between 2 and 50 nm) and macropores (diameters > 50 nm) [21]. These values can be compared with the diameter of a hydrated sodium ion (ca. 0.65 nm) or a water molecule (0.286 nm).

Micropores, present in significant proportions in high surface-area activated carbons, are a major contributor to the measured area due to its high surface-area to volume ratio. They play an important role in the selectivity of adsorption-based processes through a restricted diffusion and molecular sieve effect. Mesopores also contribute to the surface area and enhance the adsorbate accessibility due to their relatively larger size. Macropores generally make a negligible contribution to the surface area of porous carbons and their major function to provide transport avenues into the interior of the carbon particles.

Some studies on micropore accessibility in aqueous solvents have shown that pores with a diameter greater than 0.5 nm are available for the electro-adsorption of sim-

ple hydrated ions [22, 23]. Specifically, a study performed with carbon xerogel using aqueous H_2SO_4 as electrolyte concluded that the optimal pore size range for double-layer capacitance is between 0.8 and 2.0 nm [24]. The electrolyte will only access the narrow porosity through an appreciable cumulative solution resistance as a consequence of the restricted diffusion within these narrow pores. This contributes to high time constants and low rate capabilities due to the retardation in the ion movement in the pores during charging and discharging of the electrochemical double-layer capacitor. Consequently, these types of porosity will only contribute to a small degree to charge storage capacity under high rate or short duration power-pulse discharge or recharge [13].

In electrochemical capacitors based on porous electrodes a distributed electrolyte resistance which extends into the the pores is present. This resistance, which can be represented with resistor elements (R) in equivalent circuits, is coupled with distributed interfacial capacitance elements (C) and leads to an electrode with a non-uniform distribution of effective resistance and capacitance. This electrode is then represented as a complex network of RC circuits (each a series of RC combinations) which leads to different RC time constants and charging and discharging relaxation times. This is normally referred to as the transmission line model [25] and it is illustrated in Figure 2.10.

At low charge rates, or frequencies, the ions of the electrolyte have time to penetrate into the pores and additional surface area is accessed. When the charge rates or frequencies increases, the electrolyte penetration becomes poorer and less surface area is accessed. It is suggested that large pores lead to a lower distributed electrolyte resistance and a greater electrolyte penetration which permits the use of the

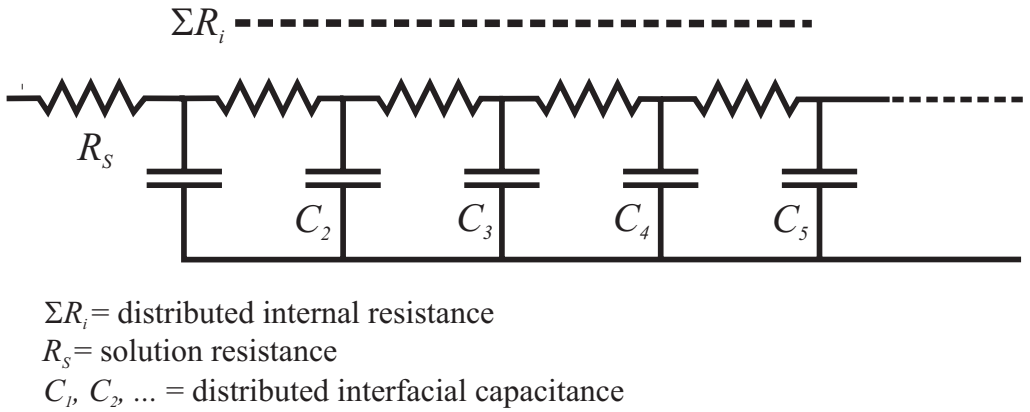

Figure 2.10: Equivalent circuit of a porous system surrounded by an electrolyte having an distributed RC network (transmission-line model).

majority of the surface area and therefore the capacitance of the electrode. Clearly, the pore size distribution of porous carbons plays a very important role in determining the fundamental performance criteria of carbon-based supercapacitors as, for example, the relationship between power and energy density and the dependence of performance on frequency [16].

Significance of *RC* constants

Considering the charging behavior of a simple model series RC circuit where the charge flow into the capacitance C (double-layer capacitance) is obstructed by a resistance R (electrolyte resistance) when a potential difference ΔV is applied, the current response can be described by equation (2.13). It means that the charging current through R into C reaches a maximum at $t = 0$ and declines exponentially with time. When $t \to \infty$ the current trends to zero. This behavior is characterized by a reduced time t/RC where RC is the time constant of this series RC combination which determines the rate at which the electrical response of the system can take place. This constant is a very important factor in evaluating the power capabilities on discharging or recharging and therefore the opportunities for practical operations of electrochemical capacitors.

$$I(t) = I_0 \; e^{\,(-t/RC)} \tag{2.13}$$

A situation with similar behavior but in reverse is observed when a charged capacitor is allowed to discharge into an ohmic load resistance (R_L) in a parallel RC circuit as shown in Figure 2.11. In this case, the discharging current from C is equal to the current through R_L. After some algebraic operations equation (2.14) is obtained which is analogous to the behavior of the series RC circuit. V_i is the potential at $t = 0$ across C and again when $t \to \infty$ the $I(t) \to 0$ as the discharge of C is completed.

$$I(t) = \frac{V(t)}{R} = \left(\frac{V_i}{R}\right) \; e^{\,(-t/RC)} \tag{2.14}$$

With this elementary example the situation having more complex equivalent circuits (e.g. the transmission line model) can be illustrated. In such complex cases parallel RC combinations and inductive elements L may be also involved, complicating the analysis of their electrical response.

Carbon black materials

Carbon blacks are characterized by having near spherical carbon particles of colloidal size, which are formed by thermal decomposition or partial oxidation of hydrocar-

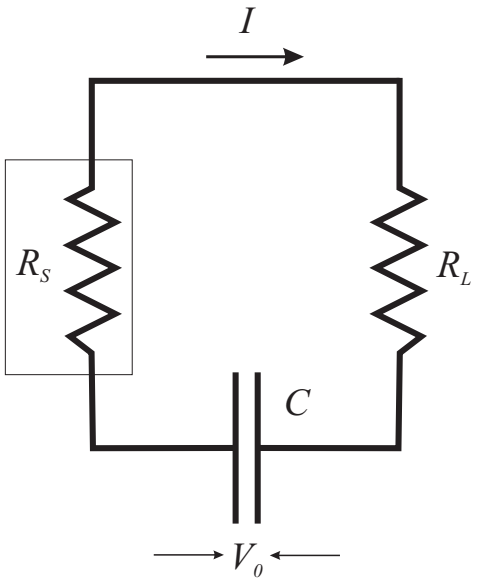

Figure 2.11: Equivalent circuit of a capacitor in parallel with a ohmic load resistance R_L. The electrolyte resistance R_S is also shown.

bons in the gas phase. The formation of polyaromatic macromolecules in the vapor phase is followed by nucleation of these macromolecules into droplets, which are then transformed into carbon-black particles. The properties of these materials depend on the feedstock used and manufacture procedures. Commercial carbon blacks are typically classified according to their method of preparation or intended application [15].

Highly conductive carbon blacks exhibit a high structure (i.e. aggregates with a highly branched, open structure), high porosity, small particle size and a chemically clean surface (free from oxygen). The typical conductivity of the carbon blacks is in the range of 10^{-1} to 10^{2} $(\Omega\,\mathrm{cm})^{-1}$ and is achieved through electron tunneling between close aggregates and through graphitic conduction between touching aggregates [16].

The surface area of these materials may vary from < 10 to greater than 1500 $\mathrm{m}^2\,\mathrm{g}^{-1}$ corresponding to particle sizes of > 80 to < 10 nm in diameter. The surface area of carbon blacks is considered to be one of the most accessible among other forms of high surface area carbons [26]. It is reported that specific capacitances of up to 250 F g^{-1}, corresponding to double-layer capacitances in the range of 10-16 μF g^{-1}, have been achieved by supercapacitors with high surface-area carbon black electrodes mixed with a binder substance [26, 27]. On the other hand, the use of high levels of binder required to prepare mechanically stable electrodes, as a consequence of the low compacted density of high surface-area carbon blacks, leads to lower electrical conductivities and volumetric capacitances.

2.2.4 Experimental evaluation of electrochemical capacitors

A quantitative evaluation of the capacitance (C) and its dependence on various experimental variables is necessary in order to test the behavior of electrochemical capacitors. This also provides important information needed to understand the phenomenon involved and to improve the performance of the system. It is always desirable to obtain this information by direct instrumental measurements.

Several simple, elementary and widely used criteria for evaluating the electrical response of an electroactive material which behaves capacitively are the following [13]:

- Galvanostatic charge: In an interfacial charging process performed at constant current density (i) in a two electrode configuration, the potential difference (ΔV), developed across the capacitor electrodes, changes linearly with time as the charge provided by i builds up across the interface over some time interval (Δt). Combining equation (2.8) and (2.15) an expression for C (equation (2.16)) is found [13].

$$\Delta q = \int i \; dt \tag{2.15}$$

$$C = \frac{\int i \; dt}{\Delta V} = i \; \frac{\Delta t}{\Delta V} \tag{2.16}$$

  Equation (2.16) is valid when the capacitance is constant with the potential. However, experimentally it is commonly found that ΔV deviates from a linear dependence on time at constant current. In this case, C is calculated as the reciprocal of the slope of the V vs. t curve (see Figure 2.12) or differentially at some point of this curve as $(\mathrm{d}\Delta V/\mathrm{d}t)^{-1}$ when C is not constant with ΔV. The V vs. t curve at constant current is typically referred to as the "charging curve" [13].

  The region a-b in Figure 2.12 corresponds to pure non-Faradaic double-layer charging. Here the electrode behaves as an ideally polarizable electrode and no Faradaic process takes place. Region b-c includes an increasing component of the passage of charge involving a parallel Faradaic reaction (Faradaic current i_F), the electrode behaves as non-polarizable and decomposition of the solution may take place [13].

- Potential step sequence: When a potential step δV is applied to the electrode, the charge δq which flows into the interface is determined by $C\delta V$ where C is the capacitance over the potential range δV. In such an experiment, a current transient (i_t) is created (see Figure 2.13) by the potential pulse δV over a small

but finite response time and δq is the integral of i_t over that time interval. The capacitance is then calculated either from the δq response for the pulse of potential or from the sum of δqs over a sum of sequential potential pulses [13].

It is important to note that if the applied potential step covers some range of potential at which Faradaic reactions take place, producing a Faradaic current (i_F) (see upper curve in Figure 2.13), then the charge due to this process needs to be taken into account in the calculation of the charge entering the double-layer capacitance.

- Cyclic voltammetry experiments: In this method, the applied potential (mea-

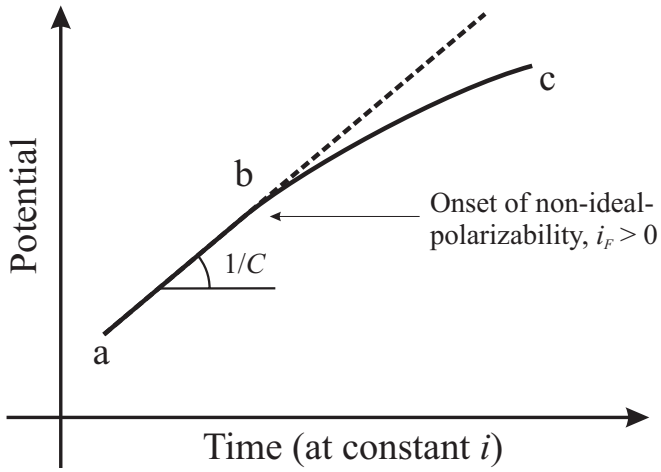

Figure 2.12: Charging curve at constant current for an electrode interface with a double-layer capacitance C. Reproduced from reference [13].

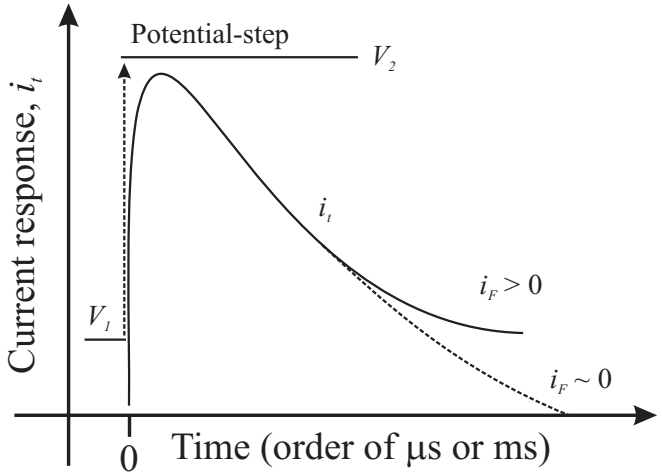

Figure 2.13: Current-response transient for charging an electrode interface using a step of potential from V_1 to V_2. Reproduced from reference [13].

sured with respect to a reference electrode) is varied linearly with time in a three electrode cell. The time-dependent current response is then recorded by a digital instrument, such as a computer, and is presented as a cyclic voltammogram (CV), which is a current vs. potential curve (see Figure 2.14). This method is also called linear potential-sweep experiment [13].

During such a cyclic voltammetry experiment the potential-sweep rate (s) is held constant and is defined by equation (2.17). The capacitive charging current (i_C) follows equation (2.18) from which the capacitance can be easily evaluated.

$$s = \frac{dV}{dt} \tag{2.17}$$

$$i = C(\frac{dV}{dt}) = Cs \tag{2.18}$$

An ideal double-layer capacitance behavior of an electrode is represented by a rectangular shape in the cyclic voltammetry curve as illustrated in Figure 2.14. The sign of the current is instantaneously reversed upon reversal of the potential sweep. This kind of behavior is purely electrostatic and current is independent from potential. In contrast, electrode materials with pseudocapacitance properties exhibit deviations of the rectangular form and also some redox peaks related with the electrochemical activity of functional surface groups. In this case the charge accumulated in the electrodes is strongly dependent on the po-

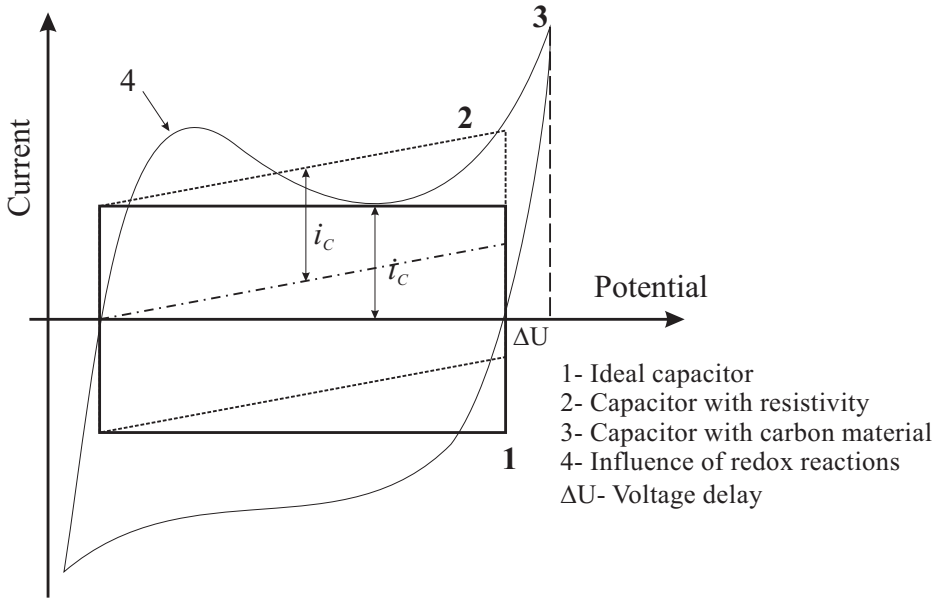

Figure 2.14: Typical cyclic voltammogram characteristics of an electrochemical capacitor. Reproduced from reference [28].

tential. The voltage delay observed in Figure 2.14 is related with a kinetically slow process involved during charging the pseudocapacitance [28].

It is important to point out that this method can be also used for testing electrochemical capacitors in a two-electrode-cell configuration. However, some considerations have to be taken into account in order to compare the results obtained from the use of the two configurations (three- and two-electrode). In a three-electrode configuration the potential applied to the working electrode (WE) with respect to a particular reference electrode (REF) is shown on the X-axis of the CV. In this case, only the WE contains the material being analyzed. In a symmetrical two-electrode cell the potential differences applied to each electrode are equal to each other and are one-half of the value shown on the X-axis of the CV. Consequently, for a given potential range shown on the X-axis of a CV, the potential range applied to the WE in a three-electrode cell is twice of that which would be applied in a two electrode cell leading to a doubling of the calculated capacitance [29].

- Self-discharge experiments: In such experiments where the electrochemical capacitors are discharged only over a known load resistance (R) the time dependence on potential is described by (2.19) from which C can be evaluated [13].

$$V(t) = V_0 \; e^{\,(-t/RC)} \tag{2.19}$$

- AC impedance methods: By applying an alternating voltage to an electrode interface, usually in a range of frequencies between 0.001 Hz and 100 kHz, an alternating current is generated from which the double layer capacitance as well as the pseudocapacitance behavior can be characterized and theoretically distinguished from each other. As mentioned before, the equivalent circuit illustrated in Figure 2.8 (b) shows a capacitive element coupled in parallel with a potential dependent reaction resistance and exemplifies an electrochemical capacitor electrode with the presence of pseudocapacitance. Such a circuit has two ranges of dispersion of impedance with frequency (ω): one at relatively high frequencies corresponding to the double-layer capacitance (C_{dl}) and a second one over low frequencies corresponding to the pseudocapacitance (C_Φ) and the reaction resistance (R_F). The response of these two elements are often resolvable in a complex-plane plot of the real and imaginary components of the impedance [13]. In this way, for such behavior the C_{dl} and C_Φ components can be distinguished. In general, in an ac impedance experiment the imaginary component of the impedance (Z'') is determined by equation (2.20). The real

component (Z') is ideally infinity for an ideally polarizable electrode. In this equation $j = \sqrt{-1}$.

$$Z'' = \frac{1}{j\omega C} \tag{2.20}$$

2.3 Hybrid systems involving supercapacitors

The combination of different technologies of energy storage, such as supercapacitors and batteries, pursues an extension of the energy-power performance rating of the system. Battery systems posses a high energy density but low power densities, in contrast, electrochemical capacitors have the ability to produce much higher power densities (see Figure 2.15) and exhibit considerably fewer material stability problems [30]. A hybrid system between the two elements should theoretically permit the energy of a battery to be released at the higher rate of energy delivery of the electrochemical capacitor. In this way, electrochemical capacitors and batteries should be considered as complementary technologies, since each provides a unique solution to energy storage [30].

Two types of hybrid battery/capacitor systems are recognized [32]:

- A hybrid system based on the combination of an electrochemical capacitor cell with a rechargeable battery or a fuel cell in a parallel way operating in a load-leveling function, for example, in an electric vehicle (EV) power train.

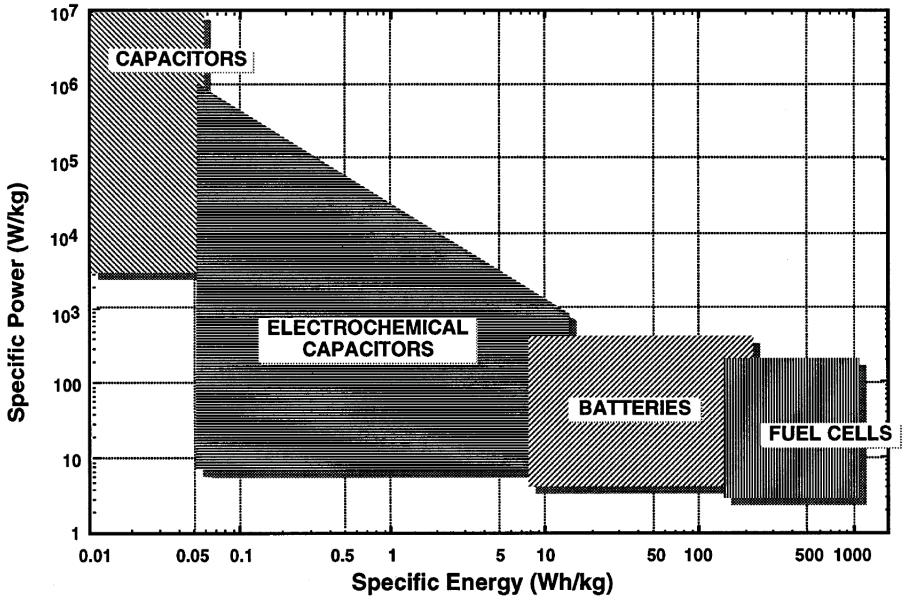

Figure 2.15: Ragone type plots for various energy storage devices. Reproduced from reference [31].

- A hybrid system (known as asymmetric capacitor) based on the combination of a Faradaic rechargeable battery-type electrode, for example, acid $PbO_2/PbSO_4$ or alkaline $NiOOH/Ni(OH)_2$ coupled internally with a non-Faradaic or pseudo-Faradaic capacitive electrode in a two electrode hybrid module.

The coupling of a battery or fuel cell in a parallel, but electronically interfaced way with a supercapacitor enables the fuel-cell or battery unit of an electric vehicle power system to operate at more steady conditions than it would otherwise operate as a stand-alone cell. For example, this configuration permits to minimize the fluctuations of fluxes of produced water and anode/cathode pH differences as well as non-steady H_2 and O_2 gas flux demands in the two porous electrode structures in a hydrogen-oxygen fuel cell [32]. Furthermore, the battery or the fuel cell could provide an average power output while electrochemical capacitors provide additional peak power when required. In this way, these primary power sources are not pushed to the limit of their power capabilities resulting in a longer lifetime of the system.

It is important to note that in the case of a battery-supercapacitor hybrid for EVs, normally the capacitor load-leveling component only has to match a 10-20% of the potential Faradaic charge during transient high-load periods (up-hill driving or acceleration). However, it must also be taken into account that the battery component has to recharge the capacitor component, which has its maximum power density at full state-of-charge.

The limitation described above is avoided when the capacitor component is coupled with a fuel cell also for EV applications. The fuel cell can provide controlled or programmed capacitor recharging indefinitely since it has no state-of-charge limitation of the kind observed in batteries or electrochemical capacitors. However, as mentioned above fuel cells have power profile limitations which can be avoided by coupling them with a supercapacitor.

The second type of electrical-energy-storage hybrid device described above corresponds to the so-called asymmetric capacitor. Such a system combines the advantage of a capacitor component which operates at high power density with the good energy density of a battery-electrode component and especially for the acid $PbO_2/PbSO_4$ system where the electrode potential remains relatively constant with diminishing state-of-discharge even down to ca. 90% discharge.

The use of such systems leads to an advantage with respect to availability of charge from the non-Faradaic electrode, namely, that its initial full charge is available on discharge against the Faradaic electrode compared with effectively only one quarter of full charge in conventional symmetrical double-layer capacitor devices. Considering equation (2.6) and the fact that in double-layer capacitors one high-

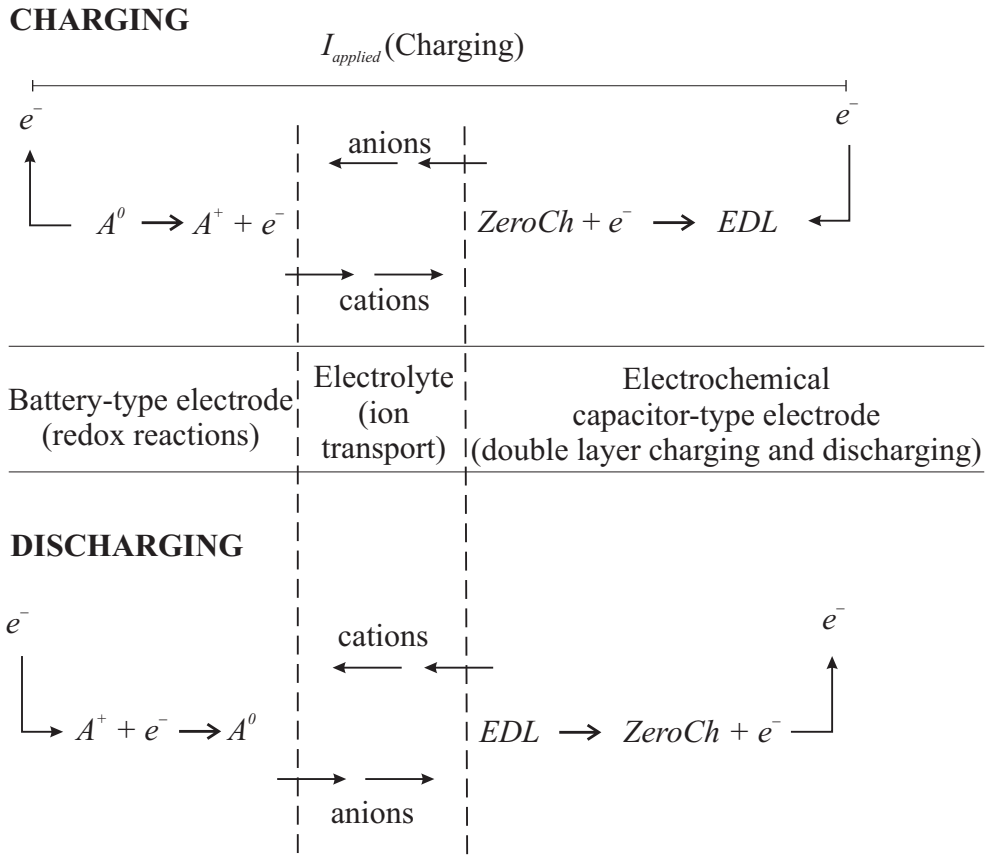

Figure 2.16: General view of the charging and discharging process of an asymmetric electrochemical system. A^+ and A^0 are the oxidized and reduced form of an active material, $ZeroCh$ means the zero charge state of the polarizable electrode, EDL represents the electrical double layer and $I_{applied}$ is the externally applied charging current.

surface-area carbon electrode is worked against another similar one, i.e. $C_1 = C_2$ (symmetrical capacitor series configuration), the measured C_{cell} will be half that of each of the components. If the second electrode corresponds to a Faradaic electrode then its capacitance (C_2) is effectively infinity, so $C_1 = C_{cell} = C_{dl}$ of the high-area double-layer electrode and the full charge stored on C_1 is therefore available for discharge, as C_{cell} against the Faradaic electrode [33]. It is important to note that in this kind of devices a sufficiently high potential or current has to be externally applied in order to keep the Faradaic reaction going at the battery electrode and to charge the double layer of the supercapacitor electrode. Once the hybrid device is charged it can be discharged over an ohmic load resistance. The charging and discharging processes in such devices are schematically illustrated in Figure 2.16.

This asymmetric electrode assembly can be also described as follows [34]:

$$A/A^{+} \mid \text{Electrolyte} \mid \text{C (carbon electrode)} \tag{2.21}$$

The most important aspect in considering the optimal conditions for coupling electrochemical capacitors with battery-type electrodes is that the electrochemical capacitor discharge follows an almost linear decline in voltage with decreasing state-of-charge, while Faradaic electrodes show a more constant electrode potential during discharge. This means that the asymmetric cells exhibit an energy- and power-density dependence on the state-of-discharge which has to be taken into account for the performance specifications and choice of application [32].

2.4 The new concept

The new fuel cell-supercapacitor hybrid concept (similar to an asymmetric capacitor cell configuration) consists of the combination of a Faradaic fuel cell-type electrode (Pt catalyst supported in carbon) coupled internally with a non-Faradaic (also pseudo-Faradaic) rechargeable supercapacitor-type electrode (high-surface-area carbon black) in a two-electrode single-cell configuration. These electrodes are separated from each other in the cell by a Nafion® membrane in contact with an aqueous electrolyte. No information was found in the literature concerning this specific hybridization between a fuel cell and a supercapacitor as we apply it in our concept.

This concept was conceived as a hydrogen storage system which could serve as a hydrogen buffer for fuel cell applications. The chief advantage of this concept is that it operates spontaneously, i.e. without applying any current or voltage, and reversibly at ambient temperature and pressure.

A general view of the process involved during charging and discharging this hybrid system is shown in Figure 2.17 and its operating principle is schematically illustrated in Figure 2.18. Hydrogen gas is oxidized at the fuel cell-type electrode acting as an anode, the protons are transported through the proton conducting Nafion® membrane and the electrolyte towards the supercapacitor-type electrode (carbon black) surface where the electroactive oxygen-based functionalities which exhibit pseudo-capacitive behavior are reduced. Simultaneously, the electrons are transferred via an external circuit onto the carbon black. The electrical double layer is then formed by storing protons in the aqueous phase and electrons onto this electrode, a process that can be controlled by a potentiometer and a switch (see Figure 2.18). For discharging, the electrons are transported back to the fuel cell-type electrode performing electrical work. At the same time the protons are transported back through

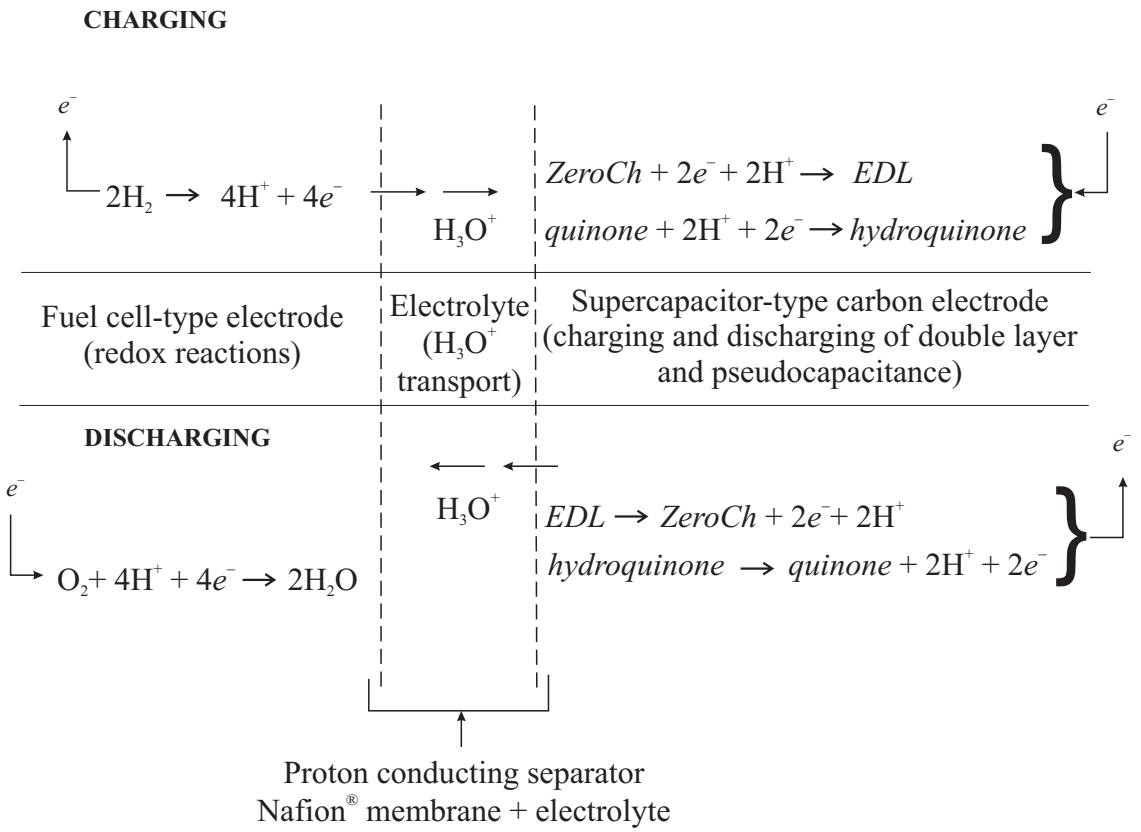

Figure 2.17: General view of the charging and discharging process of the new asymmetric electrochemical system. $ZeroCh$ means the zero charge state of the polarizable electrode, EDL represents the electrical double layer. No external current or voltage is applied. Quinone/hydroquinone redox reaction symbolizes the pseudocapacitance behavior of oxygen-based electroactive surface groups present in the carbon.

the membrane and recombine on the fuel cell-type electrode surface (former anode acting now as cathode) with electrons and O_2 (from the air) producing water and heat. This electrochemical system can be represented in a similar way as in (2.21) as follows:

$$H_2/O_2 \mid \text{Nafion}^{\circledR}112, \text{electrolyte} \mid \text{C (carbon electrode)} \tag{2.22}$$

where H_2 is used during the charging process and O_2 (from the air) is used during discharging.

It is important to point out that the present concept does involve hydrogen as a fuel from an external source. However, no external electrical work is applied and neither does hydrogen gas enter the storage material during charging, nor does hydrogen leave it during discharging. The recombination of protons at the carbon

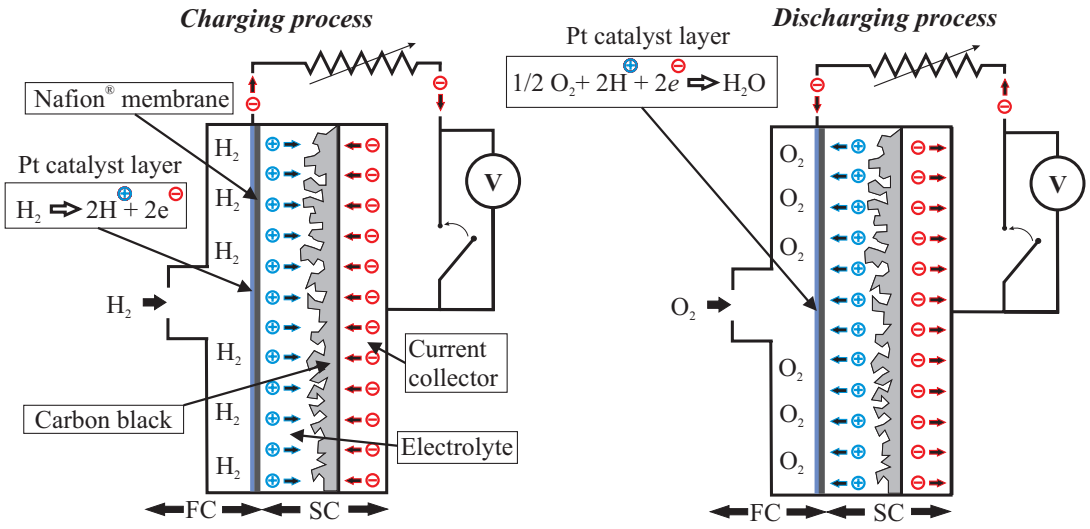

Figure 2.18: Operating principle of charging and discharging the two-electrode fuel cell-supercapacitor hybrid capacitor. FC and SC symbolize the fuel cell-type electrode and the supercapacitor-type electrode respectively.

surface is not expected to take place at the measured open circuit voltage (< 1 V) due to the high hydrogen overpotential of the carbon material [35]. It is also estimated that electroactive functionalities at the carbon surface play a role during charging and discharging the cell. As mentioned in previous sections, redox couples, such as quinone/hydroquinone, contribute to the overall capacitive performance in form of pseudocapacitance in this type of material. The overall capacitance will then have two contributions: non-Faradaic (formation of the double layer) and Faradaic (redox reactions at the carbon surface).

We now present a simple theoretical estimation of the potential and the limits of such a storage device. Preliminarily we assume that all carbon atoms are exposed to the surface and that one positive or negative charge can be stored per surface carbon atom. The ions derived from one water molecule compensate these charges, so we need one H_2 atom per one C atom and one H_2O molecule, which is an ultimate limit and equivalent to a theoretical storage capacity of 3.33 wt.% relative to the total storage material (or 8.33 wt.% if it is referred to only the carbon material). Similar saturation values have been reported for cryo-physisorption of H_2 on carbon or organic molecular framework materials at 77 K and pressures exceeding 50 bar [3, 36], while at ambient temperature and pressure these materials adsorb less than 0.01 wt.%.

The hydrogen storage process in this system can be represented using chemical equilibria. Taking into account the species involved in neutral, acidic and alkaline

conditions, equilibrium (2.23), (2.24) or (2.25) are suggested.

At neutral conditions (when only water is used) it is expected that the negative charges accumulated on the carbon storage material during the charging process attract the protons to balance the charge and drive the equilibrium (2.23) further to the right. The same behavior is expected to happen at acidic and alkaline pH, as denoted by equations (2.24) and (2.25), respectively, with the difference that a high concentration of ions is already present in the solution at the beginning of the experiments. The redox reactions of the pseudocapacitive surface functional groups (>C=O) are also considered. Increasing hydrogen pressure could serve also to drive these equilibria further to the right.

- Start with a neutral electrolyte:

$$\begin{aligned} \mathrm{H_2 + H_2O + C + {>}C{=}O} &\rightleftharpoons \tfrac{1}{2}\mathrm{H_2 + H_3O^+ + C^- + {>}C{=}O} \rightleftharpoons \\ &\rightleftharpoons \mathrm{H_3O^+ + C^- + {>}C{-}OH} \end{aligned} \tag{2.23}$$

- Start with an acidic electrolyte:

$$\begin{aligned} \mathrm{H_2 + H_3O^+ + H_2O + C + {>}C{=}O} &\rightleftharpoons \tfrac{1}{2}\mathrm{H_2 + 2\,H_3O^+ + C^- + {>}C{=}O} \rightleftharpoons \\ &\rightleftharpoons \mathrm{2\,H_3O^+ + C^- + {>}C{-}OH} \end{aligned} \tag{2.24}$$

- Start with an alkaline electrolyte:

$$\begin{aligned} \tfrac{3}{2}\mathrm{H_2 + OH^- + C + {>}C{=}O} &\rightleftharpoons \tfrac{1}{2}\mathrm{H_2 + H_2O + H_3O^+ + C^- + {>}C{=}O} \rightleftharpoons \\ &\rightleftharpoons \mathrm{H_2O + H_3O^+ + C^- + {>}C{-}OH} \end{aligned} \tag{2.25}$$

The reaction should be reversed when the hydrogen pressure decreases. Alternatively, by replacing hydrogen by oxygen or air it is expected that the equilibrium will also reverse and use the protons under formation of water, leaving oxygen anions or hydroxide ions in the cell. This is the fuel cell cathode reaction which provides electrical power when the current is discharged over a load.

An extension of this concept is the combination of a non-Faradaic supercapacitor-type electrode with two fuel cell-type electrodes in a single cell. The supercapacitor-type electrode is then coupled internally and placed between two Faradaic fuel cell-type electrodes which act as an anode and cathode respectively in a three electrode single-cell configuration. Such a device is a complete fuel cell in which the supercapacitor-type electrode capable to store hydrogen is inserted between cathode and anode, where it serves as a hydrogen buffer.

This device can be operated as a typical PEM fuel cell when the supercapacitor-type electrode is disconnected. The cathode and anode electrode assemblies (catalyst-coated Nafion® membranes) are separated by a graphite electrode with holes (filled by electrolyte in order to assure the proton conduction) which also serves as current

collector for the supercapacitor-type electrode (carbon black). In this way the buffer may be loaded continuously, even in a slow process, for example, when the fuel at the anode is methanol. The cathode side has its own electrical circuit and can be operated independently, allowing the buffer to be tapped on peak power demand. Figure 2.19 illustrates the operating principle of this cell. For more details about the experimental setup see section 3.4.

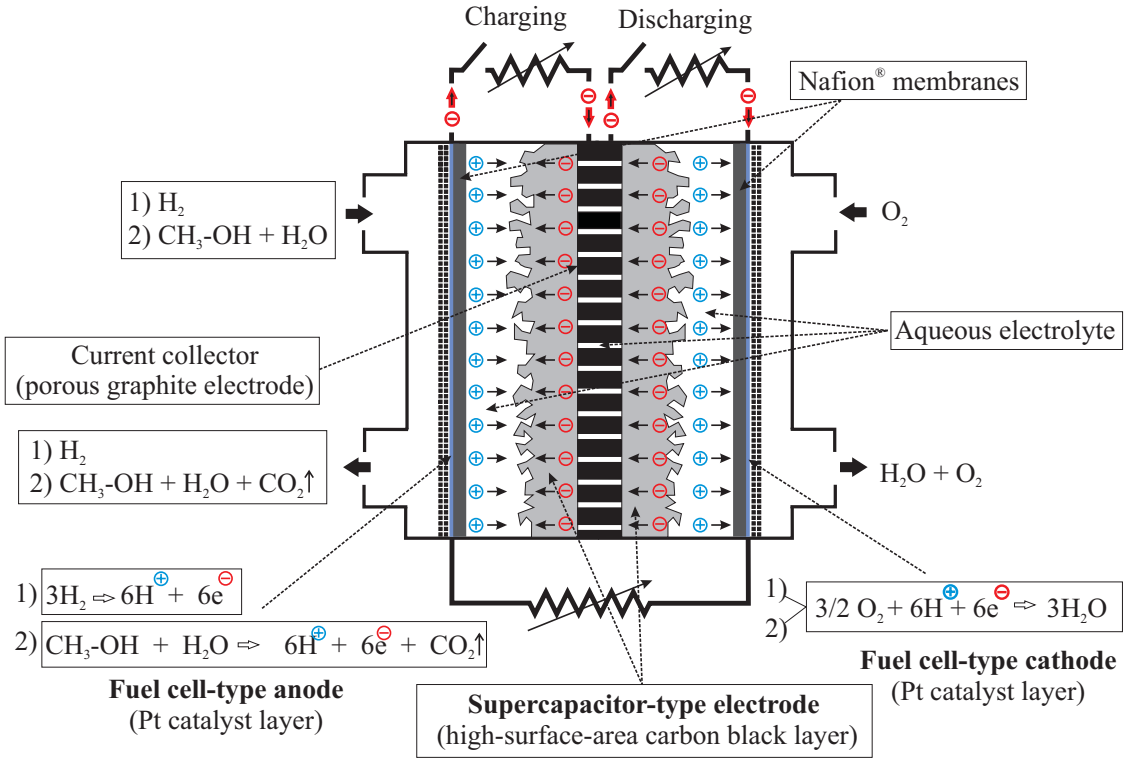

Figure 2.19: Schematic diagram of the three-electrode fuel cell-supercapacitor hybrid cell.

3 Experimental techniques

3.1 Supercapacitor-type electrode material

We investigated carbon black Black Pearls 2000 (BP) from CABOT Corporation, and Printex XE-2 (PX) from EVONIK-DEGUSSA Corporation as supercapacitor-type electrode material. Both carbon blacks were used as received and characterized by N_2 adsorption isotherms using a Micromeritics ASAP 2000 instrument. Prior to the adsorption experiments, the samples were degassed at 450 °C and 10^{-6} bar for 20 hours.

3.2 Catalyst coated membrane preparation

One-side catalyst coated membranes were prepared by spray-coating of the catalyst ink onto only one side of heated Nafion® 112 membranes [37]. Non-teflonized carbon cloth was used as gas diffusion layer (GDL). The catalyst coating of the membrane represents the fuel cell-type electrode.

3.2.1 Catalyst ink

The catalyst ink was prepared by dispersing commercially available supported catalyst (Alfa Aesar Pt 20 wt.% in carbon black Vulkan XC72R) in doubly-distilled deionized water. Nafion® solution (Aldrich 10 wt.% dispersion in water) was added to obtain the desired concentration of Nafion® in the ink (about 28-30 wt.%). Nafion® was used in order to bind the electrode and provide proton conductivity to the active layer.

The catalyst ink was then stirred for at least 24 h in order to obtain electrode layers with sufficient binding to the electrolyte. However, too extensive stirring time ($>$ 2 weeks) can lead to undesired changes in the powder morphology and blocking the spraying nozzle [37].

3.2.2 Membrane pretreatment

In order to clean the proton conducting Nafion® membranes before being used, the following standard procedure was applied: treatment of the membrane in boiling 5 vol.% H_2O_2, doubly-distilled deionized water, and then in boiling 0.5 M H_2SO_4 and doubly-distilled deionized water for 1 hour in turn. The pretreated membranes were kept in doubly-distilled deionized water prior to the coating procedure [38, 39].

3.2.3 Spray-coating method

The experimental setup used for the spray-coating of the membranes included a 10 cm × 10 cm aluminum frame (1) (see Figure 3.1) which had regularly spaced round orifices and was connected to a vacuum system (2). The frame was also in contact with a hot plate (3) and a temperature control (4). A wet membrane was fixed in the aluminum frame, the temperature was set to 90 °C and the vacuum system was turned on to hold the membrane in place and support the drying process. The membrane was then left to dry for about 1 hour under these conditions. Then it was removed from the frame, left to cool in the air for 15 min and weighed.

After the membrane had been weighed, it was placed again in the aluminum frame, the same conditions as for the drying process were set and then it was spray-coated with the catalyst ink in several layers using a spraying nozzle (5). We used a Teflon® mask (6) in order to coat a desired area or electrode form onto the membrane. The spray-coating procedure took approximately 1 hour, then the membrane was left to

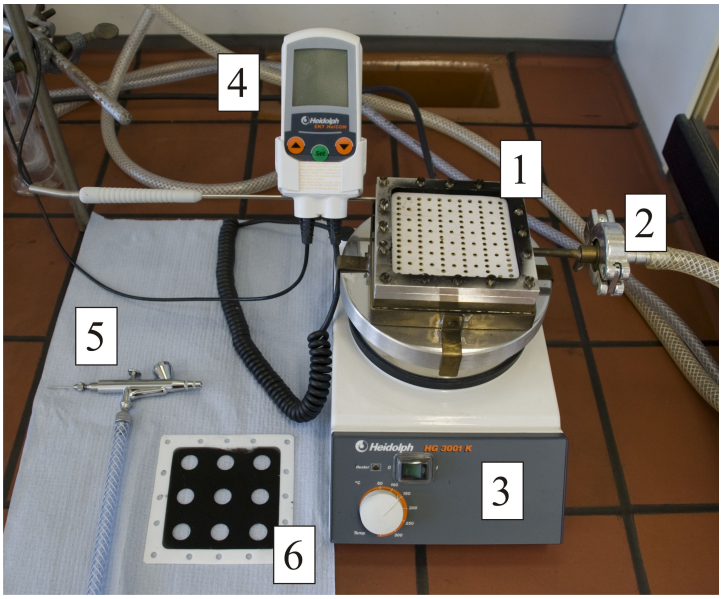

Figure 3.1: Spray-coating method setup

dry for 1 hour under these conditions. The vacuum system and the hot plate were turned off and the membrane was left for 24 hours in the frame and then weighed again.

The catalyst loading was calculated by comparing the weight of the dried membrane before and after the spray-coating procedure. It could also be estimated using the difference in weight of the Teflon® mask before and after the spray-coating procedure. Catalyst coatings with a Pt loading of about 0.45 mg cm^{-2} and a geometrical area of 1.33 cm^2 were obtained.

3.3 Two-electrode fuel cell-supercapacitor hybrid cell

The two-electrode cell consists of two hollow Plexiglas cylinders (2 cm high, 2 cm outer and 13 mm inner diameter; Figure 3.2). The hydrogen gas connection, the electrical contact A (Pt wire) and the gas diffusion layer (carbon cloth) were mounted in the upper part. The supercapacitor-type electrode, the current collector (glassy carbon disk, Sigradur G obtained from HTW, Germany) and the electrical contact B (Cu foil) were placed in the lower part. A one-side catalyst coated Nafion® 112 membrane was placed in between. The catalyst coating (fuel cell-type electrode) was in contact with the carbon cloth and the electrical contact A. Once the cell was assembled, both compartments were sealed using O-rings between Plexiglas cylinder and membrane. All experiments were performed using ultra pure hydrogen gas (99.999 vol.%).

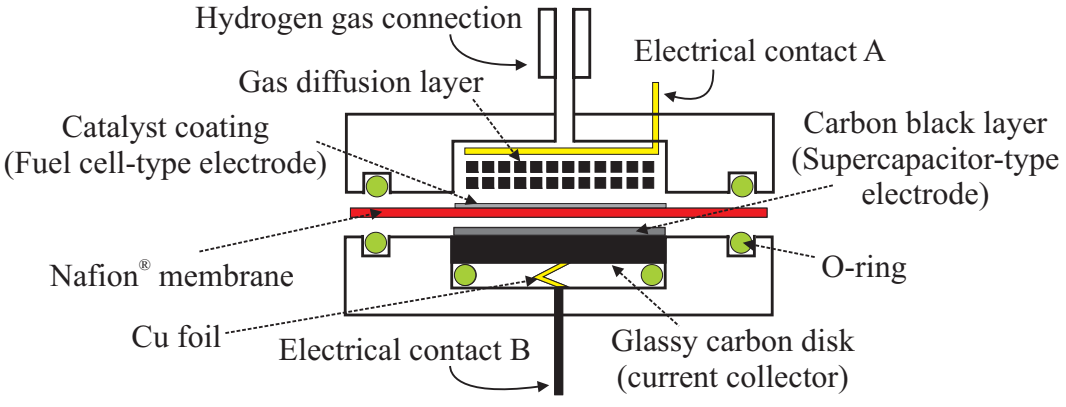

Figure 3.2: Schematic diagram of the two-electrode hybrid cell.

3.3.1 Supercapacitor-type electrode preparation

The supercapacitor-type electrode was formed from ultrasonically homogenized aqueous suspensions (1.00 mg cm^{-3}) of carbon black (BP and PX). These were pipetted in the quantity of 3.76 cm^3 cm^{-2} onto the glassy carbon disk, which was used as current collector because of its high overpotential of H_2 evolution. The applied suspensions were left to dry in the air at room temperature [40]. Supercapacitor-type electrodes with different carbon black loadings (between 0.4 and 3.8 mg cm^{-2}) and thicknesses (between 0.1 and 1 mm) were prepared. Before assembling the cell, doubly-distilled deionized water or electrolyte was added to this electrode (6.0 cm^3 liquid per gram C). We used 7 M H_2SO_4 and 7 M NaOH as electrolyte.

3.3.2 Electrochemical measurements of the two-electrode hybrid cell

An Amel Instruments model 7050 potentiostat, in two-electrode mode, was used to monitor the open circuit voltage (OCV) and the current in function of time. It was also used in the same configuration for the galvanostatic and cyclic voltammetry experiments. All measurements were performed at room temperature.

Figure 3.3 shows the schematics of the setup used in these experiments. The working electrode terminal of the potentiostat (WE) was connected to the electrical contact A through a 10 Ω resistance. The counter and reference electrode terminals (CE and REF, respectively) were connected to the supercapacitor-type electrode.

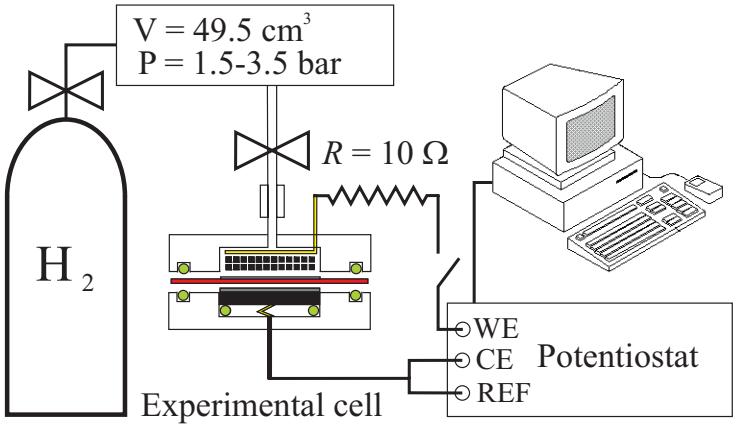

Figure 3.3: Schematic diagram of the experimental setup.

Charging-discharging experiments

At the beginning of the experiment, when the gas compartment was open to the atmosphere, the OCV was measured (we will refer to this as ΔV_0). Then the cell was connected to the pressure control system, the air was evacuated and a H_2 pressure between 1.5 and 3.5 bar was applied. The OCV was measured again (we will refer to this as ΔV_{H_2}). After closing the circuit, we measured the spontaneous charging current in function of time.

After 10 min the current sampling was stopped and the circuit was opened. The H_2 was evacuated and the gas compartment filled with air from the atmosphere. The OCV was measured again (we will refer to this as ΔV_{air}). Then the circuit was closed and the spontaneous discharging current was monitored over 10 min. The two-electrode hybrid cell was charged and discharged repeatedly by following the procedure described above. The H_2 pressure inside the pressure control system was monitored during the charging process using a manometer with a detection limit of 1 mbar.

Galvanostatic experiments

The setup of the galvanostatic experiments was similar to that described in the previous section. The WE terminal was connected to the electrical contact A without any resistor and the CE and REF terminals were connected to the electrical contact B. The air was evacuated and a H_2 pressure of 2.5 bar was applied via the pressure control system. An anodic current of 4 A g^{-1} was applied and held constant for at least 300 s. The cell voltage was then monitored in function of time.

Cyclic voltammetry experiments

In these experiments we used the same setup as in the galvanostatic experiments. The cell was connected to the pressure control system, the air was evacuated and a H_2 pressure of 2.5 bar was applied. Cyclic voltammograms were obtained in the potential window between 0 V and -0.5 V with a scan rate of 0.02 V s^{-1}.

3.4 Three-electrode fuel cell-supercapacitor hybrid cell

The three-electrode cell was a modified design of the two-electrode cell (see Figure 3.4). This configuration permitted the charging and discharging of pseudo-faradaic supercapacitor-type electrode without evacuating and changing the content

of the gas compartment. It was also made of Plexiglas and consisted of two cubical parts where the gas connections and the electrical contacts of the anode and cathode (gold wires of 0.2 mm diameter winded in spiral form), respectively, were placed. The third part was a Plexiglas sheet (2 mm thick) which held the current collector. A 3D illustration of the three-electrode cell is shown in Figure 3.5. A graphite disk of 2 mm thickness and 13 mm diameter with 18 regularly spaced holes of 0.40 mm radius each was used as current collector of the supercapacitor-type electrode. The geometrical area of the disk was 1.33 cm^2. The area without holes was 1.23 cm^2, which corresponds to an open ratio of 7.5%. As shown in Figure 3.6, the electrical contact was made through a Pt wire. The cell was sealed using O-rings, which were placed between Plexiglas and membrane.

3.4.1 Supercapacitor-type electrode preparation

Supercapacitor-type electrodes for the three-electrode hybrid cell were prepared by spreading a mixture of water and carbon black (ca. 6-10 mg C in ca. 100-120 μl) on both sides of the graphite disk with a spatula. The orifices of the graphite disk were reopened with a plastic needle. Before assembling the cell the holes were filled with electrolyte (ca. 2 μl each). Some extra electrolyte (ca. 5.0 cm^3 liquid per gram C) was added in order to maintain the carbon black wet.

3.4.2 Electrochemical measurements of the three-electrode hybrid cell

A Fluke digital multimeter model 189, connected to a computer with a data logging software (Fluke View Forms), was used to measure the fuel cell current in function of time during the fuel cell performance experiments. The internal resistance of this multimeter was 2.5 Ω. With this instrument it was possible to record up to one point per second. The voltages in other parts of the circuit were monitored with a Philips PM2525 multimeter and/or a Keithley 195A digital multimeter.

In the experiments of charging and discharging the supercapacitor we measured the current indirectly using an Amel Instruments model 7050 potentiostat in open circuit voltage measurement modus. The voltage through a known resistor connected to the cell was then measured in function of time. With the potentiostat it was possible to record up to 100 points per second, increasing the measurement resolution by a factor 10^2.

In all experiments the H_2 flow through the anode was set to 0.375 l h^{-1} and the O_2 flow through the cathode to 0.157 l h^{-1} using calibrated rotameters (model V-100)

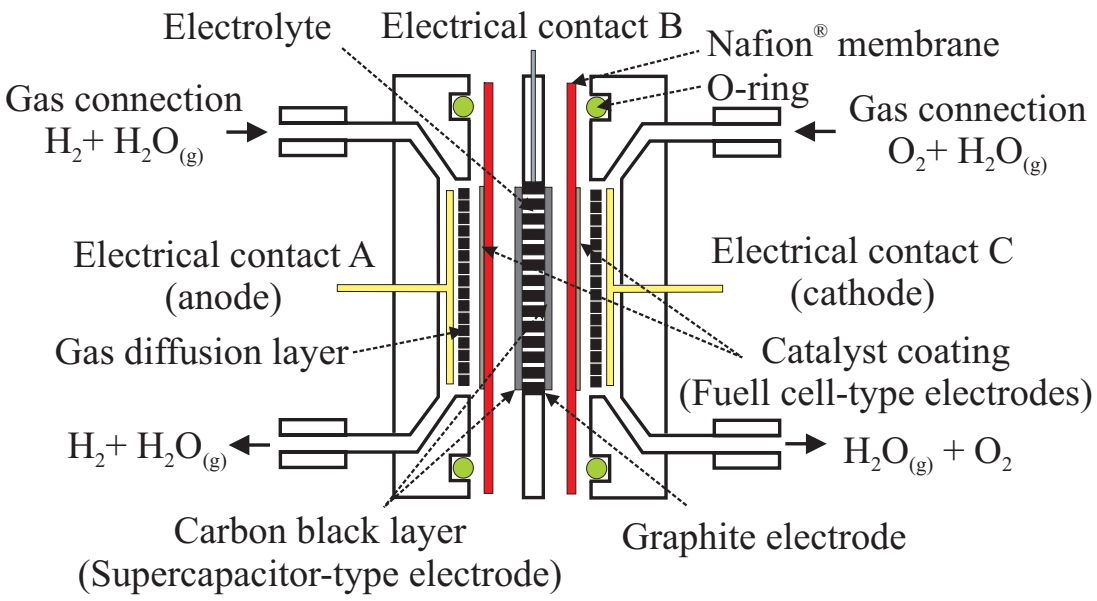

Figure 3.4: Schematic diagram of the three-electrode cell.

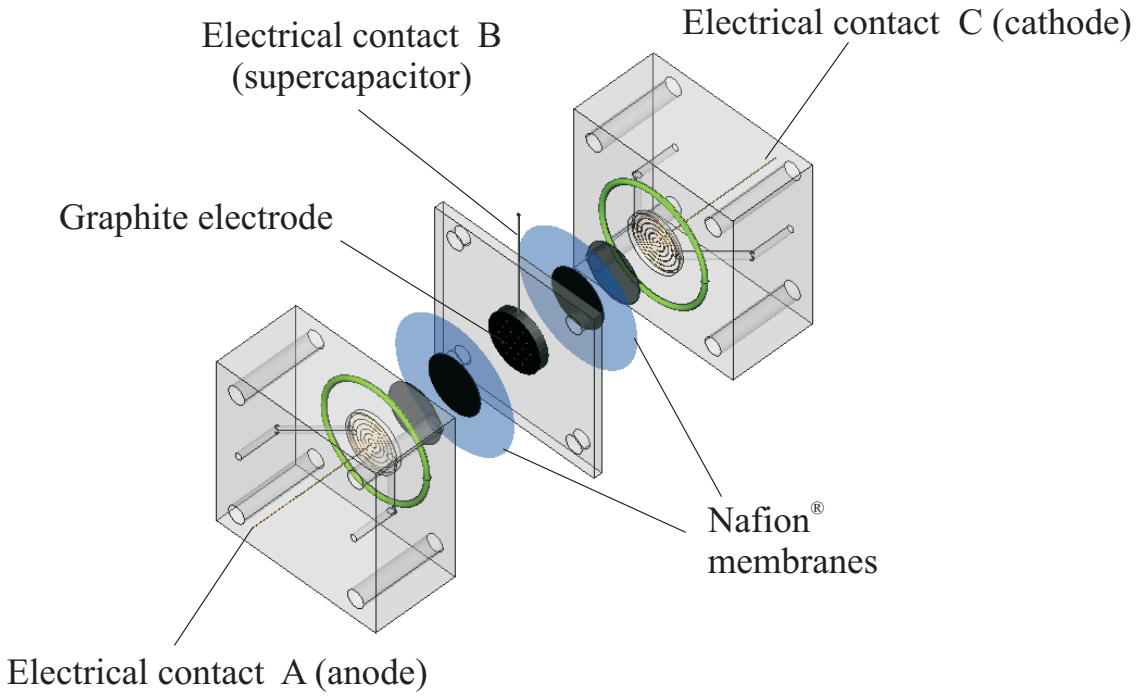

Figure 3.5: Schematic 3D diagram of the three-electrode cell.

from Voegtlin, Switzerland. The relative humidity of each gas was previously set to 70-80% using a U-glass gas humidification system schematically illustrated in Figure 3.7.

Performance of the three-electrode hybrid cell operated as a fuel cell

In these experiments we studied the influence of the concentration of H_2SO_4 on the performance of the three-electrode cell operated as a fuel cell without connecting the supercapacitor-type electrode (S). The objective was to find the optimal conditions at which the cell exhibited the highest performance. We varied the concentration of H_2SO_4 between 0.1 and 15 M. The optimal H_2SO_4 concentration was then used in further experiments. Figure 3.8 shows the experimental setup. After the preparation of the supercapacitor-type electrode, the cell was assembled and the H_2 and O_2 flows were set to the values mentioned above.

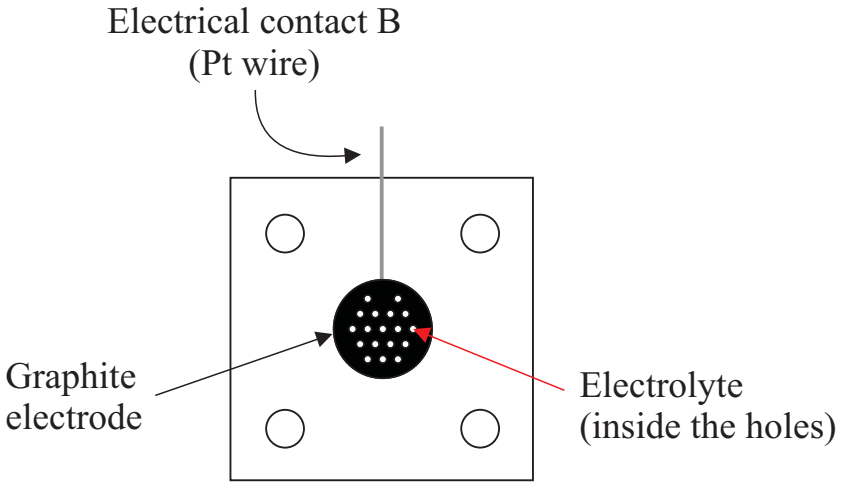

Figure 3.6: Graphite electrode of the three-electrode cell.

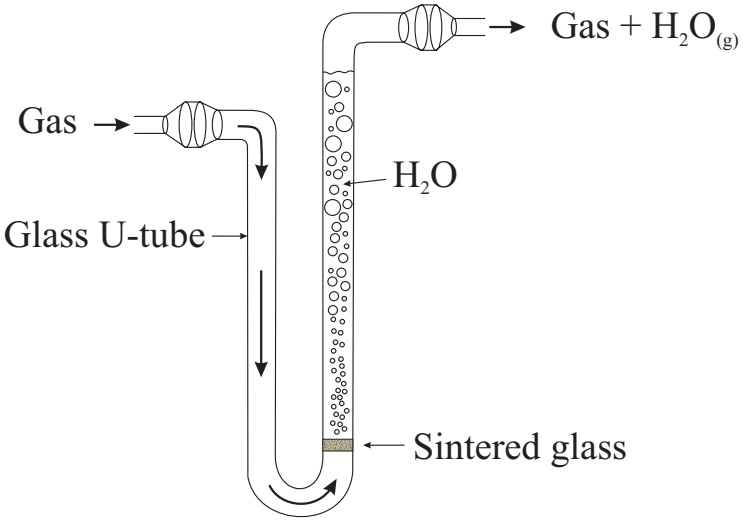

Figure 3.7: Schematic diagram of the gas humidification system used for H_2 and O_2.

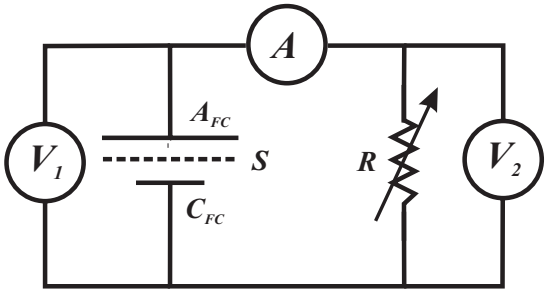

Figure 3.8: Experimental circuit of the fuel cell performance experiments.

The voltage between anode (A_{FC}) and cathode (C_{FC}) was monitored with V_1, the current with the multimeter A and the voltage in the variable resistor R with V_2. The electrode S remained disconnected during these experiments. With this experimental setup it was possible to change the resistance R and measure the voltage and current of the fuel cell. The value of the resistance R was calculated using Ohm's law, the current measured in A and the voltage observed as V_2.

Charge-discharge experiments of the three-electrode hybrid cell operated as a supercapacitor

With these experiments we studied the charge-discharge behavior of the three-electrode cell operated as a supercapacitor. The A_{FC} and C_{FC} were disconnected from each other. We used the circuit setups shown in Figure 3.9 a) for charging and b) for discharging. The voltage between A_{FC} and S was monitored during the charging process as V_C. As described before, the current was measured indirectly by measuring the voltage in function of time in R with a potentiostat. The resistance R

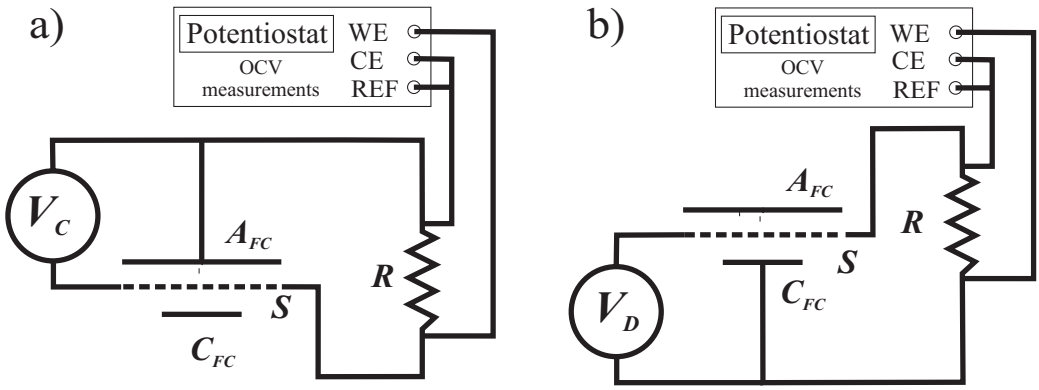

Figure 3.9: Experimental circuits used for a) charging and b) discharging of the three-electrode cell operated as a supercapacitor.

was 5.5 Ω. The voltage V_D between C_{FC} and S was monitored during the discharging process with a multimeter and the current in function of time indirectly with the potentiostat. The reproducibility and reversibility of the charging and discharging process were tested over 100 cycles using a 1.16 Ω resistance.

Charge-discharge experiments of the three-electrode hybrid cell operated as a hybrid

The charging-discharging behavior of the three-electrode cell operated as a supercapacitor and simultaneously as a fuel cell was investigated. For reasons of simplicity we will subsequently refer to the three-electrode cell operated as a supercapacitor as "supercapacitor" and to the three-electrode cell operated as a fuel cell as"fuel cell". The circuit setup shown in Figure 3.10 was used in order to determine the potential of the supercapacitor as an extra power source at different fuel cell currents (i_{FC}). This extra power source could be used independently from the fuel cell operation. When S was disconnected (switch W opened in Figure 3.10), the fuel cell current (i_{FC}) could be set to different values by changing the resistance R. When the switch W was placed in position (1), the charging current (i_{CH}) flowed through a 5.0 Ω resistor (R_S). After about 2 min, when the charging process was finished, the switch was placed in position (2). The discharging current (i_{DCH}) flowed through the resistor R_S. The i_{FC}, i_{CH} and i_{DCH} were measured indirectly using the potentiostat. The power developed in R_S during charging and discharging of the supercapacitor was then calculated at different values of i_{FC}.

In order to explore the potential of the supercapacitor also as an extra power source in function of the i_{FC}, the setups shown in Figure 3.11 and 3.12 were designed. In this case, the total power developed in R_{CH} with the switch in position (1) or R_{DCH} with the switch in position (2) resulted from two sources: the power

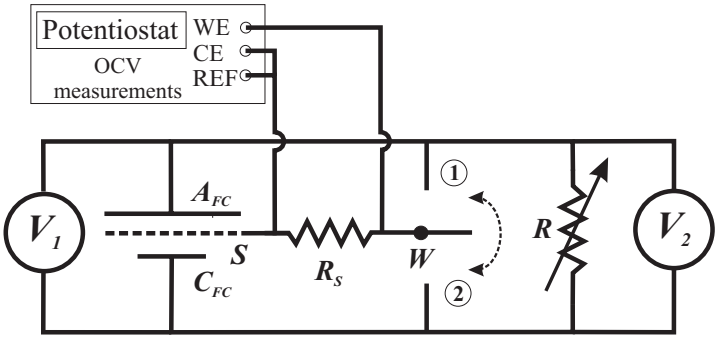

Figure 3.10: Experimental circuit of the three-electrode cell charging-discharging experiments.

generated by the fuel cell and the power generated by charging or discharging the supercapacitor. The resistance of both R_{CH} and R_{DCH} was 5.0 Ω.

In both experiments, the i_{FC} was first set to a specific value by varying the resistance R. The i_{FC} was measured in the same way as in the previous experiments. When the switch W was open, the i_{FC} flowed through R_{CH}. As soon as W was placed in position (1) also i_{CH} flowed through the resistor R_{CH} and a total current (i_{CH} + i_{FC}) was then measured. After the charging process was finished (about 2 min), the switch was placed in position (2) in order to discharge the supercapacitor before starting a recharging experiment. For the discharging experiments, W was first placed in position (1) in order to charge the supercapacitor. After the charging process was finished, W was placed in position (2) and the i_{DCH} flowed through the resistor R_{DCH} and a total current (i_{DCH} + i_{FC}) was measured.

In addition to these experiments, we explored the behavior of the current after interruption of the hydrogen flow in two situations: when the three-electrode cell was operated as a fuel cell and when it was operated as a hybrid (for experimental

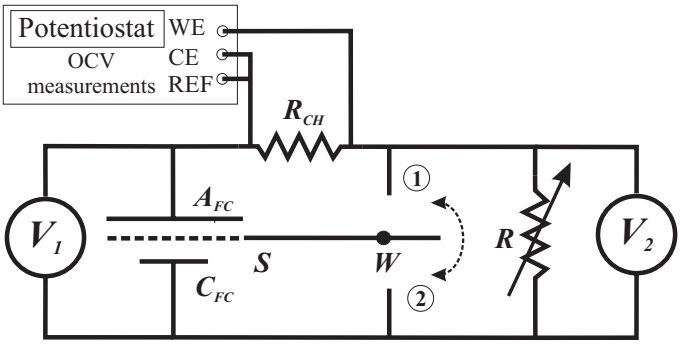

Figure 3.11: Experimental circuit setup of the three-electrode cell charging-discharging experiments to measure the charging current.

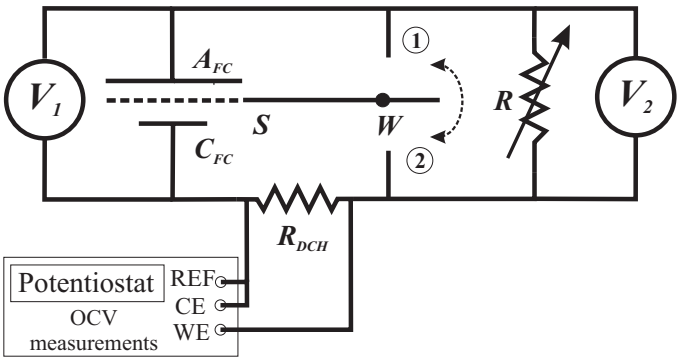

Figure 3.12: Experimental circuit of the three-electrode cell charging-discharging experiments to measure the discharging current.

setup see Figure 3.13). In both experiments the i_{FC} was first set to a specific value by varying the resistance of R.

In the first experiment the switch was open. After the i_{FC} was stabilized (about 60 s), the hydrogen flow was interrupted and the current decrease was monitored indirectly as in the previous experiments over 6 min.

In a subsequent experiment, the switch was closed after the current had stabilized and the charging process was started. After 2 min the hydrogen flow was interrupted and the decrease of the current (this time $i_{FC} + i_{DCH}$) was monitored as before.

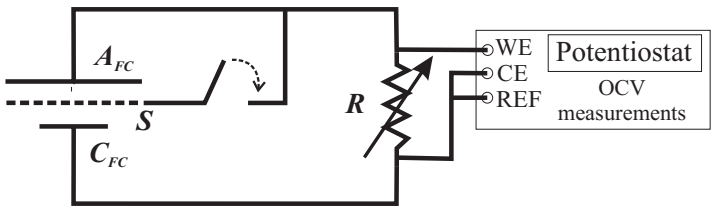

Figure 3.13: Experimental circuit of the hydrogen flow interruption experiments.

4 Experiments with the two-electrode fuel cell-supercapacitor hybrid cell

4.1 Carbon material characterization

The results of the N_2 adsorption experiments at 77 K for carbon black Black Pearls 2000 (BP) and Printex XE-2 (PX) are listed in Table 4.1. The adsorption isotherm observed for BP is shown in Figure 4.1. According to the IUPAC classification [21] the form of this adsorption isotherm corresponds to a Type II physisorption isotherm associated with monolayer-multilayer adsorption on an open external surface of a powder which can be non-porous, mesoporous or (to a limited extent) microporous. In the nomenclature used by Rouquereol et al. [41] this curve is similar to the Type IIa adsorption isotherm. At low relative pressures the isotherm rises sharply and the volume adsorbed reaches values of about 350 $cm^3\ g^{-1}$. It is usually considered that the point symbolized by A in the curve represents the formation of the monolayer. This point also indicates the beginning of an almost linear section which extends up to relative pressures of 0.7 and is associated to multilayer adsorption. At higher relative pressures (> 0.8) the curve rises again when gas condensation takes place. A relatively small hysteresis loop typically related to capillary condensation in mesopores is observed also in this region, indicating also the presence of narrow slit-like pores [41].

Taking into account the data listed in Table 4.1 these evidences suggest that a certain micro- and mesoporosity are present in BP. The results of the t-plot method show that a relatively high proportion (about 83 %) of the BET surface area corresponds to external surface area. On the other hand, taking into account the results from the BJH analysis the area of the meso- and macropores represent about 40% of the BET value. Similar values of mesoporous area (about 475 $m^2\ g^{-1}$) were observed by Wang et at. [42]. Therefore, we assume that the high BET surface area of this carbon (1155 $m^2\ g^{-1}$) is mainly due to its external surface but with an certain

contribution from mesopores and in lesser extent from microporosity.

The surface properties of BP reported from Cabot corporation are the following: BET surface area of 1500 $m^2\ g^{-1}$, pH of 9.5 and 2% of volatile content. The pH (defined by the pH of an aqueous slurry of this material measured following the ASTM D1512-80a standard test) and volatile content indicate that BP has a relatively low concentration of strong acid oxygen-based surface active functionalities such as carboxylic groups which can act as a Brönsted acid in water establishing equilibrium (4.1) [15]. The concept of a Brönsted acid can explain pH < 7 in carbon blacks, but it does not explain the pH > 7 reported for some carbon black such as BP. The alkaline pH of carbon blacks can be explained by using the concept of a Lewis base. The basal planes of the carbon with aromatic character (C_π) may function as a Lewis base capable of complexing protons to its π structure, in which case equilibrium (4.2) is considered. According to this explanation, the oxygen-based surface groups do not play a role in determining the alkaline pH of the carbon blacks. This is consistent with the observation that high pH values are found in carbon black with low volatile content [15].

$$>\!COOH + H_2O \rightleftharpoons >\!COO^- + H_3O^+ \tag{4.1}$$

$$C_\pi + 2\,H_2O \rightleftharpoons C_\pi H_3O^+ + OH^- \tag{4.2}$$

In the case of PX the observed adsorption isotherm (see Figure 4.1) has similarities to the IUPAC Type II and with the Type IIb in the nomenclature used by Rouquerol et al. [41]. The point symbolized by A also represents the formation of a monolayer. The Type IIb isotherm corresponds to the behavior exhibited by aggregates of plate-like particles having non-rigid slit-shaped pores. At low relative pressures, the volume adsorbed is about a half of that observed for BP. This isotherm exhibits a higher slope in the almost linear part between relative pressures of 0.05 and 0.6 and a more pronounced hysteresis loop which extends from relative pressures of 0.5 to 0.9. An inconsistency between the values of BET surface area, external surface area and meso- and macroporous area is observed in Table 4.1. We assume that the differences in the theoretical models considered in this calculations are the origin of these inconsistencies. From the adsorption isotherm it can be deduced that PX has a relatively high external surface area with an important presence of mesopores.

We tested two different carbon blacks in order to evaluate the effect of the surface properties in the formation of the electrochemical double layer in aqueous solution. Carbons with well developed microporosity and large surface area are commonly used as electrodes in the manufacture of supercapacitors. In such devices, a higher surface area means the possibility to form a larger double layer and therefore a

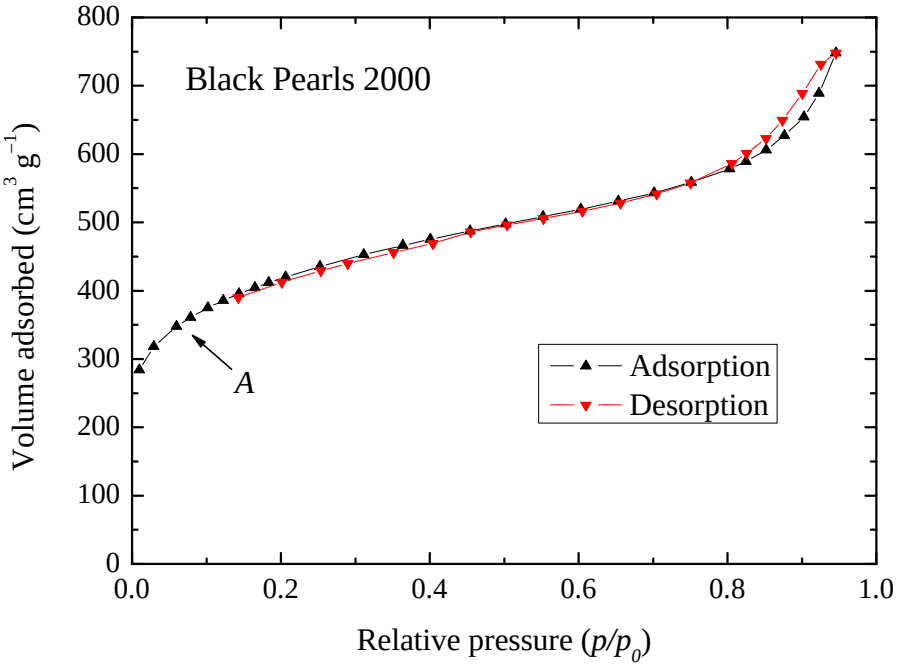

Figure 4.1: Nitrogen adsorption/desorption isotherm at 77 K on carbon black Black Pearls 2000(BP).

higher capacity.

Also the pore structure of the carbons plays a very important role in the ion

Table 4.1: Surface properties of the two carbon blacks

Carbon black	units	Black Pearls 2000	Printex XE-2
BET Surface area	(m^2 g^{-1})	1155	754
External surface area[a]	(m^2 g^{-1})	959	825
Micropore area[a]	(m^2 g^{-1})	196	-
Micropore volume[a]	(cm^3 g^{-1})	0.23	0.04
Meso- and macroporous area[b]	(m^2 g^{-1})	681	934
Meso- and macroporous volume[b]	(cm^3 g^{-1})	0.80	1.09
Average pore diameter[c]	(nm)	47	47

[a] calculated from the *t*-plot method.

[b] Meso- and macroporous area and volume are calculated from the BJH desorption pore distribution between 1.7 and 300 nm pore diameter.

[c] Average pore diameter corresponds to the BJH desorption average pore diameter.

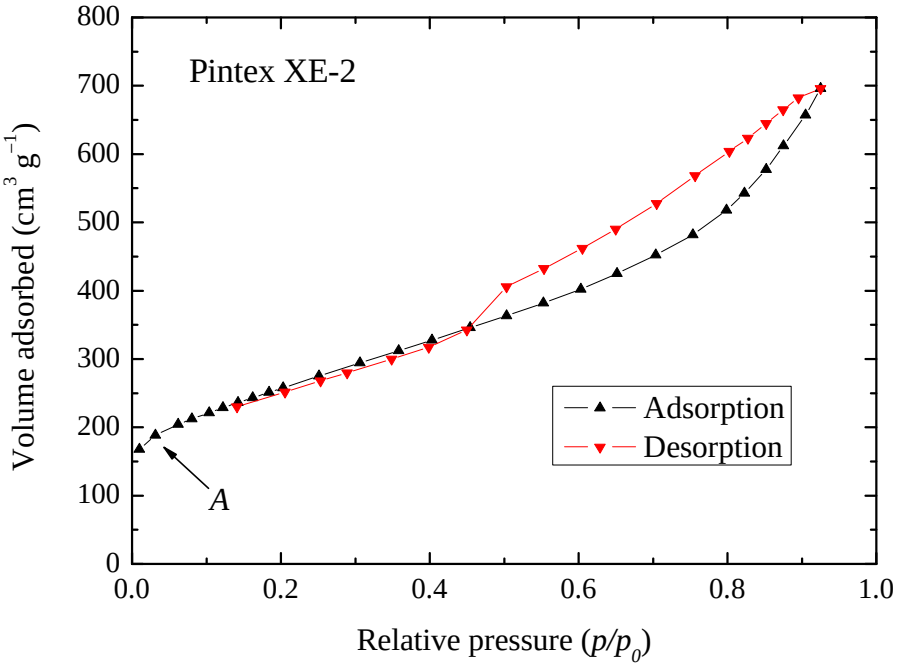

Figure 4.2: Nitrogen adsorption/desorption isotherm at 77 K on carbon black Printex XE-2 (PX).

adsorption at the exposed surface as well as in the inner surface. Although a direct relationship between the type of porosity of the electrodes and specific capacitance has not been found, pore size distribution is believed to be one of the key factors in selecting the carbon material for electrical double layer supercapacitors. Carbon materials with a combination of microporosity and also wider pores are the more suitable to high-power supercapacitor applications. The presence of wider pores should facilitate the access of the electrolyte to the inner surface of the carbon. These materials could then deliver high energy at a high rate [19]. However, other studies of experimental carbon blacks in aqueous solution have shown that there is a complex correlation between the capacitance and the surface properties of the carbons [43]. Hall et al. [30] also emphasized the complex relationship between the pores size distribution of the carbon material used for supercapacitors and the energy/power densities of these devices. These evidences indicate that several factors have an influence in the charging and discharging of the double layer of carbonaceous material in aqueous solution.

BP and PX were first evaluated as supercapacitor-electrode material in the two-electrode hybrid cell in order to investigate which one exhibits the higher hydrogen

storage capacity. We used the carbon with higher hydrogen storage capacity in further experiments.

4.2 Charging-discharging experiments using water

4.2.1 Results

Once the cell was assembled just before hydrogen was applied for the charging process an open circuit voltage (OCV) between the fuel cell-type electrode and the supercapacitor-type electrode typically in the range of +0.3 and +0.5 V was observed. As soon as a H_2 pressure was applied to the cell the OCV changed to negative values typically about −0.6 V. In the following cycles the OCV before charging increased (in absolute value) to values near to −0.8 V. After the charging process was finished, the H_2 was evacuated and then the pressure control system was opened to the atmosphere. An OCV of about +0.90 V was measured as soon as the fuel cell-type electrode was in contact with air (just before discharging). The WE terminal of the potentiostat was always connected to the fuel cell-type electrode (catalyst layer) through a 10 Ω resistor. The CE and REF terminals were connected to the supercapacitor-type electrode (carbon black).

Spontaneous anodic and cathodic currents were observed during the charging and discharging processes respectively. The result of three successive charging-discharging cycles of the two-electrode cell, shown in Figure 4.3, reveals approximately bi-exponential current-versus-time curves. The time constants τ_1 and τ_2, obtained from the bi-exponential fit to these curves, are listed in Table 4.2.

A decrease in the H_2 pressure was observed in the pressure control system during the charging process, confirming that the hydrogen is consumed at the fuel cell-type electrode. In all cases, the integrated charge (IC) of the charging curves matched the amount of consumed hydrogen. The IC of such current-versus-time plots is the area under the curve. It represents the amount of H_2 consumed at the fuel cell-type electrode during the charging process or the amount of protons consumed also at the fuel cell-type electrode to produce H_2O during the discharging process. If the current in the current-versus-time plots has units of A g^{-1} carbon, the IC is then defined as specific integrated charge (SIC).

A charging-discharging asymmetry is observed in Figure 4.3. The SIC was, in absolute value, always smaller during the discharging process than during the charging process. These results suggest that the charging process is not totally reversible and that there is a certain loss by discharging as also observed in Table 4.2. Therefore,

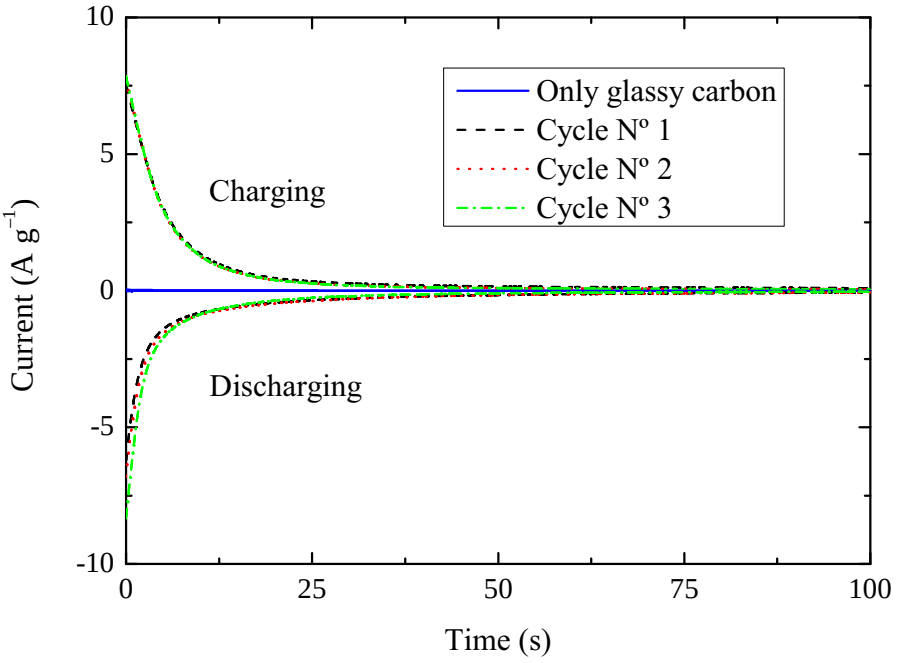

Figure 4.3: Charging-discharging curves using BP (mass loading of 3.8 mg cm^{-2}) and H_2O at 2.5 bar H_2 for charging and air at ambient pressure for discharging. In a control experiment, only glassy carbon was used as supercapacitor-type electrode.

Table 4.2: Results of the bi-exponential analysis of the data from Figure (4.3) for 3 charging (CH)-discharging (DCH) cycles. The SIC values of the original curves were calculated over 100 s. "Losses" refers to the amount of SIC in % which is not recuperated by discharging.

Cycle Nº	$\tau_{1,CH}$ (s)	$\tau_{2,CH}$ (s)	SIC_{CH} (C g^{-1})	$\tau_{1,DCH}$ (s)	$\tau_{2,DCH}$ (s)	$\mid \text{SIC}_{DCH} \mid$ (C g^{-1})	Losses (%)
1	4.95	52.56	56.38	2.10	25.37	38.07	32
2	4.68	34.49	50.87	2.08	24.08	41.25	19
3	4.66	31.56	50.99	2.00	15.54	39.22	23

we expect that during the charging and discharging of the cell different processes with different kinetics and degrees of reversibility take place.

To determine whether the current measured was a function of the amount of carbon black in the supercapacitor-type electrode, we performed charging-discharging

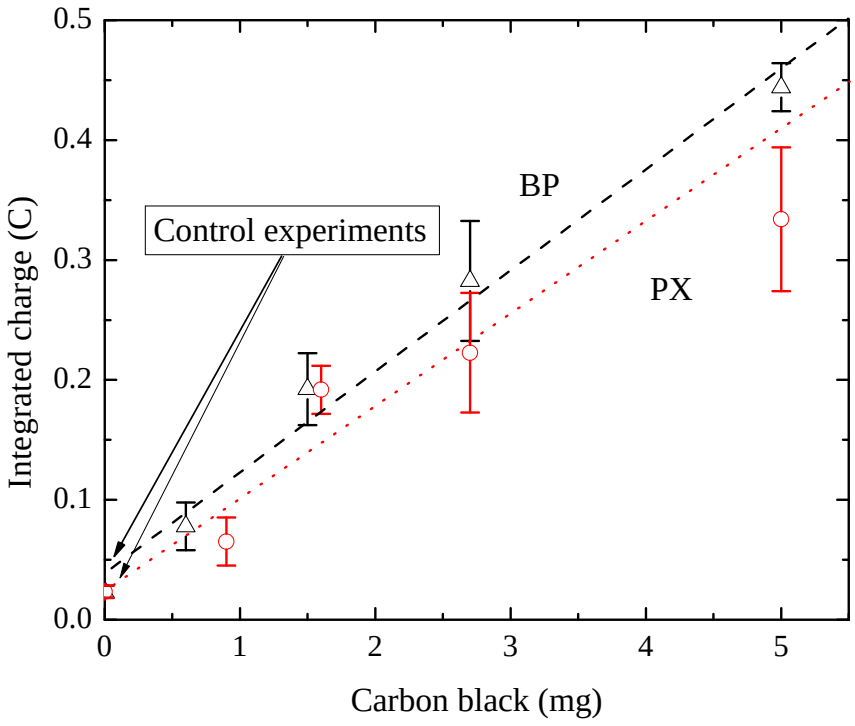

Figure 4.4: IC over 3600 s obtained with different amount of BP (open triangles) and PX (open circles) using doubly-distilled deionized H_2O at 2.5 bar H_2 during the charging process.

experiments with different BP and PX mass loadings. A control experiment (only the glassy carbon as supercapacitor-type electrode) was also carried out. In this experiment only the current collector was in contact with the Nafion® membrane.

Figure 4.4 shows good linearity between the IC and the amount of carbon black during charging experiments. The slopes of the linear fits are 0.09 and 0.08 for PB and PX respectively. We observed that the IC using BP was higher than that using PX but much less than expected based on the specific surface areas (Table 4.1). Therefore, BP was selected as supercapacitor-type electrode material for further experiments.

Figure 4.5 shows that the SIC trend to decrease when increasing amount of BP. These results suggest that not all of the carbon black present in the supercapacitor-type electrode is effectively used to form the double layer when the thickness of the carbon black layer increases. The layer thickness in these experiments was in the range of 0.1-1.0 mm.

Having in mind the equilibria (2.23), (2.24) and (2.25) proposed in section 2.4 an

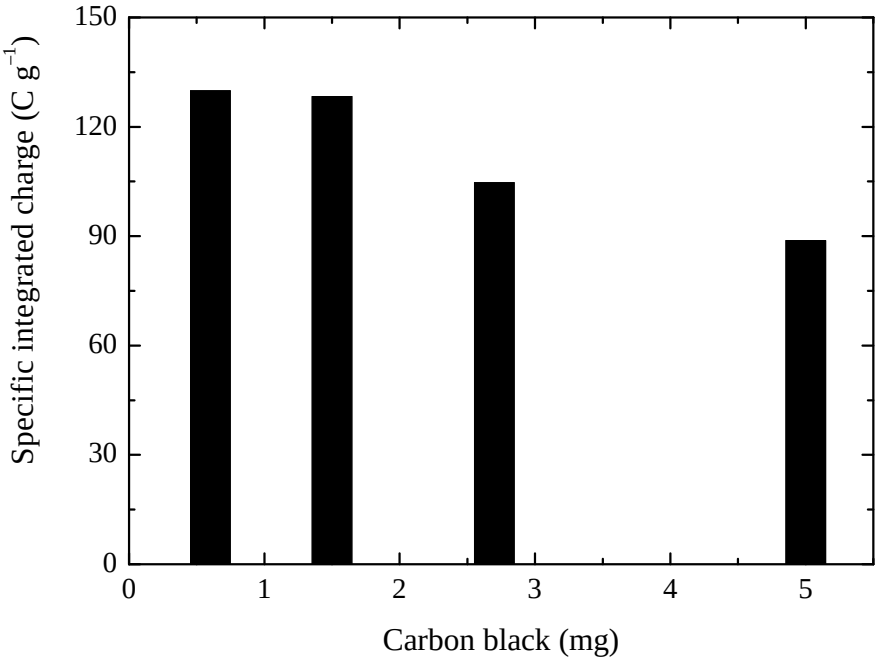

Figure 4.5: Integrated charge per gram carbon (SIC) over 3600 s obtained with different amount of BP using doubly-distilled deionized H_2O at 2.5 bar H_2 during the charging process.

increase of the hydrogen pressure would displace these equilibria further to the right, increasing the SIC and the number of protons and electrons which can be stored in the double layer. Therefore, we explored the effect of the H_2 pressure on the SIC and the hydrogen storage capacity of the cell. Charging-discharging experiments were performed under different H_2 pressures. The curves are shown in Figure 4.6. Only a slight increment in the current was noted as the H_2 pressure was increased from 1.5 to 2.5 bar. However, as the H_2 pressure was increased further to 3.5 bar a higher increment of the current was observed. The SIC values as well as the time constants derived form the bi-exponential analysis of these curves are listed in Table 4.3. The SIC values are far from proportionality with the hydrogen pressure and it seems as if the hydrogen storage is already close to saturation at 1.5 bar. It is also noted that the SIC loss between charging and discharging process at 3.5 bar is very low (about 1%) which means a higher reversibility. The origin of this effect is still not understood.

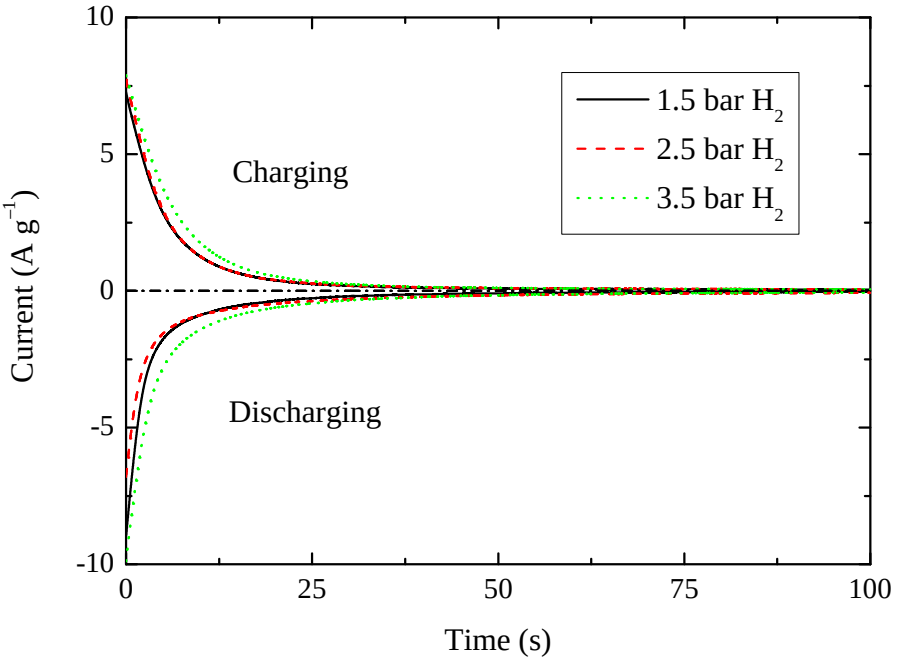

Figure 4.6: Charging-discharging curves, corresponding to the second cycle, using BP (mass loading of 3.8 mg cm^{-2}) and doubly-distilled deionized H_2O at different H_2 pressures during charging and with air at ambient pressure during discharging.

Table 4.3: Results of the bi-exponential analysis of the data from Figure (4.6) at different H_2 pressures for the charging (CH) and (DCH) discharging process. The SIC values of the original curves were calculated over 100 s. "Losses" refers to the amount of SIC in % which is not recuperated by discharging.

H_2 pressure (bar)	$\tau_{1,CH}$ (s)	$\tau_{2,CH}$ (s)	SIC_{CH} (C g^{-1})	$\tau_{1,DCH}$ (s)	$\tau_{2,DCH}$ (s)	$\mid SIC_{DCH} \mid$ (C g^{-1})	Losses (%)
1.5	4.88	31.38	48.39	1.96	15.09	40.26	17
2.5	4.68	34.49	50.87	2.08	24.08	41.25	19
3.5	6.11	45.79	61.09	2.00	15.54	60.32	1

4.2.2 Discussion

Origin of the open circuit voltage

The positive sign of the OCV observed just after the cell was assembled indicates that the supercapacitor-type electrode was charged negatively in comparison with the fuel cell-type electrode. In order to have an idea about the origin of this voltage it is necessary to consider the possible electrochemical equilibria involved at both electrodes. The fuel cell-type electrode contained Pt as a catalyst and it was in this case in contact with oxygen from air, therefore, the electrochemical reduction of oxygen in this electrode should be considered. Oxygen can be electrochemically reduced on Pt in presence of protons through a $2e^-$ or $4e^-$ catalytic path following these reactions:

$$O_2 + 2\,H^+ + 2\,e^- \rightleftharpoons H_2O_2 \qquad E^\circ = +0.695 \text{ V vs. NHE} \tag{4.3}$$

$$O_2 + 4\,H^+ + 4\,e^- \rightleftharpoons 2\,H_2O \qquad E^\circ = +1.229 \text{ V vs. NHE} \tag{4.4}$$

In the supercapacitor-electrode (made of carbon black) the following reactions involving surface electroactive oxygen-based groups such as phenolic and quinonoid (4.5), carboxylic (4.6) and ketone (4.7) groups are considered [15, 28, 43]. Without a reference electrode it was very difficult to establish which of these reactions were effectively related in the raise of the observed OCV in this system. However, taking into account that the oxygen reduction (see equation (4.4)) and the hydroquinone type surface group oxidation (see 4.5) could be involved, it was expected to observe a positive OCV since the protons provided by the hydroquinone oxidation (if the electrodes were short-circuited) could travel trough the electrolyte and the membrane to combine at the fuel cell-type electrode with oxygen from air and the electrons, transported by an external circuit, to form water. Obviously, in the OCV measurements does not flow any current but the potential differences between these two half cell reactions could explain at least the sign of the observed OCV. This system is similar to a Galvanic cell where in the positive electrode the reduction occurs and in the negative electrode the oxidation take place.

$$\text{quinone} + 2\,H^+ + 2\,e^- \rightleftharpoons \text{hydroquinone} \qquad E^\circ = +0.6992 \text{ V vs. NHE} \tag{4.5}$$

$$-COO^\bullet + H^+ + e^- \rightleftharpoons -COOH \tag{4.6}$$

$$>C{-}O^- \rightleftharpoons >C{=}O + e^- \tag{4.7}$$

It is interesting to estimate the magnitude of the OCV if a simple Galvanic cell with these reactions were considered. For this we can assume the IUPAC notation

of the Galvanic cells where the oxidation part is written on the left of the diagram and the reduction on the right as in (4.8) and we have to neglect the liquid junction potentials and the potential difference between the current collectors and the electrodes. The electromotive force ξ which is in this case also the OCV is defined by (4.9) where ϕ_R is the standard potential of the oxygen reduction and ϕ_L the standard potential of the quinone reduction. In this way an OCV which amounts to 0.529 V is calculated. This OCV value is in the range of the OCV observed.

$$\mathrm{C_{(hydroquinone)}} \mid \mathrm{H_2SO_4} \mid \mathrm{Nafion^{\circledR}112} \mid \mathrm{O_2} \mid \mathrm{Pt} \tag{4.8}$$

$$\xi = \phi_R - \phi_L \tag{4.9}$$

As soon as a hydrogen pressure was applied to the cell (after the evacuation of the air) the sign of the OCV changed to negative values. In this case the equilibrium involved at the fuel cell-type electrode side was the oxidation of hydrogen (see (4.10)). The reactions of the electroactive surface groups in the supercapacitor-type electrode to be considered are the same shown before. Assuming the same arguments as in the previous discussion, a negative OCV was expected when the fuel cell-type electrode would act as an anode and the supercapacitor-type electrode as a cathode. Therefore, the reduction of the electroactive surface groups was expected to take place in the supercapacitor-type electrode. In effect, an anodic charging current was observed when these two electrodes were connected through a load resistance. After the charging process was finished (and still the hydrogen pressure applied) the OCV of the cell was zero.

$$\mathrm{H_2} \rightleftharpoons 2\,\mathrm{H^+} + 2\,\mathrm{e^-} \qquad E^\circ = +0.000 \text{ V vs. NHE} \tag{4.10}$$

When the H_2 was evacuated (after the charging process was finished) and as soon as the pressure control system was open to the atmosphere and air was in contact with the fuel cell-type electrode the sign of the OCV changed again to positive values. No change of the OCV was observed neither during the hydrogen nor during the oxygen (air) evacuation. This situation was much the same as that observed at the beginning of the experiment (before any hydrogen pressure was applied), with the difference that the double layer was charged and a higher number of protons was present on the solution side of the supercapacitor-type electrode and that the electroactive surface groups were also reduced. This indicates that the fuel cell-type electrode acted as a cathode and the supercapacitor electrode as an anode during the discharging process.

The quasi-reversible redox reactions in which the electroactive surface groups mentioned above participate are the origin of the pseudocapacitance found in carbon

materials used in supercapacitors [13]. This pseudocapacitive behavior is observed when fast, potential-dependent reactions occur only at the surface of the carbon material, resulting in a Faradaic charge transfer across the double layer. Such reactions are favorable only in a certain range of potential, producing capacitive charging-discharging characteristics [13, 30]. It is reported in the literature that for this type of carbon materials the contribution of the pseudocapacitance to the total capacitance depends on the concentration of the surface active groups in the carbon and normally lies in the range of 5-10% [13].

The sign of the charging current (+) and the decrease of the H_2 pressure in the pressure control system confirm that the H_2 was electrochemically oxidized at the catalyst electrode, following (4.10).

During the discharging process, the sign of the current (−) indicates that a reduction at the catalyst electrode took place. There, the protons could recombine to form H_2 gas (reverse of equation (4.10)) or react with O_2 from the air to produce water (see equation (4.4)).

An exponential current-response in function of time is characteristic for the charging of the double layer at the electrode surface under the influence of a potential step [13]. In our experiments, before charging or discharging the cell, the system was far from equilibrium. Therefore, an OCV was observed. This voltage acted as a sort of potential step, with the difference that it was neither externally applied nor constant during the experiment. The OCV, observed before the charging and discharging processes, is then the driving force which leads to the charging and discharging of the double layer and the pseudocapacitance at the carbon black electrode.

Considering the redox couple quinone/hydroquinone (Q/HQ) as one of the most important surface functionalities which leads to a pseudocapacitive behavior of the carbon the following Nernst equations for the OCV of the overall reactions (4.11) and (4.12) (where CHA means charging and DIS discharging) are considered:

$$\mathrm{H_2 + Q \rightleftharpoons HQ} \qquad E^{\circ}_{(CHA)} = +0.6992 \text{ V vs. NHE} \tag{4.11}$$

$$\mathrm{2HQ + O_2 \rightleftharpoons 2H_2O + 2Q} \qquad E^{\circ}_{(DIS)} = +0.5298 \text{ V vs. NHE} \tag{4.12}$$

Just before the charging process:

$$E_{CHA} = E^{\circ}_{CHA} - \frac{RT}{2F} \ln \frac{(\gamma_{\mathrm{HQ}}[\mathrm{HQ}]/[\mathrm{C}]^{\circ})}{(P(\mathrm{H_2})/P^{\circ})\ (\gamma_{\mathrm{Q}}[\mathrm{Q}]/[\mathrm{C}]^{\circ})} \tag{4.13}$$

Just before the discharging process:

$$E_{DIS} = E^{\circ}_{DIS} - \frac{RT}{4F} \ln \frac{(\gamma_{\mathrm{Q}}[\mathrm{Q}]/[\mathrm{C}]^{\circ})^2}{(P(\mathrm{O_2})/P^{\circ})\ (\gamma_{\mathrm{HQ}}[\mathrm{HQ}]/[\mathrm{C}]^{\circ})^2} \tag{4.14}$$

In these equations γ_{HQ} and γ_{Q} are the activity coefficients of hydroquinone and quinone, respectively, and $[C]^{\circ} = 1$ mol kg^{-1}. From the equations it is derived that the OCV for charging and discharging should be determined by the activity (proportional to the concentration) of Q, HQ and the partial pressures of H_2 and O_2. As we mentioned before, this example should illustrate the origin of the OCV as the driving force for the charging and discharging processes. Obviously, the [Q] and [HQ] are far from the standard values and also the hydrogen and oxygen partial pressures are not exactly 1 atm. Therefore, it is clear that the observed OCVs will not match 100% these theoretical values.

When the fuel cell-type and the supercapacitor-type electrodes are externally connected through a load resistor, the system tends spontaneously to the electrochemical equilibrium. The hydrogen is oxidized at the fuel cell-type electrode and the surface active groups at the supercapacitor-type electrode are reduced, simultaneously with the formation of the double layer. The double layer is formed with the protons and electrons produced at the anode. The two species are transported through different paths towards the carbon black electrode. The electrons travel through the external circuit, generating a current, and the protons are transported through the membrane. After 120 s, when the charging process is finished, the voltage between the two electrodes is near zero.

Once the H_2 is evacuated and air is in contact with the fuel cell-type electrode, an OCV developed as well. This is due to the potential difference between the oxidation reactions of the surface active groups at the supercapacitor-type electrode and the O_2 reduction reaction (4.4) in the fuel cell-type electrode. When the electrodes are connected, the surface active groups in the supercapacitor-type electrode are oxidized, the double layer is discharged and O_2 from the air is reduced in the fuel cell-type electrode. The protons and electrons that are stored in the double layer travel like in the charging process, but in the opposite direction, through different paths to the fuel cell-type electrode. There they combine with O_2 to form H_2O. The voltage between the two electrodes is also near zero at the end of the discharging process (after 120 s).

Bi-exponential fit of the charging-discharging curves

During the charging and discharging process the system exhibits a bi-exponential current-response in time (see Figure 4.3 and equation (4.15)).

$$I(t) = I_{0,1}\, e^{-t/\tau_1} + I_{0,2}\, e^{-t/\tau_2} \tag{4.15}$$

As a first approximation, a time constant on the order 30 s is calculated assuming

only the diffusion coefficient of protons in bulk water, $D = 9.3\times10^{-5}$ cm^2 s^{-1} [44], and the root-mean-square distance of the layer thickness (0.5–1 mm). This constant matches relatively well the longer one of the time constants determined for both, charging and discharging process. However, the double-exponential behavior of the charging and discharging as well as the different timescales preclude a simple process. Diffusion and also electromigration mechanisms should be considered in order to understand the transport mechanisms of the protons in this system and the bi-exponential response of the current in time. Also the effect of pore tortuosity and pore wall friction play an important role in such porous systems [45].

The charging of the double layer in a porous material is a complex process. The total capacitance of the double layer can be described as the contribution from the external and the internal surface. For BP, it is estimated that almost 90% of the specific capacitance is due to the participation of the internal surface (porous medium). This internal capacitance contributes only when a charging-discharging process with moderate to slow kinetics takes place [40].

A bi-exponential fit of these curves and its analysis could contribute to the formulation of a model of the charging-discharging mechanism. Following (4.15), it is possible to calculate the SIC of the first and second exponential term separately. A "fast" sub-process which exhibits the smaller time constant and a "slow" sub-process which has the higher time constant are considered.

Figure 4.7 shows the bi-exponential analysis of the second cycle of a charging-discharging curve using H_2O. For both processes, the fast sub-process is highly relevant during the first 12 s. After this, the contribution of the slower sub-process is dominant. However, during discharging the contribution of the slow sub-process (71%) to the SIC was higher than that during charging (30%). These results indicate that neither the fast nor the slow processes are totally reversible.

From the results of the bi-exponential analysis we deduce that at least two different sub-processes with different timescales take place in the supercapacitor-type electrode during charging and discharging the cell:

- A fast sub-process involving the charging and discharging of the external double layer and the pseudocapacitance which occurs only in a specific range of potential and whose reactions do not propagate into the bulk material [30].

- A slow sub-process associated with the charging and discharging of the internal double layer (porous system of the carbon black layer).

We therefore assume that during the fast sub-process the charging of the external double layer and the pseudocapacitance occur simultaneously and during the slow

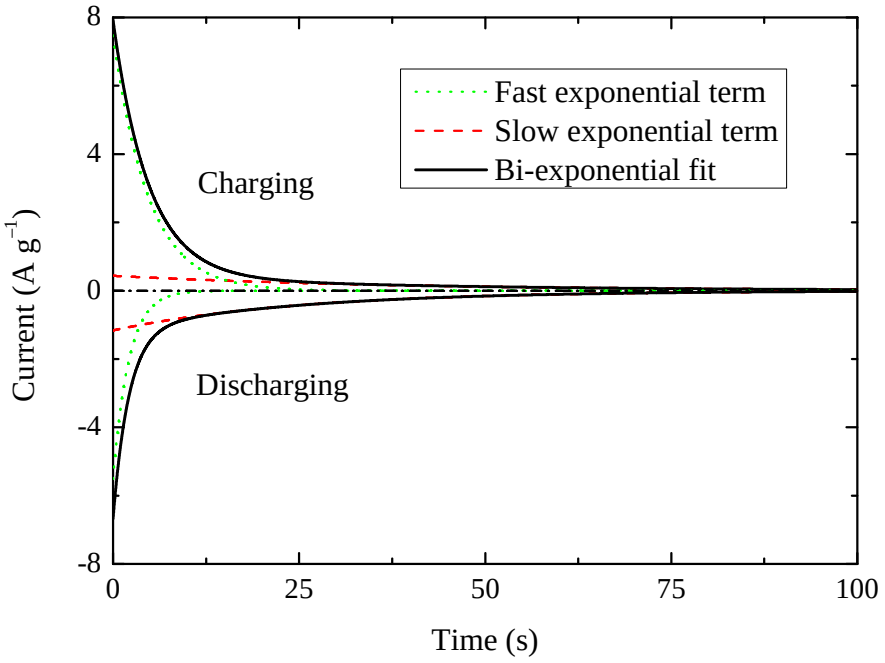

Figure 4.7: Bi-exponential analysis of the charging-discharging curves using BP and doubly-distilled deionized H_2O at 2.5 bar H_2 for charging and air at ambient pressure for discharging.

sub-process the internal double layer is charged. This agrees with the fact that the voltage at the beginning of the charging or discharging process is maximum (and equals the OCV) and also that it decays exponentially with time. In this way the pseudocapacitance is charged during the first seconds, when the voltage is high enough.

Considering that typical diffusion controlled processes in electrochemistry normally fit to a $t^{-1/2}$ function (known as the Cottrell equation), a fit of these curves to this behavior was also tested. However, as shown in Figure 4.8 the resulting fit was not satisfactory since the curves do not show a linear behavior along the $t^{-1/2}$ axis. These results also support our assumption that not only diffusion effects should be taken into account in order to describe the charging and discharging processes.

The asymmetry observed between the charging and discharging curves in Figure 4.3 and also the difference in the SIC indicate a certain loss of charge. The OCV in the loaded state against air was ca. 0.95 V, which is not only typical for hydrogen-air fuel cells but also close to the limiting hydrogen overpotential at a carbon-water interface. It decays linearly with a rate of 0.07 mV s^{-1}, which results in a loss of

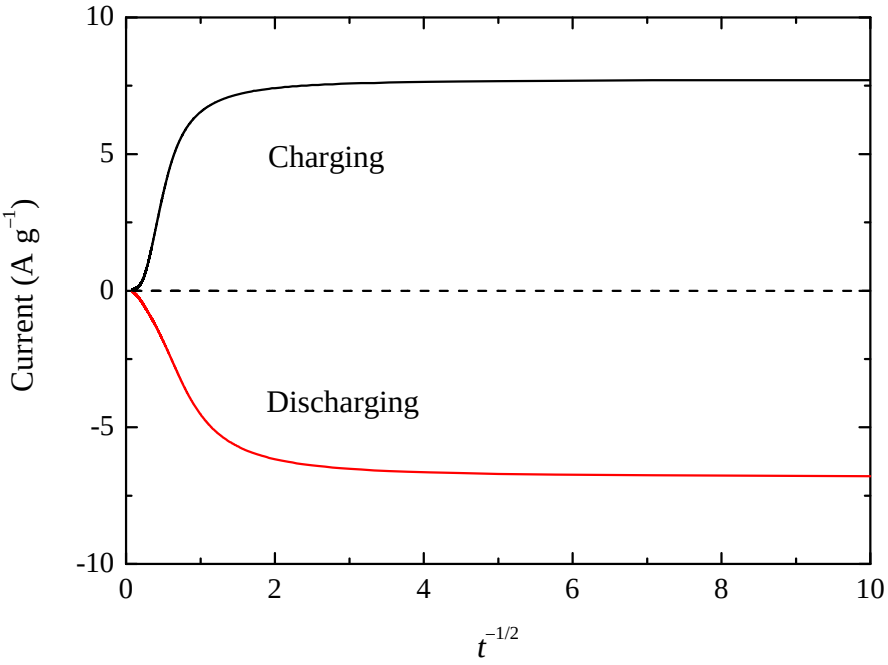

Figure 4.8: Charging and discharging current (corresponding to the second cycle using H_2O) vs. $t^{-1/2}$.

42 mV or 4.4% over the entire discharging time, while the deficit in the integrated charge amounts to about 20%. The origin of this loss can thus only to a minor extent be ascribed to bulk recombination of protons at the double layer or to leak currents. This asymmetry could be related to the transport of protons in the system. During the charging process the proton is a counterion that we want to store in the external surface and also within the structure of the porous electrode. In contrast, during the discharging process the proton acts as a coion that we want to expel from the electrode. In such a porous system the coion outflow is always less than counterion absorption [45]. Therefore, an inhibited proton transport is expected during the discharging process. It is also assumed that some of the reactions associated with the charging or discharging of pseudocapacitance have an irreversible behavior.

Dependence of the specific integrated charge with the amount of carbon black and with the hydrogen pressure

A dependence of the SIC with the amount of carbon black in the supercapacitor-type electrode is observed in Figure 4.5. Thicker layers were obtained by incrementing the amount of carbon black in the layer. Some fraction of the bulk carbon layer seems

to be inaccessible for the protons even at lower thicknesses. The effect becomes more noticeable by increasing the thickness of the layer. These results suggest that mainly the external surface of the carbon black layer was used in the formation of the double layer during the charging process. This also means that the diffusion of the protons through the tortuous structure of the carbon layer was hindered. Taking into account that the OCV after the charging process was similar for the different mass loadings used, a decrease in the SIC value means also a decrease in the capacitance of the electrode. These results agree with the observations made by Panic et al. in their study on capacitive properties of thin layers of BP [40] and its relation with the BP morphology. They found that the capacitance of a thin BP layer increases by going from the external surface into the bulk of the layer. Hu et al. have also observed that the specific capacitance of electrodes constructed of single-walled carbon nanotube paper in aqueous solution decreased when the mass loading and therefore the thickness of the electrodes was increased [46].

The SIC values calculated from the charging-discharging current-vs.-time curves of Figure 4.6 at different H_2 pressures are listed in Table 4.4. In this case, the original curves were integrated over 600 s in order to obtain a better appreciation of the capacity limit of the supercapacitor electrode. As the H_2 pressure was increased to 3.5 bar an increment of the SIC of ca. 20% was noted. The H_2 pressure had only little influence on the SIC. However, the effect of increasing the H_2 pressure in shifting the equilibrium (2.23) further to the right was confirmed. These results suggest that the device is already close to saturation at the H_2 pressure of 1.5 bar.

The saturation limit is determined by the number of electrons that can be stored in the carbon black. As mentioned in section 2.4, a theoretical hydrogen storage capacity of 8.33 wt.% relative to the storage material (only carbon black) can be achieved if it is assumed that all carbon atoms are exposed to the surface and that one positive or negative charge can be stored per surface carbon atom. However, the results shown in Table 4.4 indicate that the hydrogen storage capacity relative to the carbon material is below 0.1 wt.% and that only ca. 0.01 e^- per C atom is effectively stored. This value is far below what was initially envisaged (1 e^-per C atom). This low experimental saturation capacity can be attributed to the following effects:

- Electrostatic repulsion effects since it has been reported that only 10% of the surface atoms of carbon materials cold carry a free charge [26].

- Poor interparticle electrical contact, that leaves part of the material electrically inactive.

- Poor electrolyte accessibility to the intrapore surface area.

Table 4.4: H_2 storage capacity and SIC over 600 s of charging (CH) and discharging (DCH) processes at different H_2 pressures. "Losses" refers to the amount of SIC in % which is not recuperated by discharging.

H_2 pressure (bar)	SIC_{CH} (C g^{-1})	$\mid SIC_{DCH} \mid$ (C g^{-1})	H_2 $stored_{CH}$ (wt.%)	Losses[a] (%)
1.5	60.4	42.3	0.063	30
2.5	62.5	48.3	0.065	23
3.5	73.9	66.1	0.077	11

[a] this values differ from those shown in Table 4.3 due to the difference in the integration time used for calculate the SIC.

As mentioned before we believe that the hydrogen storage capacity of the cell is near to the saturation value at these conditions, far below this value the hydrogen storage capacity should increase linearly with the hydrogen pressure. In the following section we will study the influence of the pH on the charging and discharging behavior of the cell on the hydrogen storage capacity.

4.3 Effect of the electrolyte on the charging-discharging curves

4.3.1 Results

Higher OCVs than those observed using H_2O were observed using H_2SO_4 and NaOH as electrolytes. OCVs of ca. -0.8 V between the fuel cell-type electrode and the supercapacitor-type electrode before charging were obtained using 7 M H_2SO_4 and 7 M NaOH as electrolyte. As in previous experiments with H_2O, the WE terminal of the potentiostat was always connected to the fuel cell-type electrode and the CE and REF terminals to the supercapacitor-type electrode. After the charging process was finished, the H_2 was evacuated an the pressure control system open to the atmosphere. An OCV of about +0.95 V was observed before discharging. In the next cycles, the OCV before charging increased to values near to -0.90 V.

Also in these experiments, a decrease in the H_2 pressure during the charging process confirmed that the hydrogen is consumed at the catalyst electrode. The SIC of the charging curves matched in all cases the amount of consumed hydrogen.

The charging-discharging curves of the first cycle at acidic pH are shown in Fig-

ure 4.9. In this case, the asymmetry between the charging and discharging curves observed in all other experiments is reversed. The area under the curve of the charging process and its SIC are clearly smaller than those of the discharging process. This generates the negative value observed in the column "Losses" of Table 4.5. In this table are also shown the SIC values over 600 s for 5 cycles. After the first cycle, the SIC of the discharging process is less than that of the charging process.

Figure 4.10 shows the result of the second charging-discharging cycle, using H_2O and different electrolytes. The BP mass loading of the supercapacitor-type electrode was 3.8 mg cm^{-2}. These curves also exhibit approximately bi-exponential current-versus-time response. Higher time constants than those obtained using H_2O were observed using 7 M H_2SO_4 and 7 M NaOH as shown in Table 4.6 and 4.7. Also a charging-discharging asymmetry is noted for both electrolytes. The SIC values shown in Table 4.6 and 4.7 were calculated by integration of the curves obtained from the bi-exponential fit.

The results of the bi-exponential analysis of these curves are also listed in Table 4.6 and 4.7. During charging, the fast sub-process represents more than 55% of the SIC independent of the electrolyte used. In contrast, the slow sub-process contribution is more relevant in the discharging process for both H_2O and NaOH.

As shown in Table 4.5 the 7 M H_2SO_4 experiments exhibited the highest SIC. This amounts to ca. 162 C per gram carbon in the charging and 128 C per gram in the discharging process for the second cycle, corresponding to hydrogen storage capacities of 0.17 and 0.13 wt.% H_2, respectively.

In Figure 4.11 the charging current is plotted as a power density, developed in R, in function of time (for experimental setup see Figure 3.3). A similar behavior was observed when the discharging current was plotted as a function of time. The current density (A cm^{-2}) is the current in R divided by the geometrical area of the fuel cell-type electrode. The power density is calculated from the product of the voltage and current density trough R. A maximum of 23 mW cm^{-2} is observed at $t = 0$ for 7 M H_2SO_4. The charging and discharging of the cell offers a relatively high power density for a short time.

4.3.2 Discussion

Behavior of the open circuit voltage and the charging and discharging processes using different electrolytes

The differences observed between the OCV using water, 7 M H_2SO_4 and 7 M NaOH before the charging and discharging process are in part attributed to the change of

Table 4.5: H_2 storage capacity and SIC over 600 s of charging (CH) and discharging (DCH) processes for 5 cycles using 7M H_2SO_4. "Losses" refers to the amount of SIC in % which is not recuperated by discharging.

Cycle N°	SIC_{CH} (C g^{-1})	$\mid SIC_{DCH} \mid$ (C g^{-1})	H_2 $stored_{CH}$ (wt.%)	Losses (%)
1	78.1	136.9	0.08	(-57)
2	161.9	127.9	0.17	21
3	156.0	127.4	0.16	18
4	147.9	126.8	0.15	14
5	143.0	126.8	0.15	11

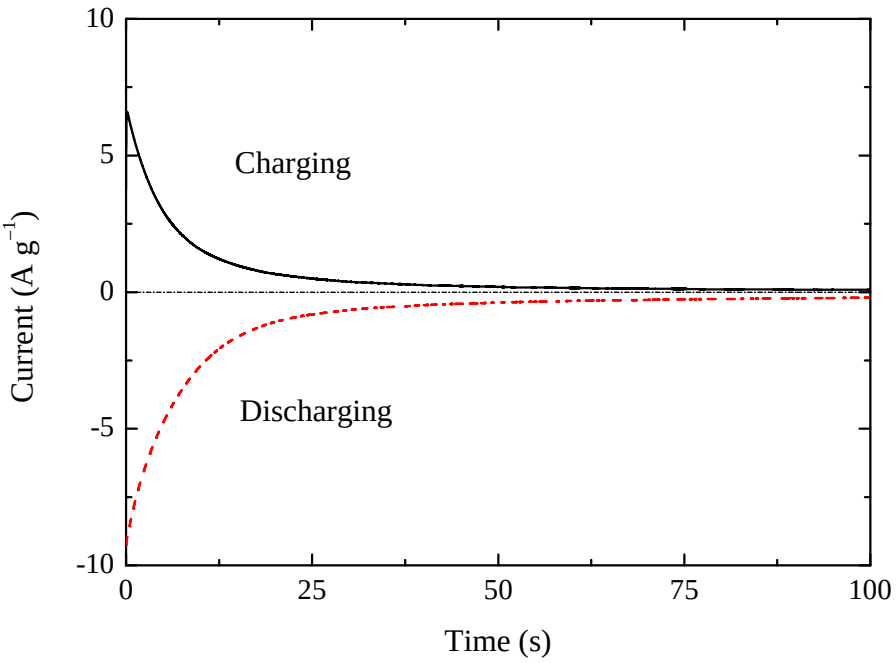

Figure 4.9: Spontaneous charging-discharging current-versus-time curves corresponding to the first cycle, using 7 M H_2SO_4 at 2.5 bar H_2.

the activity of the species in solution as a consequence of the change in concentration. The electrochemical equilibrium of the electroactive functional surface groups is also influenced by the pH value. The ketone and the quinonoid groups (4.7) are easily reduced in acidic pH, whereas the carboxylic (4.6) and phenolic (4.5) groups are easily oxidized in alkaline media. This causes a shift in the redox electrode potential

Table 4.6: Contribution on the SIC of the slow and fast processes with different electrolytes during charging of the two-electrode hybrid cell. Data obtained from the bi-exponential analysis. The SIC_{total} values were calculated from the integration over 120 s of the original curves.

Electrolyte	Sub-process	τ (s)	% of SIC (%)	SIC_{total} (C g^{-1})
H_2O	Fast	4.7	69	51.9
	Slow	38.5	31	
NaOH	Fast	5.5	55	93.5
	Slow	21.5	45	
H_2SO_4	Fast	7.6	78	120.3
	Slow	82.9	22	

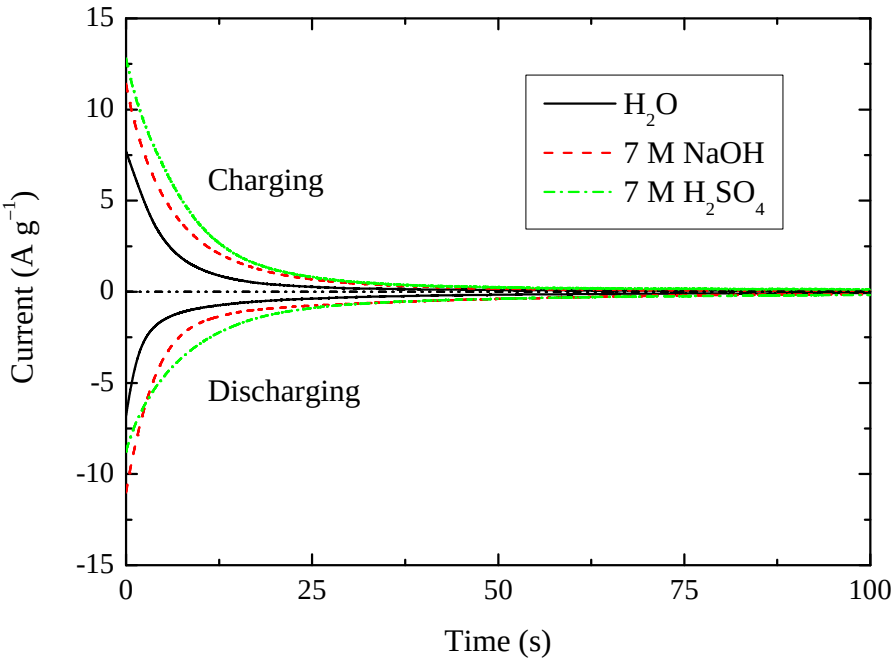

Figure 4.10: Spontaneous charging-discharging current-versus-time curves of the second cycle, using doubly-distilled deionized H_2O and different electrolytes at 2.5 bar H_2.

Table 4.7: Contribution on the SIC of the slow and fast processes with different electrolytes during discharging of the two-electrode hybrid cell. Data obtained from the bi-exponential analysis. The SIC_{total} values were calculated from the integration over 120 s of the original curves.

Electrolyte	Sub-process	τ (s)	% of SIC (%)	SIC_{total} (C g^{-1})
H_2O	Fast	5.5	29	42.5
	Slow	24.9	71	
NaOH	Fast	3.6	41	88.9
	Slow	40	59	
H_2SO_4	Fast	7.6	55	103.6
	Slow	56.8	45	

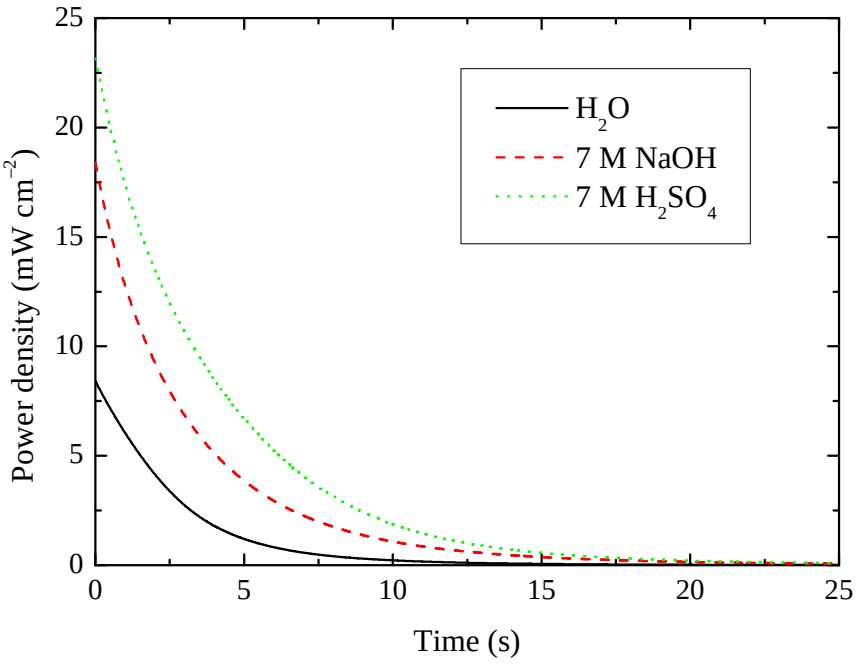

Figure 4.11: Power density developed in a 10 Ω resistor by the two-electrode hybrid cell during charging process for different electrolytes.

of these reactions, changing the OCV value.

As discussed in previous sections, an OCV between the fuel cell-type electrode and the supercapacitor-type electrode is developed just before the charging process

was performed. As soon as these electrodes were in contact through a resistor, a charging current flowed through the external circuit. The double layer and the pseudocapacitance in the supercapacitor-type electrode was charged until the chemical and electrostatic equilibrium was reached and the current was equal to zero.

Just before the discharging of the cell, when the H_2 was evacuated and the pressure control system open to atmosphere, a new condition, far from equilibrium, was established. The catalyst electrode was in contact with oxygen (from air). An OCV (with opposite sign as that of the charging process) is then developed between the two electrodes. The double layer and the pseudocapacitance were discharged when these electrodes were in contact through a resistor.

More remarkable differences between the charging-discharging behavior of the cell under acidic and alkaline conditions were expected. We presumed that the low concentration of protons in highly concentrated alkaline media would favor the proton transport towards the carbon black electrode, as a consequence of the high concentration gradient. Furthermore, in acidic media the proton concentration gradient should have inhibited the proton transport to the carbon black electrode. However, similar OCV and SIC values as well as similar charging-discharging behavior were observed for both electrolytes.

Although the pseudocapacitive contribution of the quinone/hydroquinone pair in alkaline solution would be very low due to the insufficiently available protons, it is reported that other redox reactions involving oxygenated functionalities which also contribute to the total capacitance are present [47]. These evidences support the idea that diffusion, electromigration and also the conservation of the electroneutrality (including the charge in the carbon surface) determine the charging-discharging behavior of this system. At high concentration of electrolyte some coupling between double-layer charging and simultaneous Faradaic processes, involving adsorption and partial charge transfer processes, has been suggested [13, 48]. Therefore, we assume that in concentrated NaOH also the Na^+ ions participate during the charging process in the formation of the double layer. These are attracted by the negative charges in the carbon. The protons produced in the catalyst electrode diffuse towards the carbon surface in order to maintain the electroneutrality in the system. As a result, when the cell is charged, protons and also Na^+ ions are adsorbed at the carbon black surface. During the discharging process the desorption of both species takes place. Although it is possible that even the Na^+ ions could be transported back through the Nafion® membrane [49], only the protons participate in the O_2 reduction in the catalyst electrode. The reduction of Na^+, which has a standard redox potential of -2.70 V vs. the normal hydrogen electrode, is not possible at the voltages observed

in these experiments.

On the other hand, the effect of the lower pH on the proton transport is clearly illustrated by the asymmetry observed in the first charging-discharging cycle in Figure 4.9. In this case, there was a high concentration of protons at the carbon black electrode surface at the beginning of the experiment. During the charging process the H_2 was oxidized at the anode and the double layer was formed on the carbon surface, at the same time the electroactive surface groups were reduced. However, it was expected that the basal plains with aromatic character (C_π) of BP may have functioned as Lewis base capable of complexing protons to its π structure [15], in which case the equilibrium (4.2) already mentioned in a previous section should be considered. This means that before the first charging cycle some of the available sites where the protons could be complexed and also attracted to form the double layer were already occupied by protons from the electrolyte. Therefore, only a small quantity of H_2 was oxidized in the first charging process. Just after the discharging process the active sites were free and protons were needed to form the double layer in the next recharging process.

Bi-exponential analysis

The bi-exponential analysis of the curves for 7 M H_2SO_4 and 7 M NaOH listed in Table 4.7 and 4.6 also suggest that different processes with different timescales take place during charging and discharging the cell. However, with only the results of the bi-exponential analysis it is difficult to conclude about the charging and discharging mechanisms, especially when other ions, such as SO_3^{2-} and Na^+ are present in solution. These ions could also be adsorbed at the carbon black surface. The use of impedance techniques could be very useful in elucidating the charging-discharging mechanism by the separation of the Faradaic and non-Faradaic components of the charging and discharging current.

In general, it is noted that the increase of the electrolyte concentration causes an increment in the current, SIC and time constants. This means, for the charging and discharging of the external double layer, an increment in the capacitance and a decrease in the internal resistance (increase of the RC product in a conventional dielectric capacitor). With higher time constants there is more time for the charging of the internal double layer. As described in the Gouy-Chapman-Stern model of the double layer, the excess of charge at the electrode surface needs to be counterbalanced with ions from the solution. It may then take some thickness of the solution to accumulate these ions in a so called diffuse layer (see Figure 2.5 (c) in section 2.2.1). The average distance between the electrode surface and this layer depends

on potential and also electrolyte concentration. Therefore, as the electrolyte concentration rises, there should be a compression of the diffuse layer and an increment in the capacitance [50]. The presence of hydroxyl groups and protons also increments the specific conductivity of the solution.

The highest hydrogen storage capacities observed using 7 M H_2SO_4 (0.17 wt.% for charging and 0.13 wt.% for discharging) are much below the ultimate maximum of 8.33 wt.% (if quoted against the weight of carbon, which is common in the supercapacitor community, or 3.33 wt.% if quoted against the weight of carbon plus water), but remarkably, they are one order of magnitude more than what can be reached by physisorption on carbon or molecular organic framework materials at the same temperature and pressure [36].

As discussed in earlier sections, the main capacity limitation in such a system may be electrostatic repulsion between the surface charges. The assumption of a full charge per surface carbon atom is too optimistic, as other work suggests that only 10% of the surface atoms can carry an excess of charge [26]. Furthermore, not each carbon atom may be accessible at least from one side, although the BET surface area of 1155 $m^2\ g^{-1}$ is close to the value expected for one side of a graphene sheet, 1315 $m^2\ g^{-1}$ [3, 26]. It is also possible that the surface was not completely wetted by the electrolyte or that not all carbon atoms were electrically connected to the electrode. A limitation of this system in comparison with a conventional supercapacitor is the fact that in the fuel cell-type electrode as well as in the supercapacitor-type electrode Faradaic reactions which induce chemical changes in the electrode take place, compromising the life span of the system. Another factor to take into account is the water management in the system. Water is transported through the membrane with the protons during the charging and discharging process as a consequence of the electroosmotic drag. The aqueous electrolyte had also the function to keep the membrane hydrated during the charging-discharging cycles. However, it was observed that after a certain number of cycles (> 10) the amount of water or electrolyte aqueous solution in the system decreased. This factor also affects the life span of the system, without enough water the proton conductivity of the membrane decreases and therefore the operation of the cell is inhibited. A possibility to avoid this problem is to increase the humidity of the H_2 after certain numbers of cycles in order to maintain a specific amount of water inside the cell.

Clearly, the formation of the electrical double layer plays a crucial role in this system. Other works on electrochemical hydrogen storage in carbon substrates have demonstrated the relevance of charging an electrical double layer as a step preceding the formation of hydrogen in its oxidation state zero by electrochemical reduction

of water in alkaline solution or protons in acidic medium [51, 52]. The hydrogen produced is stored in the carbon material and later oxidized in situ during the discharging process. No hydrogen gas enters the storage material on charging, and no hydrogen leaves it on discharging. Electrical work is spent on charging, much as in a rechargeable battery. In contrast, the present concept does involve hydrogen as a fuel from an external source, but no external electrical work is applied, neither by charging nor discharging the cell. Owing to the electrode overpotential the recombination of protons at the carbon surface is not expected to take place at the measured open circuit voltage (< 1 V) [35].

Some efforts are devoted to the hybridization of high energy density storage devices with fuel cells. A power density increment of 11 mW cm^{-2} by hybridization of a direct methanol fuel cell with a supercapacitor, which was charged by a constant current, was observed by Park et al. [53]. With the inclusion of our concept inside a PEM fuel cell or a methanol fuel cell, the resulting three-electrode hybrid system can provide a theoretical power increment of 20-25 mW cm^{-2} for a few seconds, as observed in Figure 4.11. To explore this idea, a new cell was designed and investigated. The results are presented and analyzed in the subsequent chapters.

4.4 Estimation of the electrical capacitance

4.4.1 Results

The electrical capacitance of the cell (supercapacitor-type electrode in this two-electrode hybrid configuration) and its dependence on the electrolyte and pH was estimated through galvanostatic and cyclic voltammetry experiments. As mentioned before in section 2.2.3, these two methods are commonly used for the estimation of the specific capacitance also in asymmetric capacitors in a two-electrode configuration [47, 54, 55, 56]. In a galvanostatic experiment, at an applied constant current density, the potential difference developed across the double layer changes linearly with time, as the charge builds up across the interface if the capacitance is constant with the potential (see equation (2.16)). In this case the capacitance can be estimated from the slope of the linear segment of a cell voltage vs. time curve (see Figure 2.12). Figure 4.12 shows the galvanostatic charging curves obtained at an applied constant current of 4 A g^{-1} for different electrolytes. As it was also observed in the spontaneous charging experiments, the H_2 pressure decreased during the galvanostatic charging experiments. The SIC in this case also matched the amount of hydrogen consumed (see Table 4.8). The BP mass loading was 3.8 mg cm^{-2}.

Table 4.8: Capacitance, SIC and hydrogen storage capacity derived from the galvanostatic charging experiments (i = constant = 4 A g^{-1}) using different electrolytes. The integration time (t_{INT}) corresponds to the period where the curves behave linearly.

Electrolyte	t_{INT} (s)	SIC_{CHA} (C g^{-1})	H_2 stored (wt.%)	Capacitance (μF cm^{-2})
H_2O	80	72	0.075	7
7M NaOH	270	240	0.250	12
7M H_2SO_4	270	240	0.250	12

Within the first 20-30 s the curves exhibit good linearity. After that some deviations from the linearity are observed. After about 180 s for H_2O and 250 s for NaOH and H_2SO_4 the cell voltage remains relatively constant at values of about 0.20-0.25 V. The capacitances calculated through this method are listed in Table 4.8. Taking into account that charge is current multiplied by time, the slope of the curves in Fig-

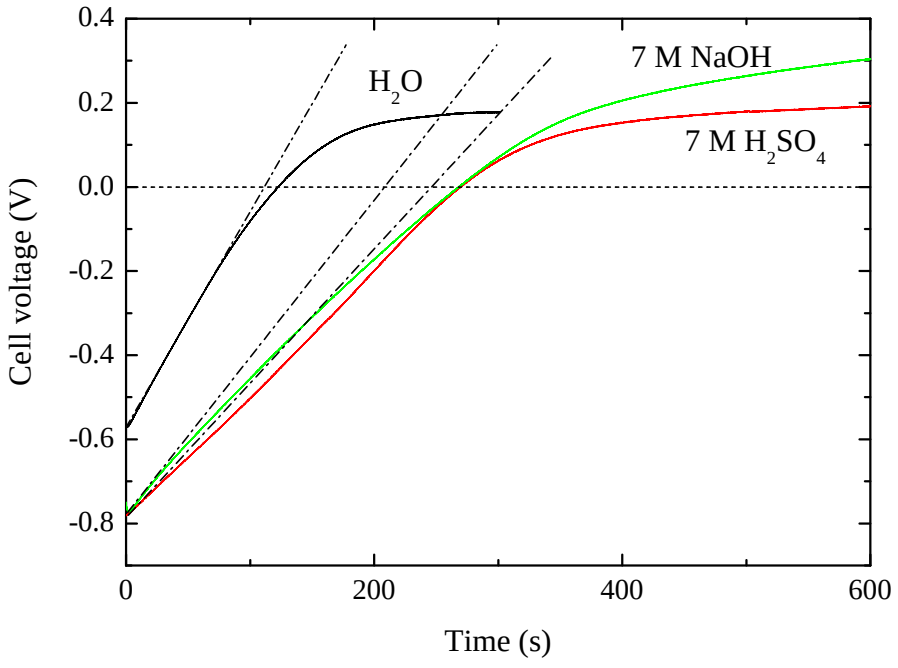

Figure 4.12: Cell voltage during galvanostatic charging process (at a constant current) with different electrolytes.

ure 4.12 at a constant current determines the value of the capacitance (see equation (2.16) and Figure 2.12 in section 2.2.3). A slope near to one means that the electrode is not able to store much charge in the double layer in comparison with an electrode exhibiting lower slope values. Obviously, this observations are valid as long as the curves behave linearly and when no Faradaic process, for example, solvent decomposition take place.

In potential sweep-reversal experiments (cyclic voltammetry) at a constant sweep rate, the current response profile of a capacitive element with constant capacitance is ideally a rectangle parallel to the potential axis [13] (see Figure 2.14). Using equation (2.18) the capacitance can be estimated from the charging or discharging current and the sweep rate. Cyclic voltammetry experiments were performed at a sweep rate of 0.02 V s^{-1} for different electrolytes at a H_2 pressure of 2.5 bar. The results are shown in Figure 4.13. During these experiments no variation of the hydrogen pressure was observed. The SIC values over about 24 s corresponding to the charging part of the voltage sweep for each electrolyte are shown in Table 4.9. This charge corresponds to an amount of hydrogen consumed (ca. 1.3 μmol H_2) which leads to a variation of less than 1 mbar in the hydrogen pressure inside the pressure control system. Therefore, no variation in the H_2 pressure could be registered in these experiments.

The voltage window (from -0.5 V to 0 V) as well as the starting voltage (-0.5 V) were selected in a way that the electrochemical response was similar to the ideal electrochemical response of a pure capacitive element so that the capacitance could be easily calculated. In other experiments performed over a wider voltage window (beyond more negative values than -0.5 V and more positive values that 0 V) deviations of the ideally response were found which may have led to the calculation of wrong capacitance values.

The current response has an approximately rectangular form. Some delay of potential during potential sweep and also increasing currents at the end of the cycles are observed. The capacitance values calculated from these experiments are listed in Table (4.9).

4.4.2 Discussion

The assumption that in the linear segment of the curves the supercapacitor-type electrode (carbon black) behaves like an ideally polarizable electrode should be carefully discussed. In an ideally polarizable electrode only non-Faradaic processes take place, thus the potential behaves linearly in time with the charge accumulating in the double layer (see also section 2.2.1). In our system, the oxidation of H_2 during the charging process represents a Faradaic process which can only be coupled with

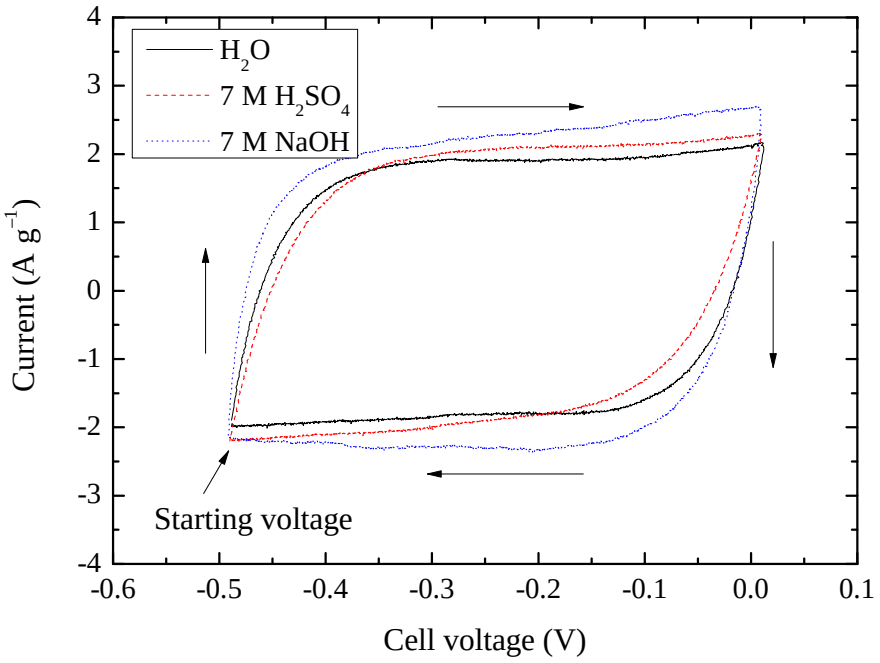

Figure 4.13: Cyclic voltammograms of the cell for different electrolytes corresponding to the third sweep cycle.

Table 4.9: Charging current (i_{CHA}), SIC and capacitance values derived from the cyclic voltammetry experiments using different electrolytes at a sweep rate of 0.02 V s^{-1}.

Electrolyte	i_{CHA} (A g^{-1})	SIC_{CHA} (C g^{-1})	H_2 stored (wt.%)	Capacitance (μF cm^{-2})
H_2O	1.8	40.8	0.042	8
7M NaOH	2.4	50.2	0.052	11
7M H_2SO_4	2.2	42.9	0.045	10

a reduction process in the supercapacitor-type electrode. Then, reduction of some surface functional groups should take place at this electrode. However, we assume that during the first seconds of the experiment the external double layer should be charged simultaneously with the pseudocapacitance.

The curves of Figure 4.12 exhibit relative good linearity over a time of ca. 80 s for H_2O and 270 s for NaOH and H_2SO_4. However, taking into account the evidence of H_2 oxidation, the calculation of the capacitance over such long periods has some

uncertainty. Therefore, these calculations were done over the first 5 s. The deviations from linearity are attributed to the presence of reactive surface functional groups such as those discussed in section 2.2.2.

The observed values of specific capacitance are comparable with the typical reported values for the double layer capacitances of carbon blacks in aqueous electrolytes. These are in the range of 7-20 μF cm^{-2} [15, 26]. However, for BP compressed pellets in 12 M H_2SO_4 a mass specific capacitance of 240 F g^{-1} which corresponds to a double layer capacitance of 16 μF cm^{-2} was found [26]. Even higher values of 310 F g^{-1} using thin-layer BP electrodes (0.09 mg BP cm^{-2}) in 0.5 M H_2SO_4 and cyclic voltammetry techniques using a three electrode configuration were reported [40]. In contrast, our experiments were performed with thicker electrodes in a two-electrode system (3.8 mg BP cm^{-2}) and without the application of any mechanical pressure. As discussed in section 2.2.3, the capacitances calculated using the cyclic voltammentry techniques with a three-electrode configuration normally lead to a doubling of the calculate capacitance in comparison with the capacitances calculated in a two-electrode system [29]. Therefore, these results should be carefully compared.

The low capacitance values obtained suggest that in our electrodes not all BP particles were electrically connected or even in contact with electrolyte. Furthermore, it is reported that in high-surface-area carbon materials which contain micropores only a part of the total internal area of the internal structure is wetted by electrolyte which could lead to lower values of the double layer capacitances [15]. This argument also supports the discussion about the results of Figure 4.5, where the mass specific SIC decreased with increasing BP mass loading and therefore the thickness of the electrode layer.

In a cyclic voltammogram the ideal current response of a capacitive element is a rectangle along the voltage-time axis. The sign of the current is immediately reversed when the potential sweep is reversed. In such cases, the current is independent on potential and the process is purely electrostatic (non-Faradaic). In contrast, the current response observed in Figure 4.13 represents a typical response of a capacitor made of porous carbon black electrodes with pseudocapacitive properties [28, 51] where the charge accumulated in the capacitor depends on the electrode potential. The delay in potential observed just after the potential sweep is attributed to a kinetically slow process involved during charging the pseudocapacitance [28]. Also the increase of the current near the potential limits is related to pseudocapacitive properties of the electrode. However, strong signals such as oxidation or reduction peaks were absent in this voltage window.

Although no evidence of diminution of the H_2 pressure was observed, we believe that indeed H_2 was oxidized during the anodic sweep and protons were reduced during the cathodic sweep (producing H_2 gas) at the catalyst electrode. In fact, the amount of hydrogen consumed during the anodic (charging) sweep for each electrolyte (proportional to the SIC values shown in Table 4.9) could only have caused a variation of less than 1 mbar in the pressure control system. Therefore, we assume that the change in the H_2 pressure during the experiment could not be detected with the manometer used which has a detection limit of $\pm$ 1 mbar.

The difference found in capacitance values using different electrolytes, observed also in the results of the galvanostatic experiments, is attributed to the change in the structure of the double layer and the influence of pH on the pseudocapacitance. As discussed previously, at high concentrations of electrolytes a more compact double layer is formed, as a consequence of the contraction of the diffuse layer. Also the redox potential of the oxygen-based surface group reactions in the carbon black surface is influenced by the pH of the electrolyte.

Pell et al. [33] have proposed that the capacitance of the non-Faradaic electrode in a battery-capacitor asymmetric capacitor could be estimated following equation (4.16). The operational voltage (in our case the OCV) of the electrode determines its charge-density (q) and the capacitance (C) is expressed in F g $^{-1}$. Maximal capacitances of 15 μF cm^{-2} for charging and 12 μF cm^{-2} for discharging the carbon black electrode using 7 M H_2SO_4 are then obtained (using the SIC values from the integration over 600 s).

$$q(\text{C g}^{-1}) = C\Delta V \tag{4.16}$$

Taking into account the maximal capacitance for the charging process and following equation (2.5) the electrical energy stored in the supercapacitor-type electrode of our two-electrode asymmetrical capacitor at the OCV of 0.95 V amounts to 77 J g^{-1}. The combustion energy of the hydrogen (assuming the hydrogen's lower heating value of 241 kJ mol^{-1}) that is stored on the same electrode (1.67 mmol H_2) is 201 J g^{-1}. This means that the chemical energy stored on this device is a factor of 2.6 larger than that of a symmetrical supercapacitor of comparable high quality. Furthermore, with this asymmetrical hybrid configuration the full charge capacity of the double-layer and pseudocapacitive components of the carbon black electrode are utilizable for the Faradaic process in the fuel cell-type electrode [33].

4.5 Summary

The potentials and limitations of the two-electrode hybrid cell as an energy storage method based in hydrogen were evaluated. Two carbon blacks (BP and PX) with different surface properties were tested as supercapacitor-type electrode material. Carbon black BP exhibited the higher surface area, micropore volume and SIC and was therefore chosen as supercapacitor-type electrode material for the cell characterization.

Reversible charging and discharging of this cell was performed using H_2O and different electrolytes. The experiments using H_2O have shown that during the charging process, H_2 was oxidized at the fuel cell-type electrode and oxygen-based surface electroactive groups (pseudocapacitance) were reduced at the supercapacitor-type electrode, simultaneously with the charging of the double layer. The double layer was formed in this electrode with protons in the aqueous solution and electrons in the carbon black layer. During the discharging process the protons were transported back through the membrane towards the fuel cell-type electrode. There, oxygen, protons and electrons combined to form water. Simultaneously, the surface electroactive groups in the carbon black surface were oxidized. The spontaneous charging and discharging of the cell produced a flow of electrons through the external circuit, generating power in an external resistor.

Asymmetric charging-discharging current-versus-time curves which also exhibited a bi-exponential behavior were observed. The results of the bi-exponential analysis suggest that at least two sub-processes which are not totally reversible and have different timescales, took place during charging and discharging the cell: a fast subprocess associated with the charging of the external double layer as well as the charging of the pseudocapacitance and, a slow one, associated with the charging of the internal double layer.

By increasing the H_2 pressure from 1.5 to 3.5 bar only an increase of 20% in the SIC was obtained in the experiments using H_2O. However, its effect on shifting the equilibrium (2.23) further to the right was confirmed. It is also assumed that the hydrogen storage capacity of the cell in these experiments was near to saturation at the H_2 pressure of 1.5 bar storing a maximum of 0.077 wt.% of H_2 which corresponds to ca. 0.01 e^- per C atom stored.

The effect of using different electrolytes on the SIC was also evaluated. The highest SIC was found using 7 M H_2SO_4, it amounts to 162 C g^{-1} BP during charging and 128 C g^{-1} BP during discharging the cell, which is almost a factor 3 more than the SIC obtained using only water. This corresponds to a hydrogen storage capacity of 0.17 wt.% and 0.13 wt.% during charging and discharging, respectively, which is

one order of magnitude more than what can be reached by physisorption on carbon or molecular organic framework materials at the same temperature and pressure. No clear tendency was observed in the results of the bi-exponential analysis of the current-versus-time curves using H_2SO_4 and NaOH. These results are difficult to interpret without additional information.

The main capacity limitations in this system are related to the electrostatic repulsion between the surface charges, the limited amount of surface atoms which can carry a full charge and its accessibility by the ions in solution. Also not all carbon atoms were wetted by the electrolyte or even electrically connected to the current collector.

In contrast with a conventional supercapacitor, Faradaic reactions which take place in the fuel cell-type electrode as well as in the supercapacitor-type electrode may compromise the life span of the system. Also the water management is a critical factor to consider in the two-electrode hybrid cell operation. In order to conduct protons the membrane has to be well hydrated. With an increasing number of cycles the amount of water in the system decreases, limiting the cycle lifetime of the cell. This problem can be avoided by the use of pre-humidified hydrogen. The gas humidification can be regulated by a control system, increasing the relative humidity of the gas, for example, after certain number of cycles when the total amount of water in the system has decreased, say, to 50%. In this way the amount of water in the system would be controlled. Obviously, a detailed study of the water management of the system would be needed.

When the current response of the charging and discharging processes is plotted as power density in function of time, it is observed that a high power density of about 20 mW cm^{-2} is obtained during the first few seconds. This suggests the possibility to use this device as an extra power complement for a primary power source such as a PEM fuel cell. This extra power source could be discharged in case of peak power demand. A hybrid system, where the supercapacitor-type electrode is put inside a PEM fuel cell in a three-electrode single module, following this idea, is described and characterized in the following chapter.

The capacitances obtained from the galvanostatic experiments were 7 μF cm^{-2} for H_2O and 12 μF cm^{-2} for 7 M NaOH and H_2SO_4. Similar values were found using cyclic voltammetry methods. These specific capacitances are comparable with the typical reported values for the double layer capacitance of carbon blacks in aqueous electrolytes. In general, the difference found in capacitance values using different electrolytes is attributed to the change in the structure of the double layer and the influence of the pH on the redox potential of some of the pseudocapacitive reactions.

At high concentrations of electrolytes a more compact double layer is formed and therefore the capacitance of the electrodes for concentrated NaOH and H_2SO_4 is higher than for plain water.

It was found that the combustion energy of the hydrogen stored in our two-electrode hybrid cell at the highest hydrogen storage capacity observed (0.13 wt.%) is a factor 2.6 higher than the electrical energy stored on a symmetric supercapacitor of comparable high quality.

5 Experiments with the three-electrode fuel cell-supercapacitor hybrid cell

5.1 Operation as a fuel cell

5.1.1 Results

The aim of this study was to determine the electrolyte and its concentration at which the three-electrode hybrid cell, operated as as fuel cell, exhibits the highest performance. In these experiments we placed the graphite electrode without electrical connection between two one-side catalyst-coated Nafion® membranes.

Based on the results of previous experiments with the two-electrode hybrid cell, we first studied the performance of the fuel cell using H_2O, H_2SO_4 and NaOH. The cell exhibited the best performance with H_2SO_4. After the electrolyte had been selected, we performed polarization curve measurements at different concentrations of H_2SO_4 (between 0.1 and 15 M). The results are shown in Figure 5.1. The shape of these curves is similar to the typical polarization curves for PEM fuel cells [8]. However, here we have straight lines even in the region of maximal current density where the concentration polarization losses should be significant.

Higher current densities were observed by increasing the H_2SO_4 concentration and therefore the specific conductivity of the electrolyte. However, at current densities of ca. 60-70 mA cm^{-2} the 10 M curve cuts the 5 and 7 M curves. Also a decrease in the cell voltage and current density of the 15 M curve is observed. This curve exhibited even lower current and potential than the 5, 7 and 10 M curves which is caused by the decrease of the proton conductivity of the electrolyte solution at very high H_2SO_4 concentrations.

Figure 5.2 shows the power density curves resulting from the polarization curves of Figure 5.1. The maximum power density is observed at the concentration of 10 M. This value amounts to 21.6 mW cm^{-2}, which is very low in comparison with reported

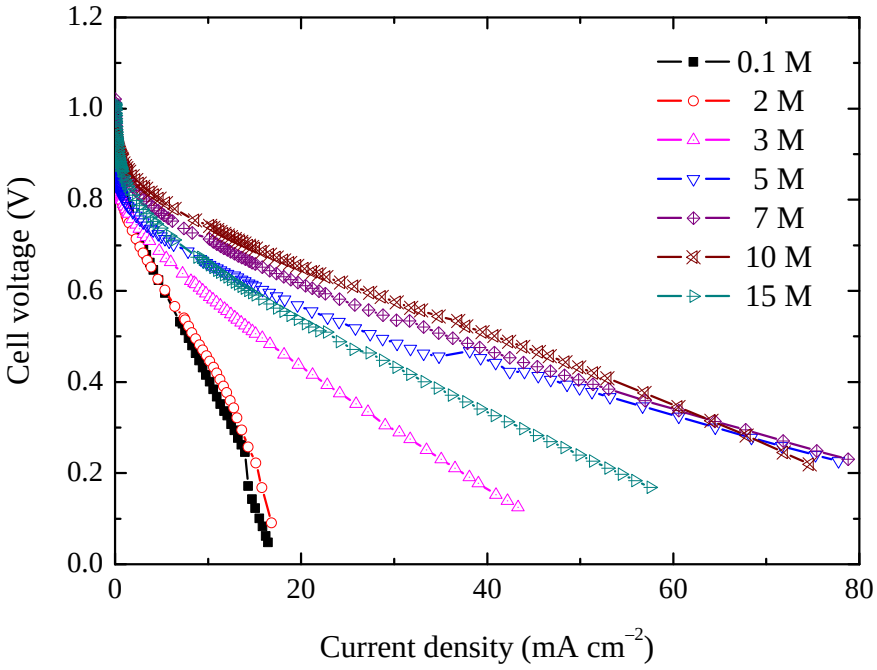

Figure 5.1: Polarization curves of the tree-electrode hybrid cell operated as a fuel cell at different concentration of H_2SO_4.

values for PEM fuel cells (in excess of 1 W cm^{-2}) [8].

5.1.2 Discussion

The curves shown in Figure 5.1 are similar to the typical PEM fuel cell polarization curves. In the region of very low current densities the activation polarization losses become predominant which is a consequence of sluggish electrode kinetics. It means that an overpotential (polarization) in both electrodes is needed in order to produce current. Also internal currents and hydrogen crossover contribute to this effect which is more remarkable in this region [8]. Therefore, the observed open circuit voltages were below the equilibrium potential of 1.23 V. The concentration polarization was absent in the region of higher current densities as a consequence of operation with pure oxygen at the cathode.

The differences in the slope of the polarization curves (linear part) correspond to changes in the ohmic losses of the cell. The ohmic losses occur because of resistance to the flow of electrons through the cell components and the external circuit and also to the flow of the ions in the electrolyte. These losses have three main components, namely, electronic, ionic and contact resistance. With the variation in the electrolyte concentration we expected to influence only the ionic resistance, since the other

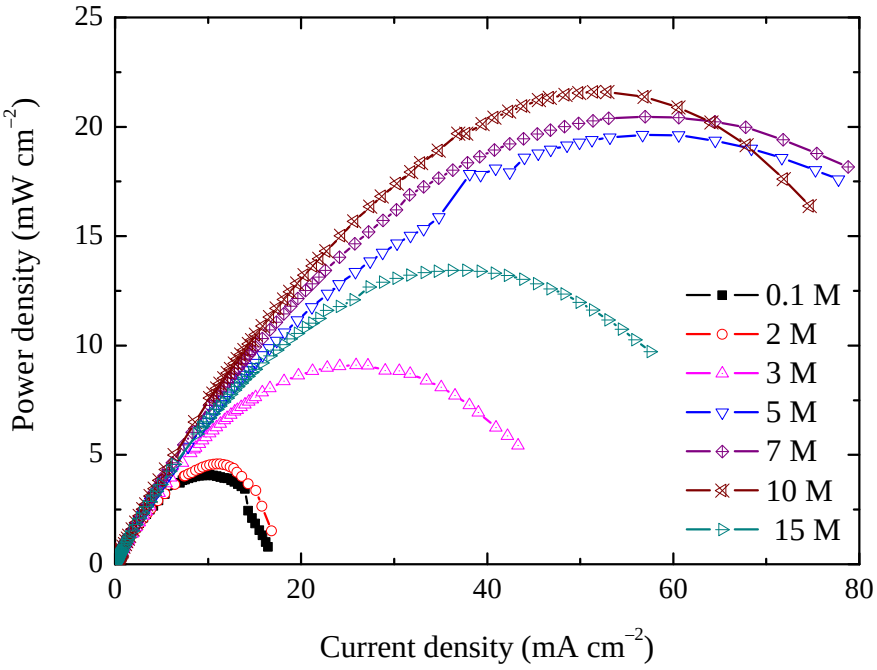

Figure 5.2: Power density curves of the tree-electrode hybrid cell operated as a fuel cell at different concentration of H_2SO_4.

elements in the cell remained unaltered.

Considering the linear part of the equation (2.4) and following Ohm's law we obtain an expression from which the total resistance of the fuel cell can be calculated ((5.1)). The term E' does not has any physical meaning. The results of the linear regression are shown in Table (5.1).

$$E_{cell}(i) = E' - iR_i \tag{5.1}$$

Although it has been shown that 4 M H_2SO_4 aqueous solutions at 25°C exhibit the highest conductivity [57], a decrease in the slope (in absolute value) of the polarization curves with the increment in the H_2SO_4 concentration beyond 4 M to 10 M is observed (see Table (5.1)). However, the 15 M curve shows a higher slope than the 5, 7 and 10 M curves. At this low degree of hydration, we expected that the proton conductivity through the prototropic mechanism was inhibited, due to the poor dissociation of the acid [58, 59]. Other studies in the conductivity of H_2SO_4 aqueous solutions suggest that a change of the proton conducting mechanism takes place at high concentrations, resulting in higher proton mobility as a consequence of the shortening of the H bonds, the rise in the density and decrease of the viscosity [60, 61].

Table 5.1: Total resistance (R_T) and maximal power density (P_{max}) of the three-electrode hybrid cell operated as a fuel cell at different H_2SO_4 concentrations. The slope values were multiplied by the electrode geometrical area (1.33 cm^2) in order to obtain the resistance values.

$[H_2SO_4]$ (M)	Slope (Ω cm^{-2})	R_T (Ω)	P_{max} (mW cm^{-2})
0.1	−40.8	30.7	4.1
2	−33.6	25.3	4.6
3	−14.6	10.9	9.1
5	−8.7	6.5	19.6
7	−7.8	5.9	20.5
10	−7.6	5.7	21.6
15	−10.9	8.2	13.4

The behavior of the 10 M curve at current densities higher than 60 mA cm^{-2} is related to gradual dilution of the electrolyte caused by water diffusion from the cathode. This could lead to a change in the proton conductivity and therefore in the performance of the cell.

The maximum power density of cell (about 22 mW cm^{-2}) was observed using 10 M H_2SO_4 solutions (see Table 5.1). This value is very low in comparison with the typical reported PEM fuel cell performance (1 W cm^{-2}). In a conventional PEM fuel cell, the distance that the protons diffuse from anode to cathode is on the order of the membrane thickness. In the case of Nafion® 112, this value is about 50 μm. In our cell, with the inclusion of the 2 mm thick graphite disk and the use of an additional Nafion® membrane, this distance was increased by a factor of 40. Therefore, lower performances were expected.

Considering the former argument, the fuel cell would exhibit a power on the order of 0.8 W cm^{-2} if it was operated with only one Nafion® 112 membrane catalyst-coated on both sides and without the graphite electrode. This would agree with the PEM fuel cell performances described above.

The graphite disk acted as a current collector for the supercapacitor-type electrode material (carbon black). It had to be able to permit the transport of the protons trough itself from the anode to the cathode. For this purpose, it had some holes which were filled with electrolyte (see Figure 3.6 in section 3.4.1). However, the area without orifices had to be large enough to form the carbon black layer on it. In

fact, the open ratio was 7.5%. Then, when the protons leave the membrane they can only diffuse further through the electrolyte which is in the orifices of the graphite electrode. Also for this reason, lower cell performances were expected.

After selecting the best electrolyte concentration, further experiments with the inclusion of the carbon black in the current collector were performed. The results are presented and discussed in the following sections.

5.2 Operation as a supercapacitor

5.2.1 Results

In this section we present the results of the charging-discharging experiments of the three-electrode hybrid cell operated as a supercapacitor. The fuel cell-type anode and cathode were electrically disconnected from each other. Under constant hydrogen flow (0.375 l h^{-1}) a voltage of about -0.8 V was measured between the supercapacitor-type electrode (S) and the fuel cell-type anode (A_{FC}) before charging. Similarly, a voltage of $+0.9$ V between S and the fuel cell-type cathode (C_{FC}) was measured before discharging under constant oxygen flow (0.157 l h^{-1}). The experimental setup is shown in Figure 3.9 a) and b).

When the A_{FC} was connected to S through a 5.5 Ω resistor, an anodic current flowed, charging the double layer and the pseudocapacitance in the supercapacitor-type electrode, as it was also observed in the experiments with the two-electrode hybrid cell. After the charging process was finished (after ca. 120 s), S was connected also through a 5.5 Ω resistor to the C_{FC} and then a cathodic current flowed as a consequence of discharging the double layer and the pseudocapacitance. Typical charging-discharging curves, using supercapacitor-type electrodes with a BP mass loading of 2.8 mg cm^{-2} and 10 M H_2SO_4, are shown in Figure 5.3.

These curves exhibit a double-exponential current-response in function of time as shown in Figure 5.4 for the second charging-discharging cycle. It was also noted that the current in both processes does not reach zero after 100 s. At 100 s the charging and discharging currents amount to ca. 0.1 A g^{-1}. The results of the bi-exponential analysis are listed in Table 5.2. Although this behavior was also observed in the charging-discharging experiments with the two-electrode hybrid cell the time constants are in this case lower, as shown in Table 5.3 and 5.4. However, by comparing Figure 4.10 with Figure 5.3 it is observed that the currents at time zero for both charging and discharging processes in the latter were a factor 1.6 higher than in the former. These results are related with the use of lower external load resistance.

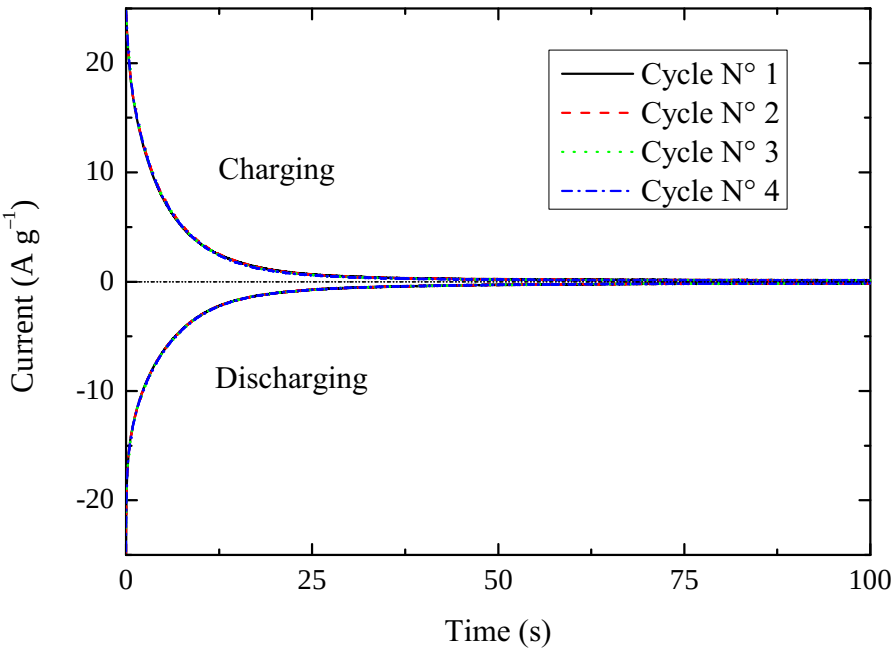

Figure 5.3: Charging-discharging curves of the three-electrode hybrid cell operated as a supercapacitor using 10 M H_2SO_4 as electrolyte.

In order to confirm this tendency charging-discharging experiments using a lower load resistance of only 0.22 Ω were performed (see Figure 5.5), in which case the SIC was the lowest during charging but higher than the SIC value obtained for the two-electrode hybrid cell during discharging (see Table 5.3 and 5.4). In this case the SIC was calculated over an integration time (t_{INT}) of 30 s. This is due to the high noise present during the measurements after the current reaches values close to 0.4 A g^{-1} (after about 40 s).

Reversibility and reproducibility of the charge-discharge processes over 100 cycles were tested. The duration of each charging or discharging process was 120 s and the resistance 1.16 Ω. Figure 5.6 shows the result of 100 charge-discharge cycles. Charging and discharging process are denoted by negative and positive current respectively. The current at the end of the discharging process (after about 120 s) does not reach zero, it stabilizes at a value of ca. 0.6 A g^{-1}. Different peak values of the current are observed for charging and discharging in different cycles.

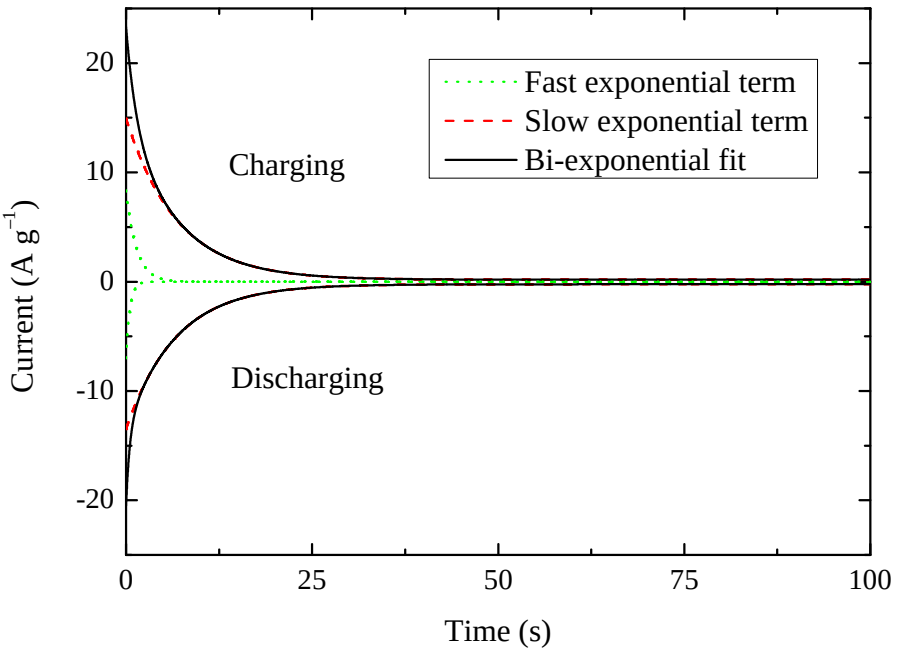

Figure 5.4: Bi-exponential analysis of the second-cycle charging-discharging curve of the three-electrode hybrid cell operated as a supercapacitor, using an external resistance of 5.5 Ω.

Table 5.2: Bi-exponential analysis results from the data of Figure 5.3 for 4 charging (CH)-discharging (DCH) cycles. The SIC from the original curves was calculated over 120 s. "Losses" refers to the amount of SIC in % which is not recuperated by discharging.

Cycle N°	$\tau_{1,CH}$ (s)	$\tau_{2,CH}$ (s)	SIC_{CH} (C g^{-1})	$\tau_{1,DCH}$ (s)	$\tau_{2,DCH}$ (s)	$\mid \mathrm{SIC}_{DCH} \mid$ (C g^{-1})	Losses (%)
1	1.38	6.85	134.22	0.50	6.67	119.78	10.8
2	1.16	6.62	134.44	0.43	6.62	119.88	10.8
3	1.08	6.42	131.27	0.51	6.69	120.24	8.4
4	1.01	6.32	130.90	0.42	6.61	120.39	8.0

5.2.2 Discussion

Similar to the results obtained with the two-electrode hybrid cell, an OCV of about −0.8 V just before the charging process was observed between the fuel cell-type an-

Table 5.3: SIC of charging process (second cycle) of the two-electrode hybrid cell (2-EHC) and the three-electrode hybrid cell (3-EHC) (both operated as a supercapacitor) through different external load resistances (R_{EXT}).

Cell	R_{EXT} (Ω)	t_{INT} [a] (s)	Sub-process	τ (s)	% of SIC (%)	SIC_{total} (C g^{-1})
2-EHC	10	120	fast	7.6	78	120.3
			slow	82.9	22	
3-EHC	5.5	120	fast	1.4	9	134.2
			slow	6.9	91	
	0.22	30	fast	0.2	15	114.6
			slow	2.6	85	

[a] t_{INT} represents the integration time used for the calculations of the SIC.

ode and the supercapacitor-type electrode. After the charging process was finished, an OCV between the supercapacitor-type electrode and the fuel cell-type cathode

Table 5.4: SIC of discharging process (second cycle) of the two-electrode hybrid cell (2-EHC) and the three-electrode hybrid cell (3-EHC) (both operated as a supercapacitor) through different external load resistances (R_{EXT}). "Losses" refers to the amount of SIC in % which is not recuperated by discharging.

Cell	R_{EXT} (Ω)	t_{INT} [a] (s)	Sub-process	τ (s)	% of SIC (%)	$\lvert SIC_{total} \rvert$ (C g^{-1})	Losses (%)
2-EHC	10	120	fast	7.6	55	103.6	13.9
			slow	56.8	45		
3-EHC	5.5	120	fast	1.4	3	119.8	10.7
			slow	6.9	97		
	0.22	30	fast	0.2	15	110.1	3.9
			slow	1.8	85		

[a] t_{INT} represents the integration time used for the calculations of the SIC.

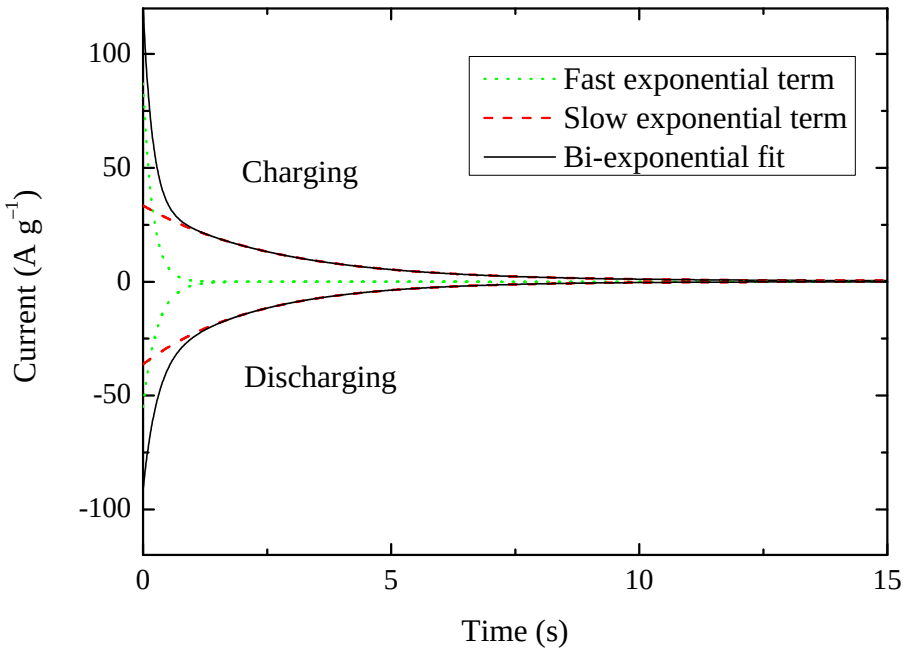

Figure 5.5: Bi-exponential analysis of the charging-discharging curves of the three-electrode hybrid cell operated as a supercapacitor using an external load resistance of 0.22 Ω.

of +0.8 V was measured. The origin of these voltages was already discussed in the previous chapter.

The curves in Figure 5.3 also exhibit a bi-exponential behavior. The results of the bi-exponential analysis are presented in Figure 5.4 and in Table 5.3 and 5.4. Typical time constants were 1.4 and 7 s for charging and 0.5 s and 6.7 s for discharging the supercapacitor. These time constants are smaller than those obtained in the two-electrode hybrid cell experiments using 7 M H_2SO_4. It was also observed that the currents at $t = 0$ were a factor 1.6 higher in these experiments. This is mainly due to the use of a lower external resistance, which in this case was 5.5 Ω. We believe that the value of the time constants were related to the supercapacitor resistance and capacitance, in a similar way as in a conventional dielectric capacitor ($\tau = RC$). It was also expected that the capacitance remained unaltered in these experiments.

Through the bi-exponential analysis of these curves it can be assumed that at least two sub-processes independent from each other take place. In a similar way as in the experiments with the two-electrode hybrid cell, a “fast” and a “slow” sub-processes are considered. In the bi-exponential analysis of those experiments we presumed

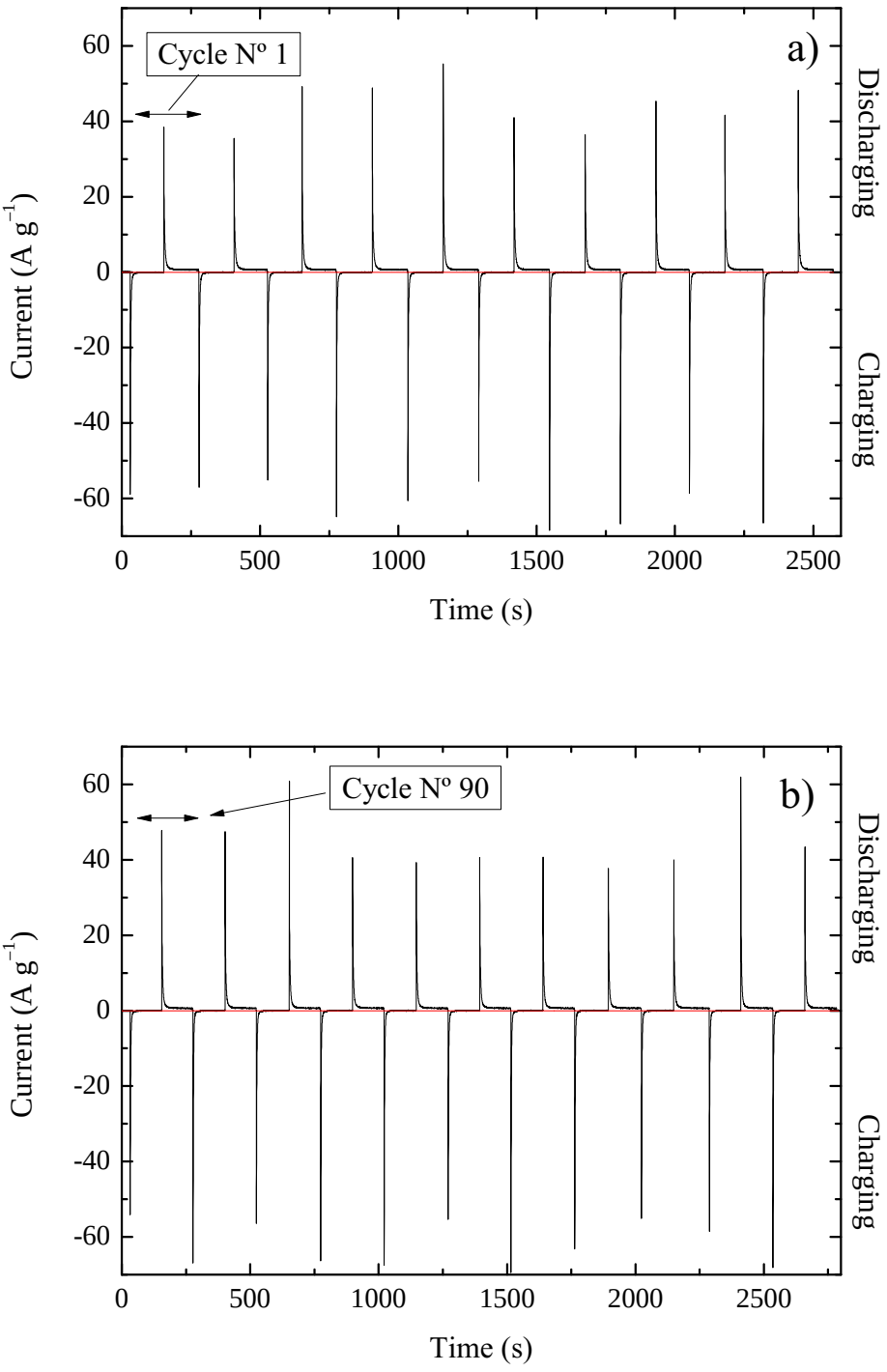

Figure 5.6: Charging-discharging curves of the three-electrode hybrid cell operated as a supercapacitor. a) cycle 1-10 and b) cycle 90-100.

that the charging or discharging of the pseudocapacitance and the external double layer take place during the fast sub-process. However, the contribution of the sub-

process with the smallest time constant (about one second) to the total SIC during the charging process in these experiments was only 10% (see Table 5.3). The same behavior was observed in the discharging process where this contribution is even less than 10% (see Table 5.4).

As discussed in the previous chapter the contribution of the pseudocapacitance to the total capacitance of these carbon materials normally lies in the range of 5-10%. In fact, for BP the high pH value (9.5) and the low content of volatile (2%) indicate a low concentration of oxygen-based surface active functionalities. It is also known that the pseudocapacitance is strongly dependent on potential. At the beginning of the charging and discharging process the voltage between the two electrodes was maximum and it decayed also exponentially with time. Therefore, it is expected that this type of capacitance was charged and discharged during the first seconds of the charging or discharging process when the voltage was high enough. These evidences support the idea that, in this case, the fast sub-process is mainly related to the pseudocapacitive behavior of the supercapacitor-type electrode. In contrast, the slow sub-process which contributed with 90% to the SIC and exhibited time constants of ca. 7 s is then associated with the charging of the external double layer and to a minor extent than it was observed in the experiments with the two-electrode hybrid cell with charging the internal double layer. This would agree also with the fact that ca. 83% of the BET surface area of BP is considered as relatively easily accessible surface area (external surface area + mesoporosity).

Although it is commonly assumed that the charging and discharging of the double layer in electrode/electrolyte interfaces is a fast process (within milliseconds), in our experiments these are affected by the value of the external resistance and the diffusion of the protons towards the supercapacitor-type electrode. For example, Figure 5.4 shows a bi-exponential analysis of charge-discharge curves performed with a resistance of 0.22 Ω. The time constant of the fast sub-process during charging and discharging process amounts to 0.20 s and for the slow sub-process to ca. 2.5 s (see Table 5.3 and 5.4).

Higher currents at $t = 0$ are observed in Figure 5.5 than in Figure 5.4. However, the SIC of the charging and discharging processes in the experiments using a 0.22 Ω resistance is about 15% and 9% lower than that of the experiments where a 5.5 Ω resistance were used. With a lower resistance almost all the SIC due to the charging and discharging of the pseudocapacitance and the external double layer flows in very little time, resulting in a higher current peak.

These results show that by decreasing the external resistance higher currents at $t = 0$, but lower SIC values and time constants are obtained. This also means that

the contribution of the fast sub-process to the SIC is incremented and that of the slow sub-process is reduced. Since the time constants are smaller, there is less time to charge the internal double layer.

The results of 100 charging-discharging cycles exhibit a good reversibility and reproducibility (see Figure 5.6). Also the SIC for charging and discharging in the first cycle was almost the same as that in the 100th cycle. However, experiments over more than 10^6 cycles should be performed in order to obtain an estimation of the cycle lifetime of this device. It is observed that the charging and discharging current peak values fluctuate. This is due to instrumental resolution effects, i.e. that the rate at which the current values changed at the beginning of the charging and discharging process is higher than the frequency at which the data were recorded. In fact, due to the high number of points involved in such long measurements the resolution of the potentiostat was set to only 5 points per second. In order to illustrate this idea a 15 cycles charging-discharging experiment performed at a higher experimental resolution of 50 points per second is shown in Figure 5.7 in which case the fluctuation of the current peak values is negligible.

It was observed that the current at the end of the discharging time of about 120 s did not reach zero. Experiments performed with higher external resistances (about 50 Ω) have shown that the discharging current at the end of the process reaches zero when the H_2 flow is interrupted. This suggests that even when the A_{FC} was disconnected, some charging of the carbon black surface took place simultaneously with the discharging process. However, this phenomenon is still not fully understood.

5.3 Operation as a hybrid device

5.3.1 Results

The operation of the three-electrode hybrid cell as a hybrid device involves the charging and discharging of the supercapacitor-type electrode as a source of high energy density in short time during the simultaneous operation of the device as a PEM fuel cell. For reasons of clarity we will subsequently refer to this cell operated as a fuel cell as "fuel cell". Similarly, when the cell is operated as a supercapacitor we will refer to it as "supercapacitor".

We explored the behavior of the charging-discharging curves under different operation conditions of the fuel cell, such as under interruption of the fuel flow and at different fuel cell current densities (i_{FC}) and power.

In the hydrogen flow interruption experiments we first charged the supercapacitor

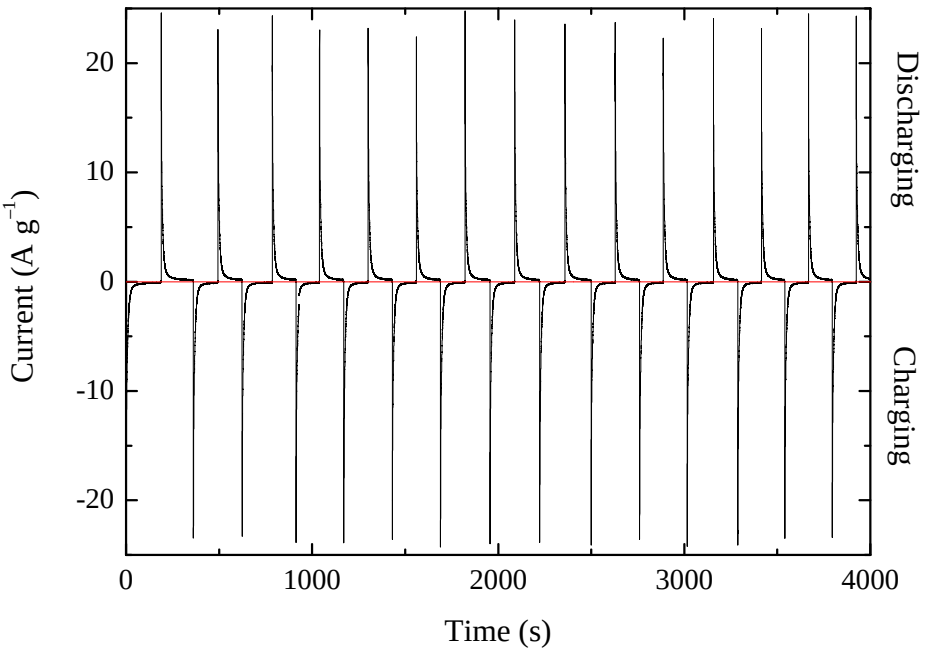

Figure 5.7: Charging-discharging curves (15 cycles) of the three-electrode hybrid cell operated as a supercapacitor. The external load resistance in this case was 5.0 Ω, and the experimental resolution is a factor of 10 higher than in Figure 5.6.

for 3 min and left it connected to the anode after the hydrogen flow had been interrupted. The experimental setup used is sketched in Figure 3.13. The current response of the fuel cell and of the hybrid device were monitored before and after the interruption of the hydrogen flow. The results are shown in Figure 5.8. At 60 s the hydrogen flow was interrupted. The initial value of the i_{FC} was ca. 40.3 mA cm^{-2}, the resistance R was set to 10 Ω. A decrease of the current occurred 30 s after the hydrogen flow had been interrupted. In the time range of 100 to 150 s the curves show a different progression. This difference can be expressed in terms of SIC which amounts to 50 C g^{-1}.

The charging and discharging of the supercapacitor were performed during the fuel cell operation. The results are presented in two sets of experiments. With the setup shown in Figure 3.10 we measured the charging and discharging currents in function of time through a known resistance R_S (5.0 Ω) at different i_{FC}.

The results of the bi-exponential analysis of these curves are listed in Table 5.5 and 5.6. This analysis has revealed that the time constants remained in the same order of

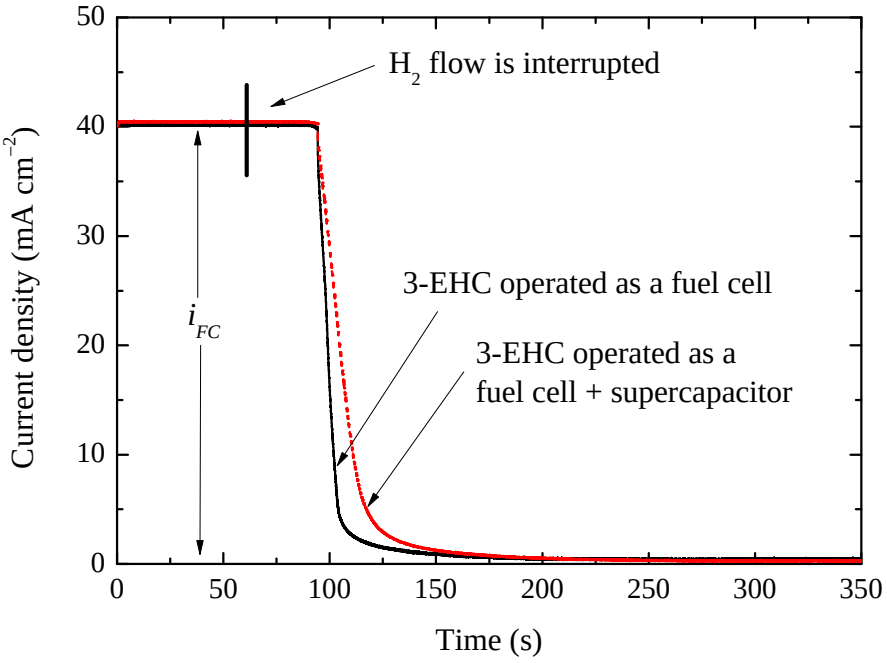

Figure 5.8: Current response of the three-electrode hybrid cell operated as a fuel cell and as a hybrid device after interruption of the hydrogen flow.

magnitude (for the fast sub-process between 0.6 and 2 s and for the slow one in the range of 6-8 s during charging and discharging) when the i_{FC} was varied. Also the contribution of each sub-process to the total SIC during charging remained relatively constant, i.e. for the fast sub-process amounted to 2-3% of the SIC. However, the contribution of this sub-process to the SIC during discharging increased gradually from 3 to 10% when the i_{FC} was incremented (see Table 5.6).

The power that developed in R_S as a function of time during charging and discharging is shown in Figure 5.9 a) and b), respectively. The negative sign of the power density during discharging the supercapacitor indicates only the direction of the current flow which in this case is the opposite as during charging. These curves also exhibit an exponential decay, and after about 20 s the power density reaches zero. The maximum value of peak power density for charging (57.38 mW cm^{-2}) and for discharging (63.14 mW cm^{-2}) was observed at the lowest i_{FC}, and it decreases for each curve when i_{FC} increases as shown in Table 5.7.

In addition to these experiments, we tested this cell during hybrid operation by using the experimental setups sketched in Figure 3.11 and 3.12 in section 3.4.2. The idea was to design an experiment to measure the contribution of charging and

Table 5.5: SIC of charging process (second cycle) of the supercapacitor-type electrode of the three electrode hybrid cell when it is operated as a hybrid device at different fuel cell currents. The value of R_S in these experiments was 5.0 Ω

Fuel cell current (i_{FC}) (mA cm^{-2})	Sub-process	τ (s)	% of SIC (%)	SIC$_{total}$ (C g^{-1})
0.008	fast	0.61	2.4	156.85
	slow	7.92	97.6	
0.075	fast	0.57	2.2	152.58
	slow	7.53	97.8	
11.3	fast	0.68	2.6	121.49
	slow	6.96	97.4	
18.9	fast	0.72	2.6	113.08
	slow	6.79	97.4	
30.1	fast	0.75	2.5	103.33
	slow	6.64	97.5	
45.2	fast	0.82	2.7	93.28
	slow	6.59	97.3	
75.3	fast	1.17	3.4	73.42
	slow	6.67	96.6	

discharging the supercapacitor to the power density developed by the fuel cell in an external resistor.

Figure 5.10 a) shows the power density developed in R_{CH} by the fuel cell before charging the supercapacitor and the power developed by both elements during the charging process. The corresponding results of the discharging process are presented in Figure 5.10 b) in which the negative sign of the power density only signalizes the direction of current flow. The value of the resistance in R_{CH} and R_{DCH} was set to 5.0 Ω. The maximum power density decreases with the increment of the i_{FC} and the fuel cell power (P_{FC}) as shown in Table 5.8 and 5.9.

Simultaneously with incrementing the power in R_{CH} or R_{DCH} during charging or discharging the supercapacitor, the voltage between the fuel cell anode and cathode decreased by several millivolts. It returned also exponentially to its original value with the same time constant as the power density did.

Table 5.6: SIC of discharging process (second cycle) of the supercapacitor-type electrode of the hybrid cell when it is operated as a hybrid device at different fuel cell currents. The value of R_S in these experiments was 5.0 Ω. "Losses" refers to the amount of SIC in % which is not recuperated by discharging.

Fuel cell current (i_{FC}) (mA cm^{-2})	Sub-process	τ (s)	% of SIC (%)	$\mid SIC_{total} \mid$ (C g^{-1})	Losses (%)
0.008	fast	0.72	3.0	147.33	6.1
	slow	7.62	97.0		
0.075	fast	0.92	3.6	146.79	3.8
	slow	7.73	96.5		
11.3	fast	1.36	4.8	114.97	5.4
	slow	7.57	95.2		
18.9	fast	1.30	4.5	106.33	6.0
	slow	7.24	95.5		
30.1	fast	1.37	4.7	96.68	6.4
	slow	6.96	95.2		
45.2	fast	1.77	6.6	85.94	7.9
	slow	6.99	93.4		
75.3	fast	2.36	9.7	64.09	12.7
	slow	6.89	90.3		

5.3.2 Discussion

The difference between the current decay of the three-electrode cell, as a result of the interruption of the hydrogen flow when the switch of the supercapacitor-type electrode was opened and when it was closed, is a clear indication of the hydrogen buffer properties of this supercapacitor. In the absence of hydrogen in the fuel cell-type anode the protons which were previously stored in the double layer during the charging process were consumed in the fuel cell-type cathode.

A current of ca. 9 A g^{-1} could not be held only through the discharge of the carbon black electrode. However, a charge of 50 C g^{-1} still flowed giving some smoothing effect to the current decay, as illustrated in Figure 5.8. A SIC of 50 C g^{-1} is about 50% less than that achieved during the discharging process in previous charge-discharge experiments. This suggests that there was a charge leak in the system.

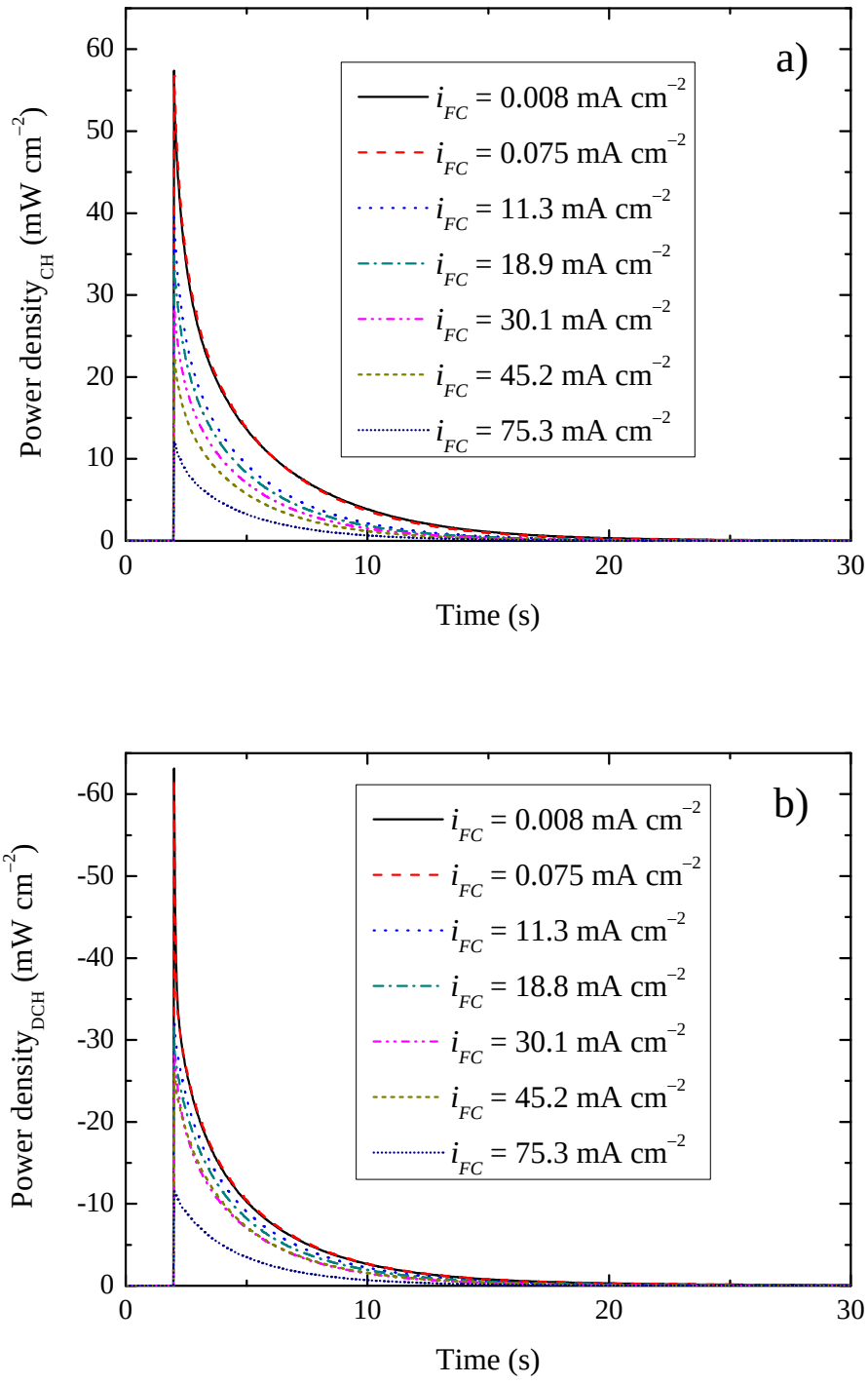

Figure 5.9: Power density of the supercapacitor in function of time in the resistor R_S during a) charging and b) discharging at different i_{FC}.

Although the hydrogen flow was interrupted, a certain quantity of it remained inside the gas ducts. This hydrogen was consumed during the first 40 s before the

Table 5.7: Power density that developed in R_S during charging (CH) and discharging (DCH) process of the supercapacitor-type electrode of the cell when it is operated as a hybrid device at different fuel cell currents.

Fuel cell current (i_{FC}) (mA cm^{-2})	Peak power$_{CH}$ (mW cm^{-2})	| Peak power$_{DCH}$ | (mW cm^{-2})
0.008	57.38	63.14
0.075	56.77	61.83
11.3	39.47	31.52
18.9	34.81	31.68
30.1	28.43	28.42
45.2	22.50	26.09
75.3	12.18	11.78

current decay occurred. When almost all the hydrogen had either been consumed or had diffused out into the atmosphere the current fell to zero. This process went on simultaneously with the diffusion of air inside the anode chamber. When it is filled with air then a voltage between the fuel cell-type anode and the supercapacitor-type electrode emerges. Due to this fact, the protons in the supercapacitor-type electrode had two ways to diffuse out, towards the cathode (where the oxygen concentration was higher than in air) or to the anode (where oxygen from air was present). It is important to note that the fuel cell-type electrode (former anode when it was in

Table 5.8: Power density that developed in R_{CH} by the fuel cell (P_{FC}) before charging and by the fuel cell + supercapacitor (P_{FC+S} peak value) during charging the supercapacitor-type electrode of the cell when it is operated as a hybrid device at different fuel cell currents. The power density increment by charging the cell (ΔP) is also shown.

Fuel cell current (i_{FC}) (mA cm^{-2})	P_{FC} (mW cm^{-2})	P_{FC+S} (mW cm^{-2})	ΔP (mW cm^{-2})
3.1	0.06	36.70	36.65
32.3	3.86	27.22	23.36
47.9	9.83	20.54	10.71
60.4	15.87	17.44	1.57

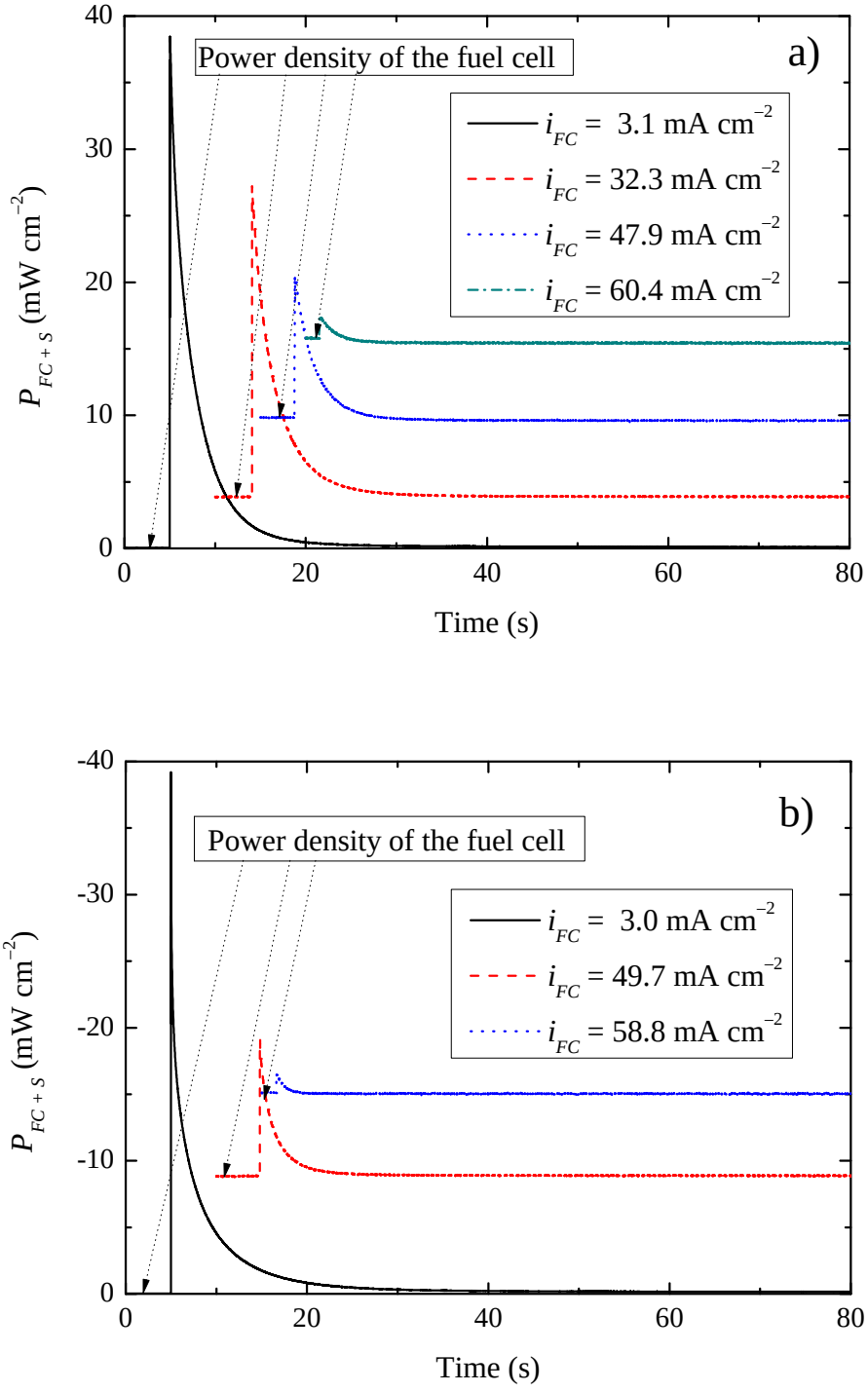

Figure 5.10: Power developed in a)R_{CH} before and after charging and in b)R_{DCH} before and after discharging of the supercapacitor at different i_{FC}.

contact with H_2) acted as a cathode as soon as it was in contact with oxygen. This is the origin of the leak: a fraction of the protons diffusing in the opposite direction,

Table 5.9: Power density (in absolute value) that developed in R_{CH} by the fuel cell (P_{FC}) before discharging and by the fuel cell + supercapacitor (P_{FC+S} peak value) during discharging the supercapacitor-type electrode of the cell when it is operated as a hybrid device at different fuel cell currents. The power density increment by discharging the cell is also shown.

Fuel cell current (i_{FC}) (mA cm^{-2})	P_{FC} (mW cm^{-2})	P_{FC+S} (mW cm^{-2})	ΔP (mW cm^{-2})
3.0	0.02	39.20	39.18
49.7	8.87	19.06	10.19
58.8	15.06	16.56	1.50

generating the loss.

The reversible charging and discharging processes of the supercapacitor generate a relatively high current in a short time. We can take advantage of this feature in order to complement a primary energy source such as a fuel cell in case of a peak power demand. The results shown in Figure 5.9 a) illustrate this idea. The three-electrode hybrid cell is operated as a fuel cell, generating a current from the oxidation of hydrogen at the anode and reduction of oxygen at the cathode. When the supercapacitor-type electrode is connected to the electrical circuit (switch W in position (1), see Figure 3.11 in section 3.4.2), an extra charging current flows through the resistor R_S, generating a peak of power which decays bi-exponentially to zero with typical time constants of about 0.5 and 8 s (see Table 5.5). A similar behavior is observed during discharging. This high power delivered in a short time can be used independently from the fuel cell operation. However, the power that can be obtained from the charging or discharging of the supercapacitor is limited at high fuel cell current densities.

In these experiments the charging of the external double layer and the pseudocapacitance in the supercapacitor-type electrode is possible because of the fast electrode kinetics of the hydrogen oxidation in comparison with the sluggish electrode kinetics of the oxygen reduction (exchange currents of about 10^{-4} vs. 10^{-9} A cm^{-2} Pt at 25°C and 1 atm) [8]. In this way the supercapacitor can be charged during the fuel cell operation. Nevertheless, smaller charging power peak were observed when the current density of the fuel cell increased. The transport of the protons through the two Nafion® membranes and the supercapacitor-type electrode towards the cathode under these conditions could have inhibited the formation of the double layer at the

carbon black surface. Additionally, the high depolarization of the anode at high fuel cell currents led to a decrease in the OCV between the anode and the supercapacitor-type electrode which was the driving force needed to charge the double layer and the pseudocapacitance. Consequently, the supercapacitor cannot be charged to the same level as observed at low current densities.

The discharging of the double layer and pseudocapacitance of the supercapacitor-type electrode was also influenced by the current density of the fuel cell, as illustrated in Figure 5.9 b). The power obtained from discharging the supercapacitor is directly related with the level at which it was previously charged. Due to this fact, also a small power peak is observed at a high current density during the discharging process.

Some efforts are devoted to the hybridization of a fuel cell and a supercapacitor as an auxiliary power source in order to improve the efficiency and response capacity of the system to a fast load demand, which is a common situation, for example, in vehicle applications [32, 53, 62, 63]. However, these hybrid configurations normally consist of two discrete units which are electrically coupled in a parallel way. In our system, the supercapacitor was integrated inside a PEM fuel cell forming a single hybrid module consisting in two Faradaic fuel cell-type electrodes coupled internally with a capacitive electrode. This design permits the charging and discharging of the supercapacitor without applying any external current or voltage but with losses in the fuel cell power as a consequence of incrementing the internal resistance of the cell.

Figure 5.10 a) and b) show the increment in power density in function of the fuel cell current density developed in a 5 Ω resistor (R_{CH}) during the charging and discharging process. The highest increment of about 40 mW cm^{-2} was observed by discharging at the lowest fuel cell current density (see Table 5.8 and 5.9). The contribution of charging or discharging the supercapacitor to the total power density developed in R_{CH} is clearly apparent.

The decrease of several millivolts in the voltage between the A_{FC} and the C_{FC} was a consequence of the depolarization of the anode. The voltage returned exponentially to its original value with the same time constant as did the power density. Furthermore, at higher i_{FC} the voltage decrease was less pronounced. Having in mind the circuit shown in Figure 3.11, a decrease in the fuel cell voltage (V_1) means that while the total current density in R_{CH} increases, the current at R actually decreases. However, the current increment in R_{CH} was higher than the current decrease in R. For example, for a fuel cell current density of 32.3 mA cm^{-2} and a R of 10 Ω the effect of charging the supercapacitor leads to an increase of the current density to a

maximum of 86 mA cm^{-2} while in R_{CH} it decreases from 47.9 to 45.0 mA cm^{-2}.

A voltage decrease between anode and cathode also occurred during the discharging process. In this case it was due to the cathode depolarization. As in the charging process the voltage returns exponentially to its original value and the current increment of in R_{DCH} was also higher than the decrease of the current in R.

An exact comparison of our results with other works in the field of fuel cell-supercapacitor hybridization is difficult. As discussed before, the hybridization of two discrete elements is considered and an improvement of the fuel cell voltage is pursued. Asymmetric capacitor devices based on the combination of a capacitor and battery-type electrodes have also been studied. However, a voltage or a constant current have to be applied in order to charge these devices [33, 34].

The results of the hybridization of a direct methanol fuel cell (DMFC) with an all-solid-state supercapacitor have shown that the power density of a fuel cell operated under a constant current increases rapidly by about 11 mW cm^{-2} from 36 mW cm^{-2} in a short time after the hybridization [53]. In these experiments the energy of the supercapacitor was transferred to the DMFC during the discharging process, increasing the cell voltage from 0.35 V to 0.45 V. However, energy should have been spent in oder to charge the supercapacitor separately from the DMFC. In our experiments an increase in a PEM fuel cell performance in an resistor through the charging and discharging of an internal supercapacitor was observed.

5.4 Summary

We first explored the behavior of the three-electrode hybrid cell operated as a fuel cell. The aim of these experiments was to determine with which electrolyte and at which concentration the cell exhibited the highest performance. The cell exhibited the lower ohmic losses using 10 M H_2SO_4. Also the maximum power density of about 22 mW cm^{-2} was observed at this concentration. However, this value is very low in comparison with typical reported PEM fuel cell performances (1 W cm^{-2}). This was attributed to the increment of the proton diffusion distance by a factor of 40 and to the low open ratio of the graphite electrode.

After the electrolyte and the experimental conditions had been selected we performed charging-discharging experiments of the cell operated as a supercapacitor. Good reproducibility and reversibility were observed over 100 charging-discharging cycles. However, experiments with more than 10^6 cycles should be performed in order to estimate the cycle lifetime of this device.

The current-versus-time response during charging and discharging also exhibited a

bi-exponential behavior. The time constants were smaller than those observed in the experiments with the two-electrode hybrid cell, as a consequence of the lower external resistance value. Two sub-processes were assumed to happen. A fast sub-process related with the charging of the pseudocapacitance which represented 10% of the total SIC and a slow sub-process related with the charging of the double layer. It is estimated that the internal double layer at these time constants could not be charged to the same extent as in the the experiments with the two-electrode hybrid cell. Therefore, the charging and discharging of the supercapacitor under these conditions involved the participation of the external surface area and the pseudocapacitance. This agrees with the fact that for BP the relatively easily accessible mesoporous area and external surface area represent an important contribution to the BET surface area.

With the inclusion of the carbon black electrode inside a PEM fuel cell we explored a new concept of fuel cell-supercapacitor hybridization. The idea was to take advantage of the high energy density delivered by a supercapacitor in a very short time and combine it with an energy converter system such as a fuel cell.

The ability of the supercapacitor of developing and also increasing the total power during the charging-discharging experiments in a resistor was explored in two situations. First, when no fuel cell current flowed through an external resistor and secondly, when a fuel cell current flowed through a resistor, developing power on it. Hydrogen interruption experiments were also performed. In these tests we explored the capacity of the supercapacitor in smoothing the fuel cell current decay when the hydrogen flow was interrupted.

The results have shown that a power density developed in an external resistor connected between the carbon black electrode and the anode during the charging process even when the hybrid cell was operated as a fuel cell. Similar observations were made during the discharging process. A maximal power of about 60 mW cm^{-2} was observed at the lowest i_{FC} (0.008 mA cm^{-2}). The higher the i_{FC}, the smaller the peak power value.

Also an increment of the power developed by the i_{FC} in an internal resistor by charging or discharging the supercapacitor was noted. A maximal power increment of about 40 mW cm^{-2} occurred when the i_{FC} was 3.1 mA cm^{-2}. In contrast, when the i_{FC} and power generated by the the fuel cell were about 60 mA cm^{-2} and 16 mW cm^{-2} an increment of only 4 mW cm^{-2} occurred.

These evidences indicate that the use of the three-electrode hybrid cell as a new concept of hybrid device based on the combination of a supercapacitor and fuel cell-type electrodes is viable. Increments in the power developed in an internal and also

external resistor practically independent from the fuel cell operation were observed. This show the potential of the supercapacitor-electrode as an extra power delivery system inside a PEM fuel cell to be used in case of peak power demand. An exact comparison of this system with the typical fuel cell-supercapacitor and battery-supercapacitor hybrid devices is difficult due to the differences in design and in the characterization methods.

6 Final summary and conclusions

Hydrogen has emerged as one of the most serious candidates to replace fossil fuels especially for the transportation sector. This is mainly due to its environmental friendliness since the only exhaust gas resulting from using it, for example in fuel cells, is water vapor. However, an important challenge which has to be overcome in order to make this technology efficient and safe enough to compete with combustion engine machines is hydrogen storage. In almost all available hydrogen storage options high pressures or low temperatures have to be used not only for storage but even for release of hydrogen thereby consuming a considerable amount of energy. Some of these methods have also problems with reversibility. Therefore, we decided to explore a new concept of hydrogen storage which operates reversibly near ambient conditions and without important energy losses and which is based on the hybridization between a fuel cell and a supercapacitor.

The main idea consists in the electrochemical splitting of hydrogen at a PEM fuel cell-type electrode into protons and electrons and then in the storage of these two species separately in the electrical double layer of a supercapacitor-type electrode which is made of electrically conductive large-surface area carbon materials. A large surface area is needed in order to achieve high hydrogen storage capacities.

Assuming that all carbon atoms are exposed to the surface and that each carbon atom can carry a negative charge, then one H_3O^+ in solution would be necessary to compensate this negative charge in the carbon forming the double layer. A theoretical storage capacity of about 7 wt.% H_2 is then calculated by considering that in order to store a hydrogen atom in this system one water molecule and one carbon atom are necessary.

The investigation of this concept was performed first using a two-electrode fuel cell-supercapacitor hybrid device. The fuel cell-type electrode was made of platinum supported on carbon black with catalyst loadings of about 0.45 mg cm^{-2}. Nafion® 112 membranes were used as separator. H_2O, NaOH and H_2SO_4 were used as electrolytes in the supercapacitor-type electrode side. High-surface-area (BET = 1155 m^2 g^{-1}) carbon black Black Pearls 2000 was used as a supercapacitor-type electrode with mass loadings in the range of 0.7 to 3.8 mg cm^{-2}.

Spontaneous reversible charging and discharging of this cell was achieved simply by changing the gas feed in the fuel cell-type electrode (H_2 for charging, O_2 for discharging) without applying any current or voltage near ambient conditions using H_2O and different electrolytes. However, the H_2 storage capacities obtained were small. The highest hydrogen storage capacity of 0.17 wt.% and 0.13 wt.% during charging and discharging were found using 7 M H_2SO_4 and at a hydrogen pressure of 2.5 bar. Although the H_2 storage capacities are small, the combustion energy of the hydrogen stored in this cell at the storage capacity of 0.13 wt.% is a factor 2.6 higher than the electrical energy stored on a symmetric supercapacitor of comparable high quality.

The driving force of the charging and discharging processes is the potential difference between the two electrodes, originating in the difference of the redox potentials of the electrochemical reactions involved. These reactions are the electrochemical oxidation of H_2 at the fuel cell-type electrode vs. the reduction of the oxygen-based surface groups (e.g. quinone type) at the supercapacitor-type electrode (carbon black layer) during charging and the electrochemical reduction of O_2 vs. the oxidation of the oxygen-based surface groups during discharging.

The decrease of several mbar in the H_2 pressure during the charging process confirmed that H_2 was oxidized at the fuel cell-type electrode and oxygen-based surface electroactive groups (pseudocapacitance) were reduced at the supercapacitor-type electrode, simultaneously with the charging of the double layer. During the discharging process the protons were transported back through the membrane towards the fuel cell-type electrode where they combined with oxygen and electrons to form water. Simultaneously, the surface electroactive groups in the carbon black surface were oxidized.

From the bi-exponential analysis of the asymmetric charging-discharging current-versus-time curves it is derived that at least two sub-processes took place during charging and discharging the cell. The first one corresponds to a fast sub-process, associated with the charging and discharging of the double layer at the external surface of the carbon black layer and with the charging and discharging of the pseudocapacitance generated by the oxygen-based redox surface functionalities. It exhibits typical time constants of 8 s using 7 M H_2SO_4 as electrolyte. The second one is considered a slow sub-process, which is related to the charging and discharging of the double layer at the internal surface of the carbon black layer (porous system) with typical time constants in the range of 50 and 80 s using 7 M H_2SO_4 as electrolyte.

The results of the charging-discharging experiments at different H_2 pressures using H_2O indicate that the hydrogen storage capacity of the cell was near to saturation

at the H_2 pressure of 1.5 bar. At this pressure 0.063 wt.% of H_2 was stored which corresponds to ca. 0.01 e^- per C atom and is very far from the initially envisaged value of 1 e^- per C atom. A pressure increment of two bar led to an increment of only 22% in the H_2 storage capacity. The main capacity limitations in this system are due to the electrostatic repulsion between the surface charges, the limited amount of surface atoms which can carry a full charge and their accessibility by the ions in the electrolyte solution. Moreover, not all carbon atoms were wetted by the electrolyte or even electrically connected to the current collector.

The capacitances of the device using different electrolytes were obtained from galvanostatic and cyclic voltammetry experiments. The results obtained were the following: 7 μF cm^{-2} for H_2O and 12 μF cm^{-2} for 7 M NaOH and H_2SO_4. The difference in the capacitance values using different electrolytes is attributed to the change in the structure of the double layer and the influence of the pH on the redox potential of the pseudocapacitive reactions. These specific capacitances are close to the typical reported values for the double layer capacitance of carbon blacks in aqueous electrolytes.

The flow of electrons through the external circuit generated by the spontaneous charging and discharging of the cell produced a peak power of about 20 mW cm^{-2} in the external load resistance. This showed the potential of the device as an extra power complement (to be used in case of peak power demand) for a primary power source, such as a PEM fuel cell. To explore this idea, an advanced design of the original cell was investigated. This new design is based in the combination of two fuel cell-type electrodes (anode and cathode of a PEM fuel cell) with a supercapacitor-type electrode also in a single-cell configuration. The performance of this three-electrode fuel cell-supercapacitor hybrid cell when it was operated as a PEM fuel cell was about 22 mW cm^{-2}, which is very low in comparison with typical PEM fuel cell performances of 1 W cm^{-2}. This is due to the increase of the proton diffusion distance by a factor of 40 in this cell and to the low open ratio of the graphite electrode.

The charging-discharging behavior of this cell when it was operated as a supercapacitor showed good reproducibility and reversibility over 100 cycles. The current-versus-time response also exhibited a bi-exponential behavior. However, the time constants were smaller than those observed in the experiments with the two-electrode fuel cell-supercapacitor hybrid cell (between 0.5 and 1 s for the fast sub-process and between 3 and 7 s for the slow one) as a consequence of the lower external resistance value. In this case, the fast sub-process was associated with the charging-discharging of the pseudocapacitance.

The ability of the supercapacitor-type electrode of incrementing the power density developed by the fuel cell in an external load resistance depends on the value of the current at which the fuel cell is operated (i_{FC}). The total power density (fuel cell power + supercapacitor power) was increased by up to values of 40 mW cm^{-2} for a few seconds by charging and discharging when the i_{FC} was 3.1 mA cm^{-2}. In contrast, when the i_{FC} was about 60 mA cm^{-2} an increment of only 4 mW cm^{-2} occurred. This is due to depolarization effects on the fuel cell-type electrodes at high i_{FC} values. These increments in the power developed in the external resistor are obtained practically independently from the fuel cell operation. This offers the possibility to release the energy of the fuel cell electrodes at the higher rate of energy delivery of the supercapacitor electrode.

These results indicate that the novel concept of hydrogen storage by hybridization of a fuel cell with a supercapacitor explored in this work using two-cell designs is viable. An exact comparison of this system with the typical fuel cell-supercapacitor and battery-supercapacitor hybrid devices is difficult because of the differences in design and in the characterization methods. However, Table 6.1 and 6.2 show a general comparison between a typical supercapacitor electrode and the two-electrode hybrid cell and between a PEM fuel cell coupled in parallel with a supercapacitor and the three-electrode hybrid cell.

In further research, improvements should be focused on aspects such as shorter proton diffusion distances, a more efficient electrical contact between the gas diffu-

Table 6.1: Comparison between a typical carbon supercapacitor electrode and the two-electrode (2-E) hybrid cell.

Feature	Units	Supercapacitor	2-E hybrid cell
Charging[a]		ΔV or i has to be applied	spontaneous
Capacitance	μF cm^{-2}	10-16	7-12
Energy stored[b]	J g^{-1}	77 (electrical)	201 (chemical)
Use of noble metals		no	yes
Reversibility[c]	%	80-100[d]	80-90
Proved cyclability	No. of cycles	2000[d]	100

[a] conditions for the charging process.

[b] values calculated assuming a specific capacitance of 12 μF cm^{-2} at 1 V.

[c] in terms of Coulombic efficiency between charging and discharging process.

[d] data obtained from reference [26].

Table 6.2: Comparison between a typical PEM fuel cell (FC) coupled in parallel with a supercapacitor (SC) and the three-electrode (3-E) hybrid cell.

Feature	Units	FC-SC	3-E hybrid cell
FC performance	mW cm^{-2}	ca. 1000	20
FC internal resistance	Ω cm^{-2}	lower than 0.1[a]	7.6
SC charging		fuel cell voltage used	spontaneous process
No. of systems		2 (FC + SC)	1 (hybrid cell)
Power response[b]		available	available

[a] data obtained from reference [64].

[b] represents the response of the system to a peak power demand.

sion layer and the catalyst layer as well as the use of a thinner current collector of the supercapacitor type-electrode with also an improved open ratio. However, the high value of the internal resistance in comparison with typical PEM fuel cells makes a possible implementation of this concept for practical purposes difficult. In spite of these difficulties, the great merit of this concept is the new insights that it brings on the new field of hybridization between fuel cells and supercapacitors in which a Faradaic PEM fuel cell-electrode is coupled with a non-Faradaic electrochemical supercapacitor-type electrode. The spontaneous nature of the charging and discharging processes as well as the very good charging-discharging reversibility, associated with a high Coulombic efficiency of this system, have to be also highlighted.

7 Zusammenfassung

Wasserstoff hat sich zu einer der am stärksten ernstzunehmenden Möglichkeiten entwickelt, fossile Brennstoffe ersetzen zu können, vor allem im Transportbereich. Dies ist hauptsächlich in seiner Umweltfreundlichkeit begründet, da das einzige Produkt aus seiner Verwendung, beispielsweise in Brennstoffzellen, reines Wasser ist. Eine große Herausforderung, die jedoch noch gemeistert werden muss, um diese Technik effizient und ausreichend sicher zu machen, um sich gegen Verbrennungsmotoren durchzusetzen, ist die Wasserstoffspeicherung. In nahezu allen verfügbaren Möglichkeiten der Wasserstoffspeicherung sind ein hoher Druck oder niedrige Temperaturen notwendig, und dies nicht nur für die Speicherung, sondern auch für die Freisetzung von Wasserstoff, was einen beträchtlichen Energieverbrauch mit sich bringt. Manche dieser Methoden haben zudem Schwierigkeiten bezüglich der Reversibilität. Aus diesem Grund haben wir ein neues Konzept für Wasserstoffspeicherung untersucht. Es funktioniert bei Standardbedingungen reversibel und ohne bedeutenden Energieverlust, und es basiert auf der Hybridisierung einer Brennstoffzelle (BZ) und eines Superkondensators (SK).

Die Grundidee besteht in der elektrochemischen Spaltung von Wasserstoff in Protonen und Elektronen an einer BZ-Elektrode sowie in der separaten Speicherung beider Spezies in einer elektrolytischen Doppelschicht einer SK-Elektrode, die aus elektrisch leitfähigen Kohlenstoffmaterialien mit großer Oberfläche hergestellt ist. Eine große Oberfläche ist notwendig, um hohe Speicherkapazitäten zu erzielen.

Unter der Annahme, dass alle Kohlenstoffatome sich an der Oberfläche befinden und jedes eine negative Ladung trägt, wäre ein H_3O^+-Ion notwending um die negative Ladung im Kohlenstoff auszugleichen und die Doppelschicht zu bilden. Es wird eine theoretische Speicherkapazität von ca. 7 wt.% H_2 berechnet, unter Berücksichtigung, dass für die Speicherung eines Wasserstoffatoms in diesem System ein Wassermolekül und ein Kohlenstoffatom notwendig sind.

Die Untersuchung dieses Konzepts wurde zuerst an einem Hybrid aus zwei Elektroden - einer Brennstoffzelle und einem Superkondensator - durchgeführt. Die BZ-Elektrode bestand aus Platin, aufgebracht auf carbon black, mit einer Katalysatorbeladung von ca. 0,45 mg cm^{-2}. Nafion®-112-Membranen wurden als Separator

eingesetzt. Auf der Seite der SK-Elektrode wurden H_2O, NaOH und H_2SO_4 als Elektrolyte verwendet. Als Elektrode wurden carbon black Black Pearls 2000 (BET = 1155 m^2 g^{-1}) mit Massenladungen zwischen 0,7 und 3,8 mg cm^{-2} eingesetzt.

Spontanes reversibles Laden und Entladen dieser Zelle wurde lediglich durch einen Wechsel des in der BZ-Elektrode zugeführten Gases (H_2 zum Laden, O_2 zum Entladen) und unter Verwendung von H_2O und verschiedenen Elektrolyten erreicht. Es wurde weder ein Strom noch eine Spannung angelegt, die Zelle arbeitete unter Standardbedingungen. Die erzielten Wasserstoffspeicherkapazitäten waren allerdings nur gering. Die höchste Speicherkapazität von 0,17 wt.% H_2 und 0,13 wt.% H_2 bei Laden und Entladen wurden erreicht bei einem Einsatz von 7 M H_2SO_4 und bei einem Wasserstoffdruck von 2,5 bar. Obwohl die Speicherkapazitäten gering sind, ist die Verbrennungsenergie des in dieser Zelle gespeicherten Wasserstoffs bei einer Speicherkapazität von 0,13 wt.% H_2 um einen Faktor von 2,6 höher als die elektrische Energie, die in einem symmetrischen Superkondensator von vergleichbar hoher Qualität gespeichert ist.

Die Triebkraft der Lade- und Entladeprozesse ist die Potenzialdifferenz zwischen den beiden Elektroden, die ihren Ursprung in den verschiedenen Redoxpotenzialen der involvierten elektrochemischen Reaktionen hat. Die ablaufenden Reaktionen während des Ladens sind die elektrochemische Oxidation von H_2 in der BZ-Elektrode vs. die Reduktion der sauerstoffbasierten Oberflächengruppen (z.B. chinonartige Gruppen) in der SK-Elektrode. Während des Entladens sind dies die elektrochemische Reduktion von O_2 vs. die Oxidation der sauerstoffbasierten Oberflächengruppen.

Das Sinken des Wasserstoffdrucks um mehrere mbar während des Ladeprozesses bestätigte, dass gleichzeitig mit dem Beladen der Doppelschicht an der BZ-Elektrode H_2 oxidiert und an der SK-Elektrode sauerstoffbasierte elektroaktive Oberflächengruppen (Pseudokapazität) reduziert wurden. Während des Entladeprozesses wurden die Protonen durch die Membran zur BZ-Elektrode zurücktransportiert, wo sie mit Sauerstoff und Elektronen zu Wasser reagierten. Gleichzeitig wurden die elektroaktiven Gruppen an der carbon black-Oberfläche oxidiert.

Die bi-exponentielle Analyse der asymmetrischen Lade-Entladekurven lässt darauf schließen, dass wenigstens zwei Subprozesse während des Be- und Entladens der Zelle abliefen. Der erste entspricht einem schnellen Prozess. Dieser steht in Verbindung mit dem Laden und Entladen der Doppelschicht an der äußeren Oberfläche der carbon black-Schicht und mit dem Laden und Entladen der Pseudokapazität, die durch die sauerstoffbasierten Redox-Oberflächenfunktionalitäten produziert wird. Unter der Verwendung von 7 M H_2SO_4 als Elektrolyt weist er typische Zeitkonstanten von 8 s

auf. Der zweite wird als langsamer Subprozess betrachtet. Er steht in Beziehung mit dem Laden und Entladen der Doppelschicht an der inneren Oberfläche der carbon black-Schicht (poröses System) und hat unter Verwendung von 7 M H_2SO_4 als Elektrolyt typische Zeitkonstanten von 50-80 s.

Die Ergebnisse der Lade-Entladeexperimente mit verschiedenen Wasserstoffdrücken und unter der Verwendung von H_2O weisen darauf hin, dass die Wasserstoffspeicherkapazität der Zelle bei einem Wasserstoffdruck von 1,5 bar nahezu erschöpft war. Bei diesem Druck wurden 0,063 wt.% H_2 Wasserstoff gespeichert. Dies entspricht ca. 0,01 e^- pro Kohlenstoffatom und ist weit entfernt von dem anfänglich angenommenen Wert von 1 e^- pro Kohlenstoffatom. Eine Verstärkung des Drucks um 2 bar führte zu lediglich 22% Steigerung der Speicherkapazität. Die hauptsächlichen Limitierungen der Speicherkapazität dieses Systems liegen in der elektrostatischen Abstoßung zwischen den Oberflächenladungen, der begrenzten Menge an Oberflächenatomen, die eine volle Ladung tragen können und deren Zugänglichkeit für die Ionen in der Elektrolytlösung. Zudem waren nicht alle Kohlenstoffatome durch den Elektrolyt befeuchtet oder elektrisch mit dem Stromabnehmer verbunden.

Die Kapazitäten der Hybridzelle unter der Verwendung verschiedener Elektrolyte wurden mittels galvanostatischer und cyclovoltammetrischer Experimente untersucht. Die Ergebnisse waren folgende: 7 μF cm^{-2} für H_2O und 12 μF cm^{-2} für 7 M NaOH und H_2SO_4. Die verschiedenen Kapazitäten bei der Benutzung unterschiedlicher Elektrolyte haben ihren Grund in der Veränderung der Struktur der Doppelschicht und dem Einfluss des pH-Werts auf die Redoxpotenziale der mit der Pseudokapazität zusammenhängenden Reaktionen. Diese spezifischen Kapazitäten sind vergleichbar mit den in der Literatur genannten typischen Werte für Doppelschichtkapazitäten von carbon blacks in wässrigen Elektrolyten.

Der durch das spontane Laden und Entladen der Zelle produzierte Elektronenfluss durch den äußeren Stromkreis erzeugte eine Leistungsspitze von ca. 20 mW cm^{-2} im äußeren Lastwiderstand. Dies zeigte das Potenzial der Zelle als zusätzliche Ressource (die im Falle eines Spitzenleistungsbedarfs eingesetzt werden kann) einer primären Energiequelle, wie z.B. einer Polymerelektrolyt-Brennstoffzelle. Um diesen Gedanken zu verfolgen, wurde eine erweiterte Version der ursprünglichen Zelle untersucht. Dieser neue Aufbau basiert auf der Kombination von zwei BZ-Elektroden (Anode und Kathode einer Polymerelektrolyt-Brennstoffzelle) mit einer SK-Elektrode in einer Ein-Zellen-Konfiguration. Wurde diese Drei-Elektroden-Hybridzelle in der Funktion einer Polymerelektrolyt-BZ eingesetzt, war die Leistung ca. 22 mW cm^{-2}. Im Vergleich mit der Leistung typischer Polymerelektrolyt-BZ von 1 W cm^{-2} ist

dieser Wert sehr gering. Der Grund dafür ist eine 40 Mal größere Protonendiffusionsdistanz in dieser Zelle sowie das niedrige Verhältnis aus offenen Löchern zur Gesamtfläche (sog. *open ratio*) der Graphitelektrode.

Wurde diese Zelle als Superkondensator betrieben, zeigte das Lade-Entladeverhalten eine gute Reproduzierbarkeit und Reversibilität über 100 Zyklen. Die Lade-Entladekurven zeigten ebenfalls ein bi-exponentielles Verhalten. Aufgrund des geringeren äußeren Widerstands waren allerdings die Zeitkonstanten kleiner als jene, die in den Experimenten mit der Zwei-Elektroden-Zelle beobachtet wurden (zwischen 0,5 und 1 s für den schnellen Subprozess und 3-7 s für den langsamen). In diesem Fall stand der schnelle Subprozess mit dem Laden-Entladen der Pseudokapazität in Verbindung.

Die Fähigkeit der SK-Elektrode, die durch die Brennstoffzelle in einem äußeren Lastwiderstand entwickelte Leistungsdichte zu erhöhen, ist abhängig vom Strom, mit dem die Brennstoffzelle betrieben wird (i_{FC}). Die gesamte Leistungsdichte (Leistung von Brennstoffzelle und Superkondensator) wurde durch Laden und Entladen bei einem i_{FC} von 3,1 mA cm^{-2} für einige Sekunden auf bis zu 40 mW cm^{-2} erhöht. Lag der i_{FC} bei ca. 60 mA cm^{-2}, trat dagegen nur eine Steigerung von 4 mW cm^{-2} auf. Die Ursache hierfür sind Depolarisierungseffekte an den BZ-Elektroden bei hohen i_{FC}-Werten. Diese in dem äußeren Lastwiderstand erzeugte Leistungssteigerung wurde praktisch unabhängig vom Betrieb der Brennstoffzelle erreicht. Dadurch kann die Energie der BZ-Elektroden über die höhere Rate der Energiefreisetzung der SK-Elektrode entnommen werden.

Diese Ergebnisse zeigen, dass dieses neuartige Konzept der Wasserstoffspeicherung durch die Hybridisierung einer Brennstoffzelle mit einem Superkondensator, wie es in dieser Arbeit unter der Verwendung zweier Zellaufbauten untersucht wurde, realisierbar ist. Ein exakter Vergleich dieses Systems mit den typischen Hybriden aus Brennstoffzellen oder Batterien mit Superkondensatoren ist schwierig, da große Unterschiede im Aufbau existieren sowie unterschiedliche Charakterisierungsmethoden zum Einsatz kommen. Die Tabellen 7.1 und 7.2 zeigen einen allgemeinen Vergleich zwischen einer typischen SK-Elektrode und der Zwei-Elektroden-Hybridzelle sowie zwischen einer Polymerelektrolyt-Brennstoffzelle parallel verbunden mit einem Superkondensator und der Drei-Elektroden-Hybridzelle.

In zukünftiger Forschung sollten sich Verbesserungen auf Aspekte wie kürzere Wege in der Protonendiffusion konzentrieren, desweiteren auf einen effizienteren elektrischen Kontakt zwischen der Gasdiffussions- und der Katalysatorschicht sowie auf einen dünneren Stromabnehmer an der SK-Elektrode und damit einhergehend einen besseren *open ratio*. Die hohen Werte des inneren Widerstands im Vergleich

Table 7.1: Vergleich zwischen einer typischen Kohlenstoff-Superkondensator-Elektrode und der Zwei-Elektroden (2-E)-Zelle.

Eigenschaften	Einheiten	Superkondensator	2-E-Zelle
Ladung[a]		ΔV oder i muss angelegt werden	spontan
Kapazität	μF cm^{-2}	10-16	7-12
Gespeicherte Energie[b]	J g^{-1}	77 (elektrisch)	201 (chemisch)
Verwendung von Edelmetallen		nein	ja
Reversibilität[c]	%	80-100[d]	80-90
erwiesene Laufzeit	N° Zyklen	2000[d]	100

[a] Bedingungen für den Ladeprozess.

[b] Berechnete Werte unter der Annahme einer bestimmten Kapazität von 12 μF cm^{-2} bei 1 V.

[c] Ausdruck Coulombscher Effizienz zwischen Lade- und Entladeprozess.

[d] Daten aus Quelle [26].

Table 7.2: Vergleich zwischen einer typischen Polymerelektrolyt-Brennstoffzelle (BZ) parallel verbunden mit einem Superkondensator und der Drei-Elektroden-Zelle (3-E).

Eigenschaften	Einheiten	BZ-SK	3-E Zelle
BZ Leistung	mW cm^{-2}	ca. 1000	20
BZ innerer Widerstand	Ω cm^{-2}	niedriger als 0.1[a]	7.6
SK Ladung		Spannung der Brennstoffzelle benutzt	spontaner Prozess
Anzahl Systeme		2 (BZ + SK)	1 (hybridzelle)
Reaktionsfähigkeit[b]		vorhanden	vorhanden

[a] Daten aus Quelle [64].

[b] Repräsentiert die Reaktion des Systems auf die Notwendigkeit einer Leistungsspitze.

mit typischen Polymerelektrolyt-Brennstoffzellen machen eine mögliche Implementierung dieses Konzepts in der Praxis jedoch problematisch. Trotz der Schwierigkeiten liegt der große Gewinn dieses Konzepts in den neuen Erkenntnissen auf dem noch

neuen Gebiet der Hybridisierung von Brennstoffzellen und Superkondensatoren, in dem eine Faradaysche Polymerelektrolyt-BZ-Elektrode mit einer nicht-Faradayschen elektrochemischen SK-Elektrode verbunden wird. Die spontane Art der Lade- und Entladeprozesse sowie die hervorragende Lade-Entladereversibilität, zurückzuführen auf eine hohe Coulombsche Effizienz in diesem System, sind ebenso hervorhzuheben.

Acknowledgments

In the first place I want to thank God for give me the strength to achieve my goals.

In particular I would like to thank Prof. Dr. Emil Roduner for his advice and support throughout this work and for always be available.

Many thanks to the DAAD for the scholarship and for giving me the possibility to study in Germany. Thank you to Ursula Habel for always be friendly and for her support.

I am very grateful to Prof. Dr. Klaus Müller for kindly writing the evaluations of my DAAD reports and for accepting to take part in the final evaluation of this work.

Thanks to Prof. Dr.-Ing. Elias Klemm also for taking part in the final evaluation of this work.

My thanks to Christopher Jensen for the great time we shared and for show me the meaning of a real German Freundschaft.

I also want to thank my team for always been friendly and helpful, specially, Tobias Kittel for his help in almost everything, Augusta Ene and Barbara Vogel for the support at the beginning of my studies in Stuttgart, Alexander Kromer and Steffen Hink for the scientific discussions.

My thanks go also to the people of the mechanical workshop and our "CTAs", specially to Walter Ottmüller, Thomas Weigend, Jürgen Hußke, Jochen Graff, Beatrice Omiecienski and Gabrielle Bräuning.

Finally I would like to thank my Dagmar, because without her support and love this work would not have been possible.

Not to forget my parents who gave me encouragement and support to come to Germany and for teaching me that you must go through with the things you start and to fight for achieving your goals.

Jesus Enrique Zerpa Unda

Bibliography

[1] S. Saito. *Journal of Nuclear Materials*, 398(1-3):1–9, 2010.

[2] M. Z. Jacobson. *Energy and Environmental Science*, 2(2):148–173, 2009.

[3] U. Eberle, M. Felderhoff, and F. Schüth. *Angewandte Chemie - International Edition*, 48(36):6608–6630, 2009.

[4] I. R. Harris, D. Book, P. A. Anderson, and P. P. Edwards. *The Fuel Cell Review*, (June/July):17–23, 2004.

[5] C. Vix-Guterl, E. Frackowiak, K. Jurewicz, M. Friebe, J. Parmentier, and F. Beguin. *Carbon*, 43(6):1293–1302, 2005.

[6] L. Schlapbach and A. Züttel. *Nature*, 414(6861):353–358, 2001.

[7] A. Züttel. *Naturwissenschaften*, 91(4):157–172, 2004.

[8] F. Barbir. *PEM Fuel Cells: Theory and Practice*. Elsevier Academic Press, London, 2005.

[9] T. A. Zawodzinski, T. E. Springer, J. Davey, R. Jestel, C. Lopez, J. Valerio, and S. Gottesfeld. *Journal of the Electrochemical Society*, 140(7):1981–1985, 1993.

[10] N. Wagner, T. Kaz, and K. A. Friedrich. *Electrochimica Acta*, 53(25):7475–7482, 2008.

[11] Z. G. Qi and A. Kaufman. *Journal of Power Sources*, 113(1):37–43, 2003.

[12] G. Sasikumar, J. W. Ihm, and H. Ryu. *Journal of Power Sources*, 132(1-2):11–17, 2004.

[13] B. E. Conway. *Electrochemical Supercapacitors Scientific Fundamentals and Technological Applications*. Kluver Academic / Plenum Publishers, New York, 1999.

[14] D. C. Grahame. *Chemical Reviews*, 41(3):441–501, 1947.

[15] K. Kinoshita. *Carbon: Electrochemical and physicochemical properties*. John Wiley and Sons, New York, 1988.

[16] A. G. Pandolfo and A. F. Hollenkamp. *Journal of Power Sources*, 157(1):11–27, 2006.

[17] K. Kinoshita and J. A. S. Bett. *Carbon*, 13(5):405–409, 1975.

[18] K. Kinoshita and J. A. S. Bett. *Carbon*, 13(6):551–551, 1975.

[19] D. Y. Qu and H. Shi. *Journal of Power Sources*, 74(1):99–107, 1998.

[20] M. Endo, Y. J. Kim, T. Takeda, T. Maeda, T. Hayashi, K. Koshiba, H. Hara, and M. S. Dresselhaus. *Journal of the Electrochemical Society*, 148(10):A1135–A1140, 2001.

[21] K. S. W. Sing, D. H. Everett, R. A. W. Haul, L. Moscou, R. A. Pierotti, J. Rouquerol, and T. Siemieniewska. *Pure and Applied Chemistry*, 57(4):603–619, 1985.

[22] H. Shi. *Electrochimica Acta*, 41(10):1633–1639, 1996.

[23] G. Salitra, A. Soffer, L. Eliad, Y. Cohen, and D. Aurbach. *Journal of the Electrochemical Society*, 147(7):2486–2493, 2000.

[24] C. Lin, J. A. Ritter, and B. N. Popov. *Journal of the Electrochemical Society*, 146(10):3639–3643, 1999.

[25] R. de Levie. *Electrochimica Acta*, 8(10):751–780, 1963.

[26] F. Beck, M. Dolata, E. Grivei, and N. Probst. *Journal of Applied Electrochemistry*, 31(8):845–853, 2001.

[27] R. Richner, S. Müller, and A. Wokaun. *Carbon*, 40(3):307–314, 2002.

[28] E. Frackowiak and F. Beguin. *Carbon*, 39(6):937–950, 2001.

[29] M. D. Stoller and R. S. Ruoff. *Energy and Environmental Science*, 3(9):1294–1301, 2010.

[30] P. J. Hall, M. Mirzaeian, S. I. Fletcher, F. B. Sillars, A. J. R. Rennie, G. O. Shitta-Bey, G. Wilson, A. Cruden, and R. Carter. *Energy and Environmental Science*, 3(9):1238–1251, 2010.

[31] R. Kötz and M. Carlen. *Electrochimica Acta*, 45(15-16):2483–2498, 2000.

[32] B. E. Conway and W. G. Pell. *Journal of Solid State Electrochemistry*, 7(9):637–644, 2003.

[33] W. G. Pell and B. E. Conway. *Journal of Power Sources*, 136(2):334–345, 2004.

[34] A. I. Belyakov. Asymmetric electrochemical supercapacitors with aqueous electrolytes. In *3rd. European Symposium on Supercapacitors and Applications*, Roma, Italy, 2008.

[35] L. L. Zhang and X. S. Zhao. *Chemical Society Reviews*, 38(9):2520–2531, 2009.

[36] B. Panella, M. Hirscher, and S. Roth. *Carbon*, 43(10):2209–2214, 2005.

[37] V. Gogel, T. Frey, Y. S. Zhu, K. A. Friedrich, L. Jorissen, and J. Garche. *Journal of Power Sources*, 127(1-2):172–180, 2004.

[38] J. G. Liu, T. S. Zhao, Z. X. Liang, and R. Chen. *Journal of Power Sources*, 153(1):61–67, 2006.

[39] H. Yang, T. S. Zhao, and Q. Ye. *Journal of Power Sources*, 142(1-2):117–124, 2005.

[40] V. V. Panic, R. M. Stevanovic, V. M. Jovanovic, and A. B. Dekanski. *Journal of Power Sources*, 181(1):186–192, 2008.

[41] F. Rouquerol, J. Rouquerol, and K. Sing. *Adsorption by Powders and Porous Solids: Principles, Methodology and Applications*. Academic Press, San Diego, 1999.

[42] Y. Wang and J. P. Zheng. *Rare Metals*, 25(6, Supplement 1):12–18, 2006.

[43] M. Toupin, D. Belanger, I. R. Hill, and D. Quinn. *Journal of Power Sources*, 140(1):203–210, 2005.

[44] M. Boero, T. Ikeshoji, and K. Terakura. *Chemphyschem*, 6(9):1775–1779, 2005.

[45] P. M. Biesheuvel and M. Z. Bazant. *Physical Review E*, 81(3), 2010.

[46] L. B. Hu, J. W. Choi, Y. Yang, S. Jeong, F. La Mantia, L. F. Cui, and Y. Cui. *Proceedings of the National Academy of Sciences of the United States of America*, 106(51):21490–21494, 2009.

[47] V. Khomenko, E. Raymundo-Pinero, and F. Beguin. *Journal of Power Sources*, 195(13):4234–4241, 2010.

[48] P. Delahay and C. W. Tobias. *Advances in Electrochemistry and Electrochemical Engineering*, volume 7. Interscience, New York, 1970.

[49] K. J. Chae, M. Choi, F. F. Ajayi, W. Park, I. S. Chang, and I. S. Kim. *Energy and Fuels*, 22(1):169–176, 2008.

[50] A. J. Bard and L. R. Faulkner. *Electrochemical methods. Fundamentals and applications*. John Wiley and Sons, New York, second edition, 2001.

[51] K. Jurewicz, E. Frackowiak, and F. Beguin. *Applied Physics a-Materials Science and Processing*, 78(7):981–987, 2004.

[52] K. Jurewicz, E. Frackowiak, and F. Beguin. *Electrochemical and Solid State Letters*, 4(3):A27–A29, 2001.

[53] K. W. Park, H. J. Ahn, and Y. E. Sung. *Journal of Power Sources*, 109(2):500–506, 2002.

[54] V. Khomenko, E. Frackowiak, and F. Beguin. *Electrochimica Acta*, 50(12):2499–2506, 2005.

[55] V. Khomenko, E. Raymundo-Pinero, and F. Beguin. *Journal of Power Sources*, 153(1):183–190, 2006.

[56] V. Khomenko, E. Raymundo-Pinero, E. Frackowiak, and F. Beguin. *Applied Physics A - Materials Science and Processing*, 82(4):567–573, 2006.

[57] H. E. Darling. *Journal of Chemical and Engineering Data*, 9(3):421–426, 1964.

[58] A. B. Duso and D. D. Y. Chen. *Analytical Chemistry*, 74(13):2938–2942, 2002.

[59] N. Agmon. *Chemical Physics Letters*, 244(5-6):456–462, 1995.

[60] G. E. Walrafen, W. H. Yang, Y. C. Chu, and M. S. Hokmabadi. *Journal of Solution Chemistry*, 29(10):905–936, 2000.

[61] A. Telfah, G. Majer, K. D. Kreuer, M. Schuster, and J. Maier. *Solid State Ionics*, 181(11-12):461–465, 2010.

[62] P. Thounthong, V. Chunkag, P. Sethakul, B. Davat, and M. Hinaje. *IEEE Transactions on Vehicular Technology*, 58(8):3892–3904, 2009.

[63] A. Payman, S. Pierfederici, and F. Meibody-Tabar. *Energy Conversion and Management*, 49(6):1637–1644, 2008.

[64] F. N. Büchi and G. G. Scherer. *Journal of the Electrochemical Society*, 148(3):A183–A188, 2001.